On Advances in LAS Instrumentation and Fiducial Volume Simulations of the S140 Detector for the NEWS-G Dark Matter Search Experiment

by

Carter David Garrah

A thesis submitted in partial fulfillment of the requirements for the degree of

Master of Science

Department of Physics

University of Alberta

Abstract

NEWS-G is a direct detection dark matter experiment specializing in gas-ionization detectors called Spherical Proportional Counters (SPCs) to search for low-mass particle dark matter. Principal measurement campaigns undergone by NEWS-G, previously at the *Laboratoire Souterrain de Modane* (LSM) and currently at SNOLAB, have used a large-scale 140 cm diameter SPC called S140.

This thesis will explore two studies related to the understanding of S140's volume and gas characteristics. First, the characterization of the detector's fiducial volume (referred to as 'fiducialization'), defined as the volume where the detector is sensitive to signal formation, will be explored using Monte Carlo electron drift simulations. This simulation framework will be used in this thesis for the determination of limits on the effective mass acceptance of S140 during the LSM measurement campaign through the calculation of the detector's fiducialization efficiency. A second study will also be presented looking at the feasibility of novel measurement techniques with prototype Laser Absorption Spectroscopy (LAS) apparatuses in the live measurement of the concentration of CH_4 within S140.

Preface

The work presented in this thesis was completed by myself, Carter Garrah, in contribution towards the NEWS-G experiment collaboration under the supervision of Dr. Marie-Cécile Piro at the University of Alberta. The NEWS-G collaboration is, at the time of writing, lead by Dr. Guillaume Giroux of Queen's University and Dr. Konstantinos Nikolopoulos of the University of Birmingham with Dr. M.-C. Piro serving as the Principal Investigator for NEWS-G at the University of Alberta.

The content of Chapters 4 and 5 on the fiducialization simulations of NEWS-G's S140 detector were completed using modified simulation code originally written and provided by Yuqi Deng. Adaptation of said simulation framework for the studies presented in the aforementioned chapters was performed by myself. Analysis techniques and methodology were contributed to by Daniel Durnford, Georgios Savvidis, and Francisco Vazquez de Sola, amongst others in the collaboration during related discussions. Chapter 6 presents work originally conceived through discussions involving Dr. William Morrish, Dr. Al Meldrum, and Patrick O'Brien, all of whom contributed to this work. Design of the presented prototype gas cell was made with assistance from Mitchel Baker and Youngtak Ko. LAS methodology and apparatus design was also assisted by Dr. W. Morrish. Measurement equipment regarding laser safety and for integrating sphere test measurements were provided by Dr. A. Meldrum.

Acknowledgements

If I were to say that my Master's degree experience had been as I expected, anyone who recalls the years of 2020 through 2022 would know that this would be a lie. These past two years were full of promised excitement with the unknown of exploring a new province, gaining further independence, having a whole new lab to settle into, and oh yeah: just a little global pandemic!

This experience has been, to say the least, a very wild ride. While much of my time at the University of Alberta thus far has been remote, even as far as from my hometown of Kingston, this has left me a lot of time to reflect on my education and future in astroparticle physics. While I still have much to learn in my field of study, I pride myself in my earnest desire to contribute, be of use to others, and collaboratively work towards our understanding of the Universe around us, like the countless of researchers before me. As I complete the writing of this thesis, marking not just the end of one chapter in my career, but the beginning of my continued, rewarding stay at the UofA, there are a handful of people who I would like to extend my personal thanks to.

First and foremost I want to thank my supervisor, Marie Cécile Piro - the one who convinced me to trek across the country to Edmonton. You were instrumental in all of my successes during these past two years, knowing how to push me just the right amount to go beyond my doubts - I am very much looking forward to continuing this journey under your guidance. To my lab mates Daniel Durnford, Yuqi Deng, and Patrick O'Brien, as well as my collaborator William Morrish, the work presented in this thesis would not have been possible if it weren't for your advice, feedback,

and consistent efforts in aiding me and answering all of my many questions. To my collaborators and old colleagues at Queen's University and the rest of the NEWS-G collaboration, namely Philippe Gros who got me started with my involvement in this wonderful group, thank you all for your support, many discussions, and I am very much looking forward to continue working with all of you for the near future. And to everyone else in the Piro Group at the UofA, I am looking forward to getting to know you all better as we transition back to proper in-person operations in the lab and University - I very much hope that we get to work together further! I would also like to take a moment to offer my thanks to NSERC and the McDonald Institute, whose research funding during my Master's degree has helped make this work possible.

Lastly, I would like to thank my friends and family who helped me get moments of rest during the chaos of the pandemic. To my grandparents, whose weekly phone call were always a delight, especially their questions on my research of "black holes". Most of all, to my sister and parents who assisted me during this adventure - their efforts in supporting me have not gone unnoticed and I couldn't have done this without them. And of course, I would like to give a very well deserved thanks to Louie, George, Monty, and Murphy (my pets) who were just the sparks of joy that I needed during these past two years.

Table of Contents

List of Tables

List of Figures

Abbreviations

ADU Analog to Digital Units.

ALS Asymmetric Least Squares Smoothing.

AU Arbitrary Units.

BGA Binary Gas Analyzer.

CAD Computer-Aided Design.

CDM Cold Dark Matter.

CEvNS Coherent Elastic Neutrino-Nucleus Scattering.

CMB Cosmic Microwave Background.

DAQ Data Acquisition.

DFB Distributed-Feedback.

DM Dark Matter.

LAS Laser Absorption Spectroscopy.

LDC Laser Diode Controller.

LSM Laboratoire Souterrain de Modane.

MACHO Massive Compact Halo Object.

MC Monte Carlo.

MOND Modified Newtonian Dynamics.

NaN Not a Number.

NEWS-G New Experiments With Spheres-Gas.

P&ID Piping and Instrumentation Diagram.

PD Photodetector.

QCD Quantum Chromodynamics.

SD Spin-Dependent.

SI Spin-Independent.

SM Standard Model.

SPC Spherical Proportional Counter.

SUSY Super Symmetry.

TDLAS Tunable Diode Laser Absorption Spectroscopy.

TEC Thermoelectric Cooler.

WIMP Weakly Interacting Massive Particle.

Chapter 1

Introduction

It has been over a century since observational evidence of what would come to be known as "Dark Matter" first puzzled physicists and astronomers. What has spawned over the decades since is a rich sub-field of study in astroparticle physics with entire collaborations dedicated to finding a solution to the observable Universe's "missing mass" problem. Today, it is the consensus within the physics community that 84.4% of the Universe's mass content is composed of some form of invisible, non-luminous matter [1]. Since the 1980's, dark matter has been theorized to be particle-like and existing beyond the Standard Model of particle physics, comprising of WIMPs: Weakly Interacting Massive Particles [2, 3]. In the search for WIMPs and other WIMP-like particles (amongst other possible candidates), a specific area of recent interest is the low-energy regime, with WIMP masses on the order of 1 GeV/c^2 or less. Experiments specializing in this particular area include the subject of this thesis: the NEWS-G experiment [4].

NEWS-G (New Experiments With Spheres-Gas) is a collaborative direct detection dark matter search experiment formed in 2008 which makes use of Spherical Proportional Counters (SPCs), a type of gaseous particle detector, in searching for evidence of low-mass WIMPs. Since 2015, the NEWS-G collaboration have been world-leaders in low-mass WIMP sensitivity with the SEDINE detector [4]. The current generation of NEWS-G detector, set to improve upon the SEDINE results, is known as S140.

S140 is a large-scale 140 cm diameter SPC first commissioned at the Laboratoire Souterrain de Modane (LSM) in Modane, France in 2019 [5]. The data recorded during this commissioning campaign totalled roughly ten days, making use of a pure methane (CH_4) target gas. At present, S140 is under commission at SNOLAB [6] - a $\sim$2 km deep underground clean room laboratory located in Sudbury, Canada. The work of this thesis is centred around a combination of simulation-based analysis work and instrumentation in support of the collaboration's endeavours with S140 concerning the properties of the active gas volume and contents of the detector.

In Chapter 2 we will take a look at the historical context of dark matter including key pieces of observational evidence. There I will present the current status of modern WIMP direct detection search experiments along with their properties and fundamental detection principles. Chapter 3 will be a brief overview of the NEWS-G collaboration, focusing on SPC operating principles and both the current and future outlook of the experiment's WIMP measurement campaigns. For Chapters 4 and 5 I will present my contributing work to S140's LSM CH_4 data analysis campaign currently being undertaken by the collaboration. In Chapter 4 specifically, I will present the current methodology for a custom first-principles 3-D Monte Carlo electron drift simulation of S140. For Chapter 5 I will detail the specific application and calibration of such a simulation framework in studying the fiducialization - the characterization of the detector volume that is sensitive to signal formation - of the S140 detector for the purpose of setting cuts on the total mass exposure of CH_4 S140 during the LSM campaign. Lastly, Chapter 6 will take a look towards the future with a new instrumentation project using Laser Absorption Spectroscopy (LAS) techniques for studying the composition of S140's fill gas. Specifically, the testing of a prototype CH_4 concentration monitoring system will be explored alongside the practical implementation and limitations of said system for use alongside S140 underground at SNOLAB.

Chapter 2

Dark Matter

The term "Dark Matter" was originally coined just under one century ago by Swiss astrophysicist F. Zwicky, which he dubbed "Dunkle Materie" in 1933 [7]. Zwicky ascribed this term to the phenomenon of a "missing mass" component of non-luminous matter in the measured mass density of the Coma cluster of galaxies. The study of non-luminous matter began during the late 19^{th} century with early evidence arising from the observation of the Milky Way galaxy - the known Universe of the time - by W. Thomson in the 1880's [8]. The commonality of such measurements alongside those made by the likes of Dutch astronomer J. H. Oort decades later in 1932 [9], amongst others predating Zwicky [10, 11], was that the measured local stellar mass density of visible, luminous matter was inconsistent with the dispersion of galactic rotational velocities. Astronomers of the time attributed these inconsistencies to the presence of "dark" stellar bodies, laying the groundwork for a nearly century-long search for an answer to this missing mass problem. The following chapter will outline the key pieces of evidence gathered since for the presence of dark matter throughout the Universe, its properties, and detection methods specifically used in the study of particle and particle-like dark matter.

2.1 Evidence for the Existence of Dark Matter

Zwicky estimated that the mass density of the Coma cluster was too low by a factor of nearly 400 [12]. This estimate was made using the Virial Theorem to measure the total mass density of the cluster for comparison with the visible, luminous matter. While improvements to his initial measurement were made by Zwicky in the following years [13], what remained was this inconsistency in the measured mass-to-light ratio. However, in his 1937 publication, Zwicky proposed another method for ascertaining the mass distributions of galaxies: the measurement of their rotational curves.

Measurements of the rotational curves of galaxies were performed in the following decades, with more precise and significant measurements notably coming in the 1970's by astronomers such as K. Ford, V. Rubin, and K. Freeman [14–16]. Thanks to their observations, evidence began to be pooled suggesting that there is a deficiency in the gravitational forces exhibited within these galactic structures. As demonstrated by example measurements in Figure 2.1, a lack of luminous matter at increasing galactic radii does not match the relatively "flat" rotational velocity distributions of all measured galaxies [17]. While this could be attributed to an incomplete understanding of gravity itself, requiring new theoretical models (e.g. MOND - MOdified Newtonian Dynamics [18]), such observations could also be explained by the presence of non-luminous matter. The distribution of said "dark" matter throughout these galaxies, including the Milky Way, could take the form of a theorized halo (referred to as the 'dark matter halo') or other cosmological structures [17].

One of the most cited pieces of evidence for dark matter comes from imaging of the "Bullet Cluster" (galaxy cluster 1E 0657-56), as presented in Figure 2.2 [20]. The Bullet Cluster is the result of the collision between two smaller clusters of galaxies that have since begun drifting apart from one another. In studying the matter composition of this cluster, X-ray imaging (the pink coloured overlay in Figure 2.2) shows the clear distribution of thermal gas - baryonic matter - that has been slowed down via

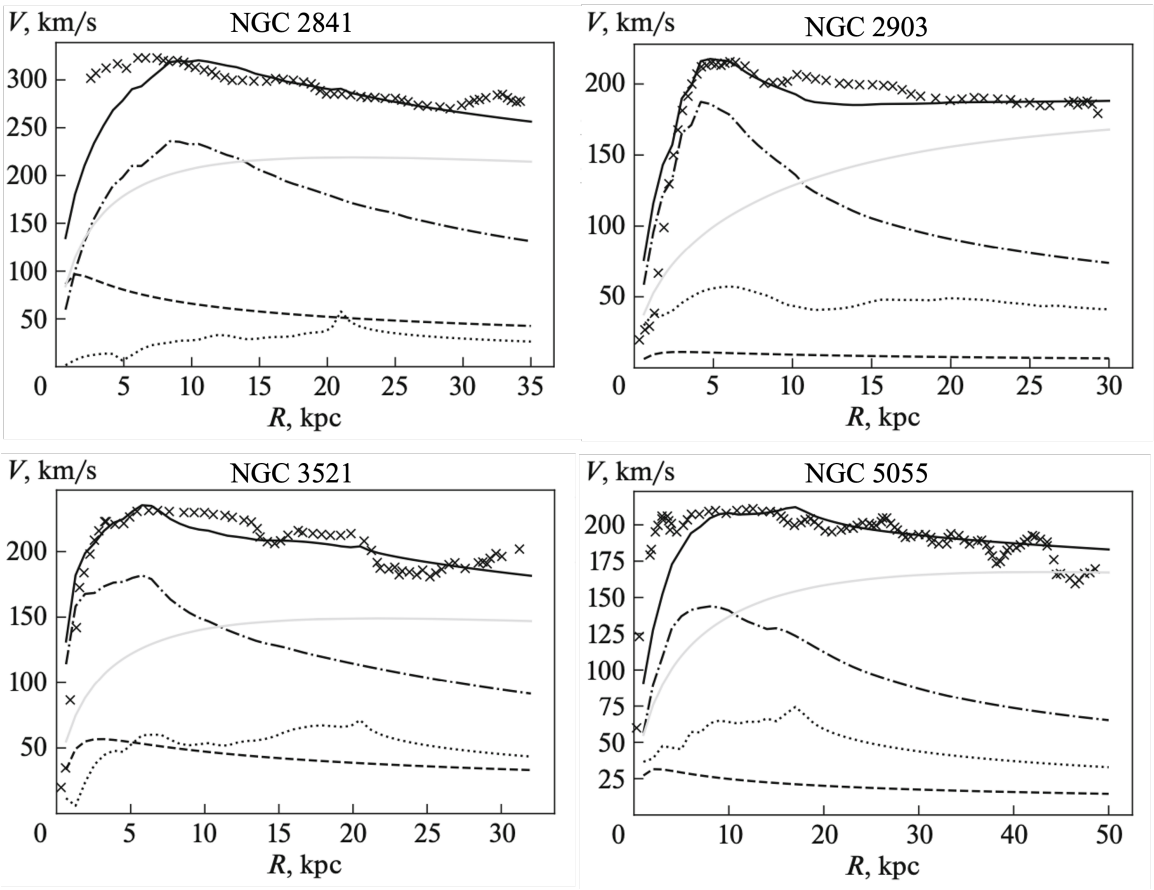

Figure 2.1: The decomposition of rotation curves for select galaxies based off of the Newtonian maximum disk model (black solid line) illustrating inconsistencies in observed radial velocities and mass density content [19]. Measured points (cross-marks) are plotted alongside component curves ascribed to visible matter in the inner-galaxy's 'bulge' (dashed) and 'disk' (dash-dotted) regions, gas (dotted), and a theoretical dark matter halo (gray solid line). Credit: D. I. Zobnina and A. V. Zasov, Astronomy Reports, vol. 64, pg. 303-306, 2020, reproduced with permission from Spinger Nature.

the collision process. However, through the study of gravitational lensing effects on this cluster, it is also observed that there is a non-luminous component that must contribute to the total observed gravitational structure. Gravitational lensing is a cosmological phenomenon predicted in A. Einstein's theory of General Relativity which results in the observable "bending" of light by a gravitational structure between the light source and observer. In the case of the Bullet Cluster, such bending can be used to surmise the presence of non-luminous 'dark matter', overlaid in blue in Figure 2.2, assuming that the majority of baryonic matter found in each sub-cluster

is interstellar gas and dust. Notably, the motion of this dark matter content involved in the collision between both sub-clusters was largely unaffected, drifting unabated to the extremities of the cluster. This evidence not only implies that this dark matter component has mass due to its gravitational structure, but must have interacted very weakly with the baryonic matter found within the sub-clusters.

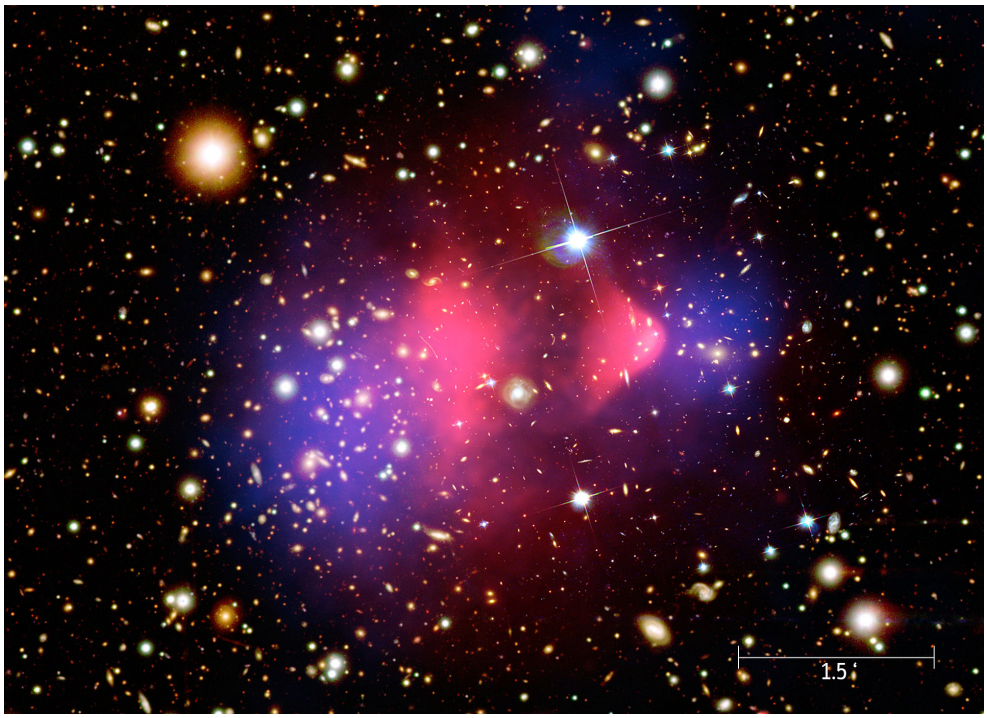

Figure 2.2: A composite image of the Bullet Cluster, as captured by the Chandra X-ray Observatory, with a colour overlay illustrating the distribution of X-rays from thermal gas (in pink) and dark matter calculated from gravitational lensing (in blue) [21]. The presence of dark matter at the extremities of the cluster indicates that it was largely unaffected by the collision (interacted weakly) between the two galactic sub-clusters, unlike the luminous gas content. Credit: NASA/CXC/SAO

Another concrete piece of evidence for dark matter comes from observations of the early Universe via the Cosmic Microwave Background (CMB). The CMB consists of the earliest observable background photons originating from the primordial observable universe, roughly 400,000 years after the Big Bang. These photons were emitted or scattered during recombination - when the early Universe first became transparent to photons - representing the distribution of matter at that time. The CMB has most

recently been measured by the Planck experiment, a space observatory launched in 2009, whose sky-map projection is shown in Figure 2.3 [22]. The 2018 Planck result showcases the sub-microKelvin fluctuations (anisotropies) in red-shifted microwaves measured in the CMB that exhibit an average measured temperature of 2.7255 $\pm$ 0.0006 K [23].

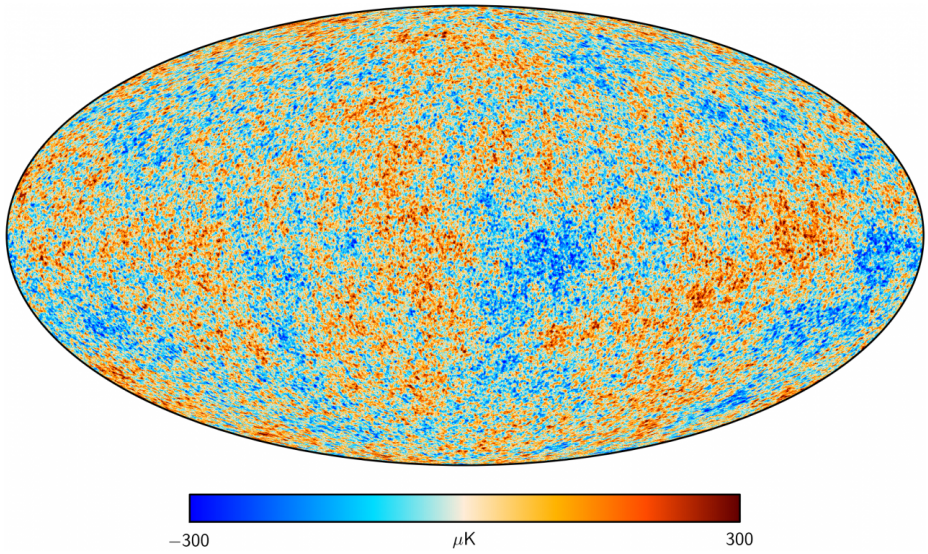

Figure 2.3: A foreground-subtracted view of the CMB sky-map as presented by the Planck experiment in 2018 [22]. Anisotropies in temperature are highlighted on the order of hundreds of μK relative to an average of 2.7255 $\pm$ 0.0006 K [23]. Credit: Y. Akrami *et al.*, A&A, vol. 641, pg. 66, 2020, reproduced with permission ©ESO.

Evidence for dark matter from the CMB comes from the interpretation of the CMB's angular power spectrum (see Figure 2.4) using the lambda cold dark matter (ΛCDM) model [1, 3]. This model is a parametrization of the structure of the Universe using evidence from the CMB, acceleration of the Universe's expansion, and distribution of baryonic matter. The ΛCDM model assumes that the Universe is comprised of three components: baryonic matter (mass density denoted by Ω_b), cold (non-relativistic) non-baryonic dark matter (CDM, with mass density denoted by Ω_c), and finally a component of dark energy denoted by the cosmological constant Λ.

The power spectrum in Figure 2.4 illustrates the angular distribution (in terms of multipole, l) of temperature anisotropies in the CMB as reported by the Planck

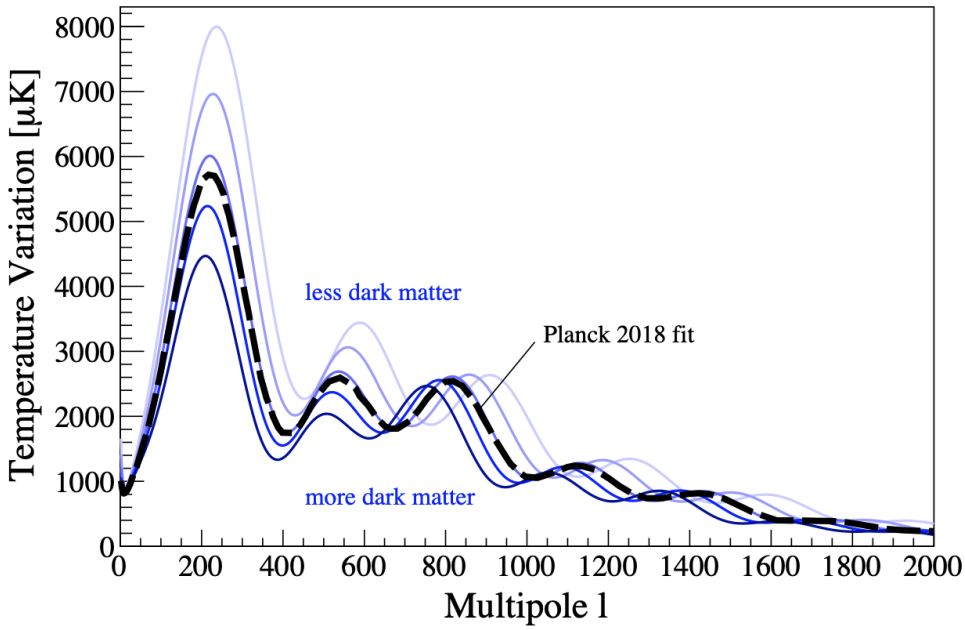

Figure 2.4: The angular power spectrum of anisotropies in the CMB as a function of multipole moment, l [3, 24]. The black dashed line highlights the best of fit result from the Planck experiment (2018). The background blue lines demonstrate variations in the dark matter density ranging between Ω_c of 0.11 and 0.43. Peaks are associated with acoustic fluctuations in temperature and density in the CMB with small l corresponding to large angular scales and vice versa. The third acoustic peak in particular is highly sensitive to the mass density of cold dark matter. Credit: M. Schumann, *Direct detection of WIMP dark matter: concepts and status*, J. Phys. G: Nucl. Part. Phys., vol. 46, pg. 3, 20 Aug. 2019, DOI: 10.1088/1361-6471/ab2ea5.

experiment in 2018 [24]. These anisotropies derive from acoustic fluctuations in temperature (see Figure 2.3) and density in the CMB sky-map. Smaller multipoles are associated with larger angular scales and vice versa, with the first two peaks ($l \approx 200$ and $l \approx 500$) largely defined by the baryonic matter density and the third peak ($l \approx 800$) by the density of CDM.

Fits of the ΛCDM model to the Planck results on the CMB yield a physical baryonic mass density $\Omega_b h^2 = 0.0223 \pm 0.0001$ (where h is the reduced Hubble constant) and a physical dark matter mass density of $\Omega_c h^2 = 0.1191 \pm 0.0009$ [1]. This suggests that the mass density of dark matter in the Universe is 5.34 ± 0.05 times that of ordinary matter.

2.2 Properties and Detection of Dark Matter

Several frameworks have been theorized to explain the "missing mass" problem, including modifications to existing gravitational models (e.g. MOND [18]), but have failed to account for all phenomenological evidence like the Bullet Cluster [20]. Thus, there is strong evidence that the missing mass problem may be accounted for by the presence of non-luminous "dark" matter. The form of dark matter is most commonly viewed as a type of particle, but non-luminous stellar bodies have also been theorized to comprise most, if not all, of the dark matter mass density in the Universe [3]. These objects, referred to as MACHOs (MAssive Compact Halo Objects), consist of stellar masses such as black holes, planets, and low-luminosity stars. However, search campaigns using gravitational lensing in the 1990's by the MACHO Project, amongst other collaborations, were only able to identify enough MACHOs to account for upwards of 20% of the mass of the dark matter halo [25]. The existence of most MACHOs prior to recombination is also impossible, presenting a disagreement with evidence presented in the CMB power spectrum.

2.2.1 Particle Dark Matter

If dark matter is indeed a type, or entire family, of particles, from observational evidence there are a set of properties that such particle(s) likely adhere to:

- General inability to interact with Standard Model (SM) particles through electromagnetic or strong force couplings, and are thus likely electromagnetically neutral (carry zero electromagnetic charge) [26].
- Ability to interact gravitationally and possibly via the weak nuclear force and or new, unknown forces beyond the SM.
- Are non-relativistic (cold) (applies to most, if not all DM particles) with lower kinetic energies, as derived from the ΛCMB model [3].

- Stable over cosmological time scales [27].

Within this framework, a host of proposed particle models for dark matter have been hypothesized as potential candidates. A graphical list of several candidates and their respective mass regimes are illustrated in Figure 2.5.

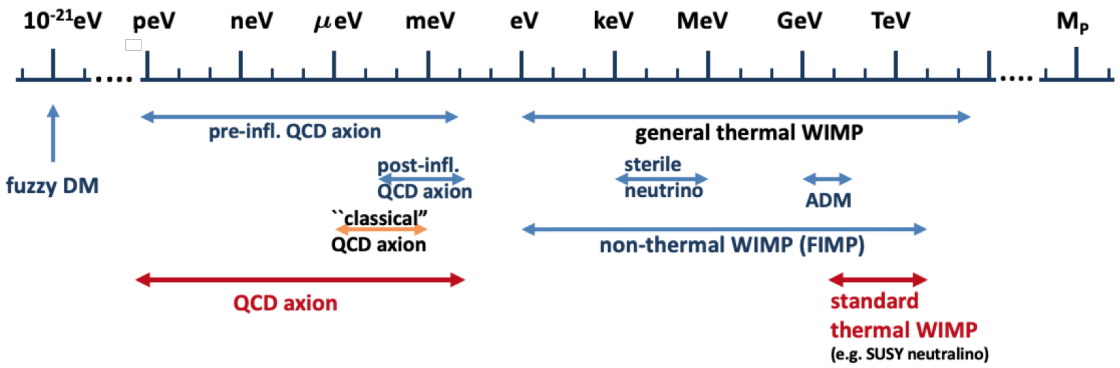

Figure 2.5: A graphical list of modern particle dark matter candidates over different mass scales ranging from 10^{-21} eV (note that units of particle mass in eV/c^2 are abbreviated to eV) to reduced Planck mass-scales ($M_p \sim 10^{18}$ GeV) including SUSY thermal WIMPs and QCD axions (in red) [28]. In blue are highlighted other candidates including general thermal WIMPs and specific classes of axions. In orange highlights the "classical" QCD axion mass regime. Credit: J. Billard *et al.*, *Direct detection of dark matter - APPEC committee report*, Rep. Prog. Phys., vol. 85, pg. 13, 29 Apr. 2022, DOI: 10.1088/1361-6633/ac5754. ©IOP Publishing, Ltd. Reproduced with permission. All rights reserved.

One of the more popular categories of particle dark matter candidates are Weakly Interacting Massive Particles (WIMPs) [2, 3]. These are theorized particles encompassing those which interact gravitationally and via the weak nuclear force (or possibly an even weaker, non-SM force). WIMPs and methods used for detecting WIMPs, amongst other particle candidates, will be the main subject for the remainder of this chapter. Apart from WIMPs, another popular candidate is the QCD axion (often shortened as just 'axion'); a possible lighter CDM particle hypothesized to solve the strong charge parity (CP) problem in quantum chromodynamics (QCD) [3, 29]. Similarly to WIMPs, and as shown in Figure 2.5, axions may inhabit different mass regimes depending upon varying theoretical paradigms; the "classical" regime ranges

from $\sim 1\,\mu$eV to ~ 1 meV (note that we use natural units where $c = 1$ for particle masses) [3]. Other particle candidates include asymmetric dark matter (ADM) [30], fuzzy dark matter [31], sterile neutrinos [32], Feebly Interacting Massive Particles (FIMPs) [33], Strongly Interacting Massive Particles (SIMPs) [34], and WIMPzillas ($M_\chi \geq 10^{12}$ GeV) [35], amongst others [26, 28].

2.2.2 Weakly Interacting Massive Particles

WIMPs were first theorized as a possible dark matter candidate in the 1980's and cover a range of different possible candidates with shared properties [2, 28]. Namely, that WIMPs must interact weakly with SM particles. The first ("standard") thermal WIMPs - produced during the early Universe - were derived from supersymmetry (SUSY), a theoretical extension of the Standard Model which attributes each SM particle to a supersymmetric partner. SUSY particles with lighter mass-scales (e.g., the 'neutralino' [3, 29]) would be the most stable on the order of cosmological time scales which, as popular early WIMP candidates, imply a lower dark matter mass limit on the order of 100 GeV. Such candidates have been shown to have calculated relic dark matter mass densities ($\Omega_c h^2$) consistent with the ΛCDM model [36]. Such a stunning alignment was aptly named the "WIMP miracle" [29]. In the decades since, the lack of evidence supporting SUSY from collider experiments has shifted the focus to other possible candidates such as more general thermally produced WIMPs and the aforementioned QCD axions. This has refined the search to mass regimes as low as $\sim$1 GeV or less.

Despite now encompassing a wide range of energy-scales, there are several common ways to search for evidence of WIMPs (and other particle dark matter candidates). In principle, we focus on three categories of search methods for WIMPs corresponding to one of three interaction channels between WIMPs (and WIMP-like) and SM particles [37]. These channels are summarized in Figure 2.6.

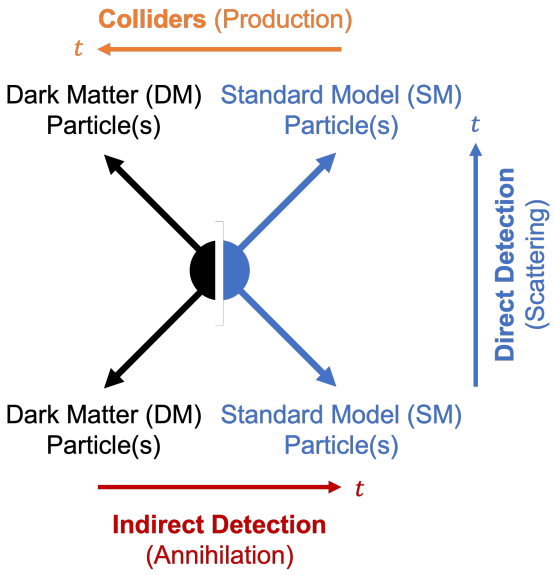

Figure 2.6: A flowchart illustrating the three standard channels by which WIMP-like dark matter could interact weakly with SM particles [3, 26]. Each channel corresponds to a specific detection method including indirect detection (via annihilation), collider experiments (via production), and direct detection (via scattering).

Indirect Detection

Assuming that WIMPs and WIMP-like particles can annihilate with one another through self-interactions, or for WIMPs to go through decay processes into SM particles, then indirect detection is the methodology of trying to observe an excess of said SM particles in regions where dark matter is expected to be abundant. This is primarily performed through observations of high-density regions of dark matter in the Universe (e.g., the centres of some galaxies) by astronomers, measuring excess SM products like high-energy photons from said regions [38]. To date, no significant evidence has been found for indirect dark matter due to the difficulty of distinguishing between dark matter sources and other possible foregrounds.

Collider Production

Another method for detecting dark matter is through the reverse process of annihilation: the production of dark matter particles through the high-energy collisions of SM particles. This could be possible in existing high-energy (order of TeV) parti-

cle accelerators like the Large Hadron Collider (LHC) at CERN [39]. Possible dark matter products from proton-proton collisions would likely not be visible to existing LHC detectors such as ATLAS, but rather a dark matter signal could be deduced from measured missing energy and or momenta in observed SM products [39]. If such absences were to be observed, indirect or direct detection methods could also be employed to corroborate said evidence.

Direct Detection

Direct detection is the third and final method that operates by measuring the energy signatures left by WIMPs scattering off of SM particles [3, 37]. These measurements can be performed using low-background particle detectors; Section 2.3 will go into further details on modern types of detection technologies. Of principal interest is the elastic scattering of WIMPs with the nuclei of target atoms within a given detector. Additional processes such as WIMP-electron scattering have also been a subject of study. The remainder of this section will pertain to the process of WIMP-nucleus scattering and its core role in the development and comparison of direct detection experiments.

2.2.3 Elastic WIMP-Nucleus Scattering

The differential rate, R, at which WIMP-nucleus scattering events are expected to occur within a detector with total target mass M and target nucleus mass m_N is usually presented as [3]

$$\frac{dR}{dE_{nr}} = \frac{\rho_0 M}{m_N m_\chi} \int_{v_{min}}^{v_{esc}} v f(v) \frac{d\sigma}{dE_{nr}} dv, \tag{2.1}$$

where E_{nr} is the nuclear recoil energy, m_χ is the WIMP mass, σ is the scattering cross section, $\rho_0 = 0.3$ GeV/c^2/cm^3 is the local mass density of the Milky Way's dark matter halo near Earth [37, 40], v is the WIMP velocity, and $f(v)$ is the normalized WIMP velocity distribution often described by the Standard Halo Model [41]. To perform this differential rate calculation, one must integrate over all allowable WIMP

velocities. The minimum velocity, v_{min}, is determined kinematically as the minimum WIMP energy required for a nuclear recoil to occur:

$$v_{min} = \sqrt{\frac{E_{nr} m_N}{2} \frac{1}{\mu^2}}. \tag{2.2}$$

In this expression, μ is the reduced mass of the WIMP-nucleus scattering interaction, written as

$$\mu = \frac{m_N m_\chi}{(m_N + m_\chi)}. \tag{2.3}$$

The maximum velocity of a WIMP particle is limited by the escape velocity (v_{esc}) of the Milky Way galaxy's gravitational potential well [3]. This has been roughly calculated to be 533^{+54}_{-41} km/s from sample high-velocity stars [40, 42]. By integrating Equation 2.1, an estimate on the number of observed WIMP interactions, N_χ can be established:

$$N_\chi = \Delta t \int_{E_{low}}^{E_{high}} dE_{nr} \epsilon(E_{nr}) \frac{dR}{dE_{nr}}, \tag{2.4}$$

where Δt is the time exposure of the experiment and ϵ is the detector energy efficiency. E_{low} represents the minimum energy threshold of the detector where as E_{high} is the maximum observable nuclear recoil energy with:

$$E_{high} = \frac{2\mu^2 v_{esc}^2}{m_N}. \tag{2.5}$$

The differential cross section for a WIMP-nucleus scattering event is assumed to be:

$$\frac{d\sigma}{dE_{nr}} = \frac{\sigma_0 F^2(E_{nr})}{4\mu^2 v^2}. \tag{2.6}$$

Here σ_0 is used to express the momentum-transfer independent cross section. $F(E_{nr})$ is known as the nuclear form factor - a Fourier transform of the spatial energy density of the nucleus [37]. σ_0 can be decomposed into two components as $\sigma_0 = \sigma_0^{(SI)} + \sigma_0^{(SD)}$. This expression covers all possible spin-couplings with different nucleons: spin-independent (SI) couplings and spin-dependent (SD) couplings. The SI component is normally expressed as:

$$\sigma_0^{(SI)} = \frac{4\mu^2}{\pi}[Z f_p + (A - Z) f_n]^2 \approx \frac{4\mu^2}{\pi} A^2 f_n^2, \tag{2.7}$$

where f_p and f_n are coupling constants for WIMP-proton and WIMP-neutron interactions respectively, A is the atomic mass of the nucleus, and Z is the atomic number. Usually we assume that both WIMP-proton and WIMP-neutron couplings are equal ($f_p \approx f_n$), then $\sigma_0^{(SI)}$ reduces to the expression on the right of Equation 2.7. For the SD component, the complete expression is composed of two terms:

$$\sigma_0^{(SD)} = \frac{32 G_F^2 \mu^2}{\pi} \frac{J+1}{J} (a_p \langle S_p \rangle + a_n \langle S_n \rangle)^2. \tag{2.8}$$

Here G_F is the Fermi constant, J is the total nuclear spin, and a_p and a_n are the SD WIMP-nucleon coupling constants. Of central importance here are the quantities $\langle S_p \rangle$ and $\langle S_n \rangle$; these represent the expectation values of the proton and neutron spin operators for the total nucleus.

Cross sections are the observable used to compare between different direct detection experiments, as will be discussed further in Section 2.3. Three cross sections are normally cited: σ_{SI} (or sometimes just σ_χ), and then σ_{SD_p} and σ_{SD_n}. These represent the WIMP-nucleon cross sections for SI and SD interactions respectively. To get the WIMP-nucleon cross section for SI interactions (σ_{SI}) we normally just express the simplification of Equation 2.7 as:

$$\sigma_0^{(SI)} = \sigma_{SI} \frac{\mu^2}{\mu_n^2} A^2, \tag{2.9}$$

where now we have included μ_n as the reduced WIMP-nucleon mass (akin to Equation 2.3). For SD interactions [37], the reported cross sections for WIMP-proton interactions are normally reported as

$$\sigma_{SD_p} = \frac{24 G_F^2 \mu_n^2 a_p^2}{\pi} \tag{2.10}$$

and for WIMP-neutron interactions as

$$\sigma_{SD_n} = \frac{24 G_F^2 \mu_n^2 a_n^2}{\pi}. \tag{2.11}$$

The reduced mass, μ_n, represents either a proton (Equation 2.10) or neutron (Equation 2.11) depending upon the relevant equation being used.

The general parameter space for comparing different direct detection experiments for WIMP sensitivity maps specific cross sections (SI or SD) over an experiment's range of sensitivities to different dark matter particle masses, m_χ. The exact sensitivity of an experiment to a WIMP signal is determined by several factors including detector energy thresholds, target medium composition and total active mass, exposure time, overall detector efficiency, and ability to distinguish between SI and SD events [37]. Almost all experiments do not report conclusive evidence of a WIMP signal, rather defining "exclusion" limits - regions of the parameter space that are said to be statistically excluded with the assumption that all observed unknown signal belongs to WIMPs. A handful of experiments (e.g., DAMA/LIBRA [43]) have also defined regions of the WIMP parameter space where they have claimed a potential WIMP discovery [26]. Plots illustrating the SI and SD WIMP-nucleon scattering parameter space with example experimental results are displayed in Figures 2.8, 2.9, and 2.10.

2.3 Status of Direct Detection Experiments

Direct detection experiments have been involved in the search for WIMPs for nearly four decades, as of 2022 [26, 28, 44]. The detector technologies used in today's experiments span a wide array of signal formation mechanisms including heat signatures, charge deposition, and scintillation (see Figure 2.7). Many experiments often make use of multiple signal types as a means of better background discrimination, so these categories are not necessarily all-encompassing of what is possible. However, there are a few core principles that all direct detection experiments must contend with. The most significant is that each experiment must be able to reduce their exposure to background (non-WIMP) sources to optimize their potential witnessing of a predicted exceedingly rare WIMP signal [3, 37]. Shielding is the primary way of reducing backgrounds in experiments. This can be in the form of natural shielding, such as operating experiments in underground laboratories like SNOLAB or the Laboratoire

Souterrain de Modane (LSM). Having a significant layer (over 1 km) of natural earth placed above an experiment reduces exposure to cosmic radiation and other atmospheric backgrounds. Man-made shielding techniques using materials such as lead, water, or polyethylene and the use of radio-pure detector materials and media can also be used to reduce potential backgrounds in the experimental environment or introduced within the detector apparatus itself.

2.3.1 Direct Detection Technologies

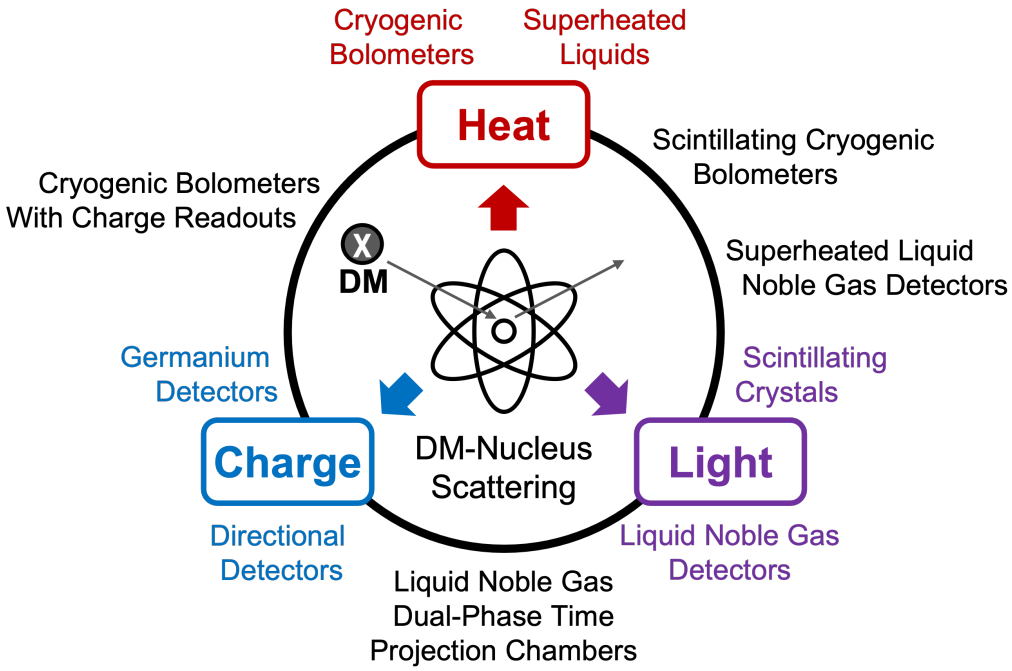

Figure 2.7: Primary signal formation mechanisms for the direct detection of dark matter using different particle detection technologies and media [3, 26, 44].

Charge: Ionization Experiments

Ionization experiments encompass all direct detection experiments which observe the charge signal from ionization products resulting from sufficiently energetic scattering events in a given ionization detector's medium. The general advantage of ionization detectors is that they have low energy thresholds making them ideal for specializing in lighter WIMP mass sensitivity [3, 4, 37]. Examples of pure ionization experiments

include NEWS-G (detailed information provided in Chapter 3) which uses a gas-ionization spherical proportional counter [4]. NEWS-G is capable of detecting energy thresholds of less than the average signal of a single primary ionization electron, ~ 10 eV (more on this in Chapter 3) [45]. With the use of low-A target nuclei, NEWS-G in particular is capable of low WIMP-mass sensitivity. Other ionization detectors make use of silicon charge-coupled devices (CCDs). These include experiments such as DAMIC [46] and SENSEI [47], both of which can attain charge resolutions of less than 1 e^- for up to single electron sensitivity - applicable for low-threshold dark matter searches.

Light: Scintillation Experiments

Scintillation is the process by which, in the case of a particle detector, a target atom (typically a scintillator material) undergoes luminescence when exposed to a sufficiently energetic incident particle. The DAMA/LIBRA experiment [43] uses a crystal matrix of NaI(T) scintillator to measure the annual modulation of WIMPs as Earth's velocity relative to the Milky Way's dark matter halo changes as it orbits the sun. This is the only experiment which has claimed to observe this process, but is inconsistent with several exclusion limits set by other direct detection experiments (see Figure 2.8). Another scintillation experiment is DEAP which operates a liquid-Ar-based scintillator detector, DEAP-3600 [48], at SNOLAB which uses pulse-shape discrimination techniques to identify signals [49].

Heat: Phonon and Bubble Chamber Experiments

There are two main types of heat-based experiments: those which observe phonons in crystal lattice structures and then bubble chamber experiments. Phonon experiments typically make use of bolometry in solid-state cryogenic detectors. Experiments such as SuperCDMS [50] and EDELWEISS [51] are commonly sighted examples also capable of ionization detection, with CRESST [52] a third example that also makes use of

scintillation detection. All three of these experiments are capable of low-mass WIMP sensitivity on the order of ∼0.2 GeV or less using high purity Si or Ge crystals (or $CaWO_3$ in the case of CRESST).

Bubble chambers, such as those used in the PICO [53] experiment, aim at detecting dark matter with a liquid in the superheated state. When a particle deposits enough energy into the metastable liquid, it will create a phase transition between the liquid and gaseous states (vaporization). This results in the formation of bubbles detectable by acoustic and visual signals. A notable advantage of bubble chamber experiments is their insensitivity to electronic recoils on the order of ∼2-3 keV.

Hybrid Experiments

Beyond those already described, there are many more experiments that make use of multiple signal techniques. One popular form of direct detection technology is liquid-noble TPCs (Time-Projection Chambers). Unlike the DEAP experiment, other liquid-noble experiments (which use either an Ar or Xe target) focus on higher-energy WIMPs and can measure both ionization and scintillation. Examples of liquid-noble experiments include LUX [54], DarkSide [55], PandaX [56], and the XENON [57] experiment which currently has the lowest reported SI WIMP-nucleon cross section exclusion limit (see Figure 2.8).

One final exciting new technology is an extension of bubble chambers in the SBC (Scintillating Bubble Chamber) experiment [58]. This experiment plans to use bubble chambers with a scintillator target of xenon-doped argon to add an additional signal formation channel for further background discrimination in comparison to traditional bubble chambers.

2.3.2 Summary and Current Exclusion Limits

As mentioned in Section 2.2.3, comparisons between direct detection experiments are based upon presented results (either exclusion limits, claimed discoveries, etc.)

within the parameter space of WIMP-nucleon cross sections and WIMP masses [26, 40]. An example of such a plot with recent (2021 [28]) SI detection limits for several experiments described in this section is provided in Figure 2.8. For SD limits, Figure 2.9 provides a recent (2022 [52]) selection of results for WIMP-proton scattering, with Figure 2.10 providing a similar current (2022 [52]) selection of results for WIMP-neutron scattering.

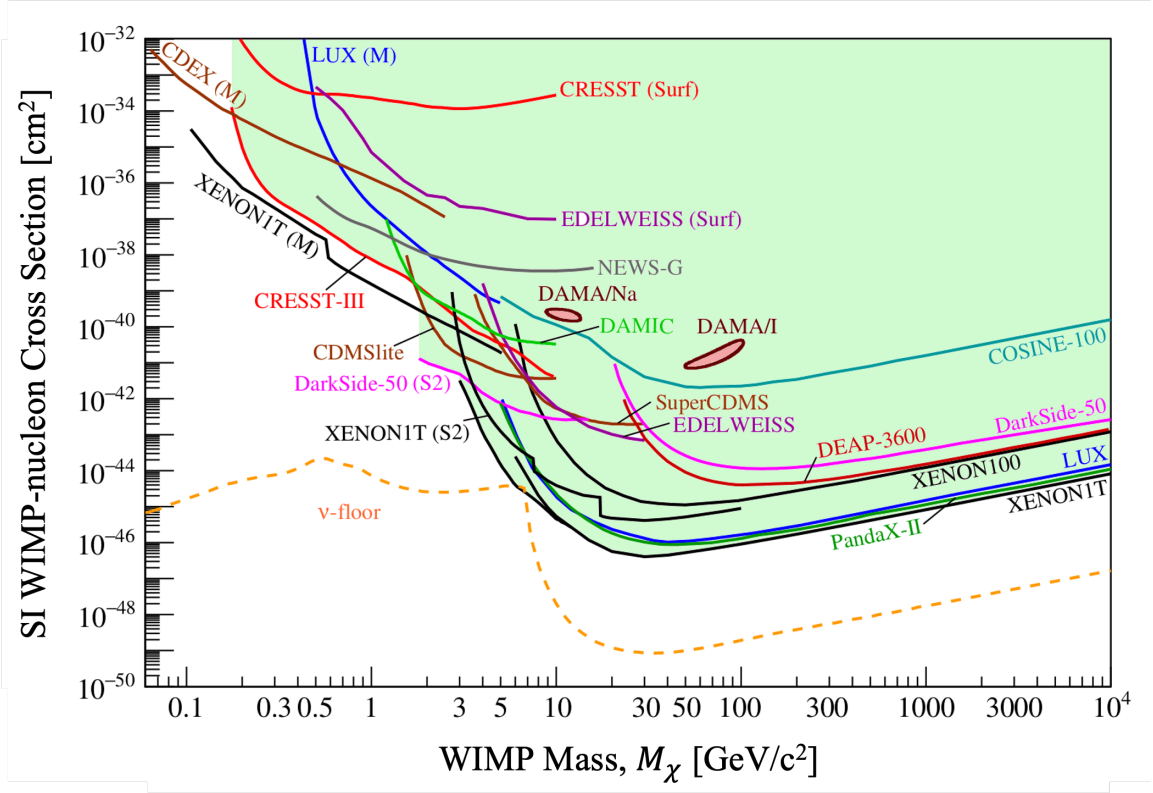

Figure 2.8: 2021 status of direct detection experiment cross section results for spin-independent (SI) WIMP-nucleon scattering as functions of WIMP mass [28]. The neutrino floor (ν-floor) is highlighted in a dashed orange line signalling the parameter space where CEνNS backgrounds are theorized to occur. Credit: J. Billard *et al.*, *Direct detection of dark matter - APPEC committee report*, Rep. Prog. Phys., vol. 85, pg. 19, 29 Apr. 2022, DOI: 10.1088/1361-6633/ac5754. ©IOP Publishing, Ltd. Reproduced with permission. All rights reserved.

As described prior, the exact limits are dependent upon the specific detector technology, energy efficiency, and mass of the target nuclei. In principle, for a given detector technology with sufficiently reduced backgrounds (via appropriate shield-

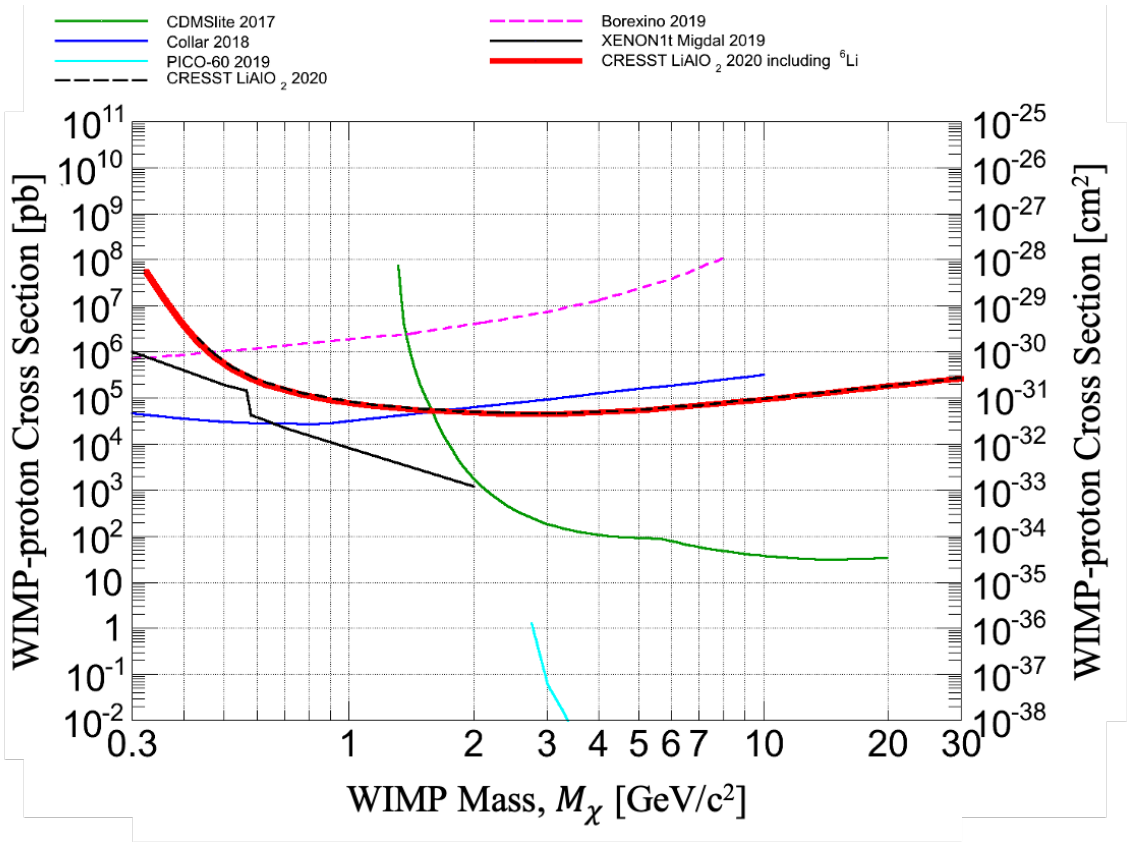

Figure 2.9: Examples of direct detection experiment cross section exclusion limits for spin-dependent (SD) WIMP-proton scattering as functions of WIMP mass [52]. Credit: A. H. Abdelhameed *et al.*, Eur. Phys. J. C, vol. 79, pg. 630, 2019.

ing, data analysis techniques, etc.), the way an experiment can probe to lower cross sections is through either greater exposure times (Δt in Equation 2.4) or by increasing the total target mass (M in Equation 2.1). This is often achieved in modern experiments by the engineering of large detector designs built to support upwards of tonne-scale target masses. This increase in size consequently exposes detectors to higher backgrounds rates which must be offset by ever advancing techniques for background suppression to successfully probe into the smaller cross section regimes.

In the future, as detectors become increasingly sensitive to smaller WIMP-nucleon cross sections, new backgrounds will pose a challenge. As can be seen in Figure 2.8, coherent elastic neutrino-nucleus scattering (CEνNS) may pose a significant background to detectors whose sensitivities reach the low cross section regime known as

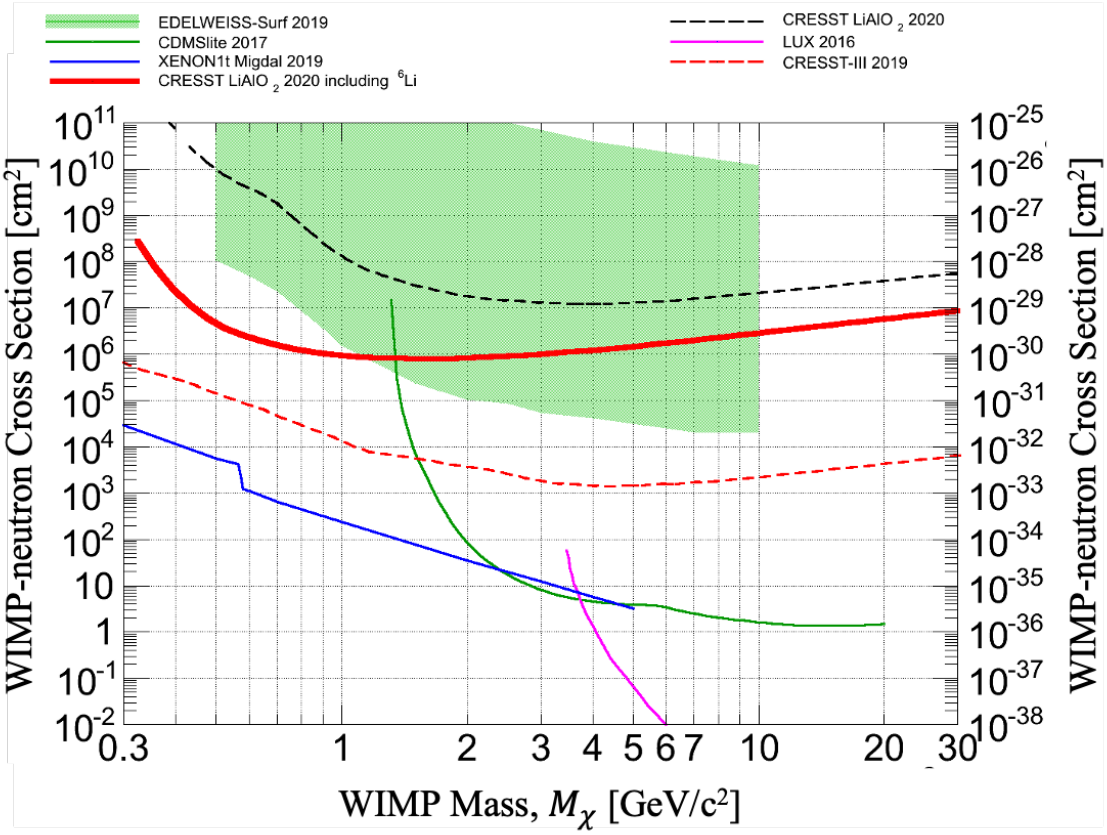

Figure 2.10: Examples of direct detection experiment cross section exclusion limits for spin-dependent (SD) WIMP-neutron scattering as functions of WIMP mass [52]. Credit: A. H. Abdelhameed *et al.*, Eur. Phys. J. C, vol. 79, pg. 630, 2019.

the "neutrino floor" [59]. The neutrino floor represents the region of both the SI and SD parameter spaces where dark matter detectors are theoretically sensitive to these neutrino scattering interactions which form nuclear recoils indistinguishable from those of a theoretical WIMP interaction. The exact cross sections vary with neutrino energy which is related to the origin of a given neutrino (e.g., in order of increasing energy, there exists solar, supernovae, and atmospheric neutrinos). This will pose a new challenge for direct detection experiments which will have to come up with new solutions for discriminating neutrino events since neutrinos are an irreducible background due to the ineffectiveness of shielding against them. One proposed method is the introduction of a directionality channel - the capacity to identify the trajectory profile of incident particles within a given detector. This is already capable

to some degree by directional detectors which measure the trajectories of recoiling nuclei in scattering interactions [60]. For lower WIMP mass regimes, CEνNS backgrounds will be dominated by those originating from the Sun (i.e. solar neutrinos), thus a solar-veto may be able to discriminate these particular interactions as long as the neutrino trajectory can be reconstructed over multiple scattering events. This improved level of WIMP-nucleon scattering cross section sensitivity may allow for dark matter detectors to pursue further physics applications in new studies of these CEνNS interactions. With the capacity to go beyond the neutrino floor, this will continue opening up opportunities to probe the low-mass WIMP parameter space, where the neutrino floor reaches its highest cross section magnitude. In the next chapter, I will focus on one such experiment specializing in this low-mass WIMP regime: the NEWS-G experiment.

Chapter 3

The NEWS-G Experiment

In light of the boom in direct detection experiments searching for dark matter since the 1980s [2], a plethora of detector technologies have been employed to probe the WIMP-nucleon scattering parameter space [2, 3]. One class of detectors centres around the physics of gas ionization; a gas ionization detector measures a signal produced by ionization induced by interacting radiation within the detectors' gaseous volume. Gas ionization detectors have a wide range of applications and are used in fields including nuclear physics and medicine [61]. Since it was first proposed by I. Giomataris in 2008 [62], the New Experiments With Spheres-Gas (NEWS-G) collaboration have specialized in Spherical Proportional Counters (SPCs) - a type of gas ionization detector - for measuring WIMPs in the low-energy, sub-GeV mass regime. Unlike other gaseous detectors, such as the ionization chamber or Geiger-Müller counter [61], SPCs exhibit a characteristic energy response that is proportional to the initial ionization energy of these interactions. This is a consequence of their electric field strength that is tuned such that there is substantial, proportional signal multiplication from a cascade production of secondary ionization events, known as Townsend avalanches [61], towards their central, high-intensity electric field region. This chapter will focus on basic SPC operating principles, signal formation, and introductory signal analysis, as well as provide an overview for the measurement campaigns undergone by the NEWS-G collaboration since 2008 and those planned for the future.

3.1 SPC Operating Principles

An SPC is a gas ionization detector consisting of a hollow grounded metallic spherical vessel. At their centre, a single high-voltage spherical anode - the detectors' sensor - is supported by a grounded rod (e.g., Figure 3.1 (b)). Some examples of the NEWS-G collaboration's SPCs are provided below in Figure 3.1.

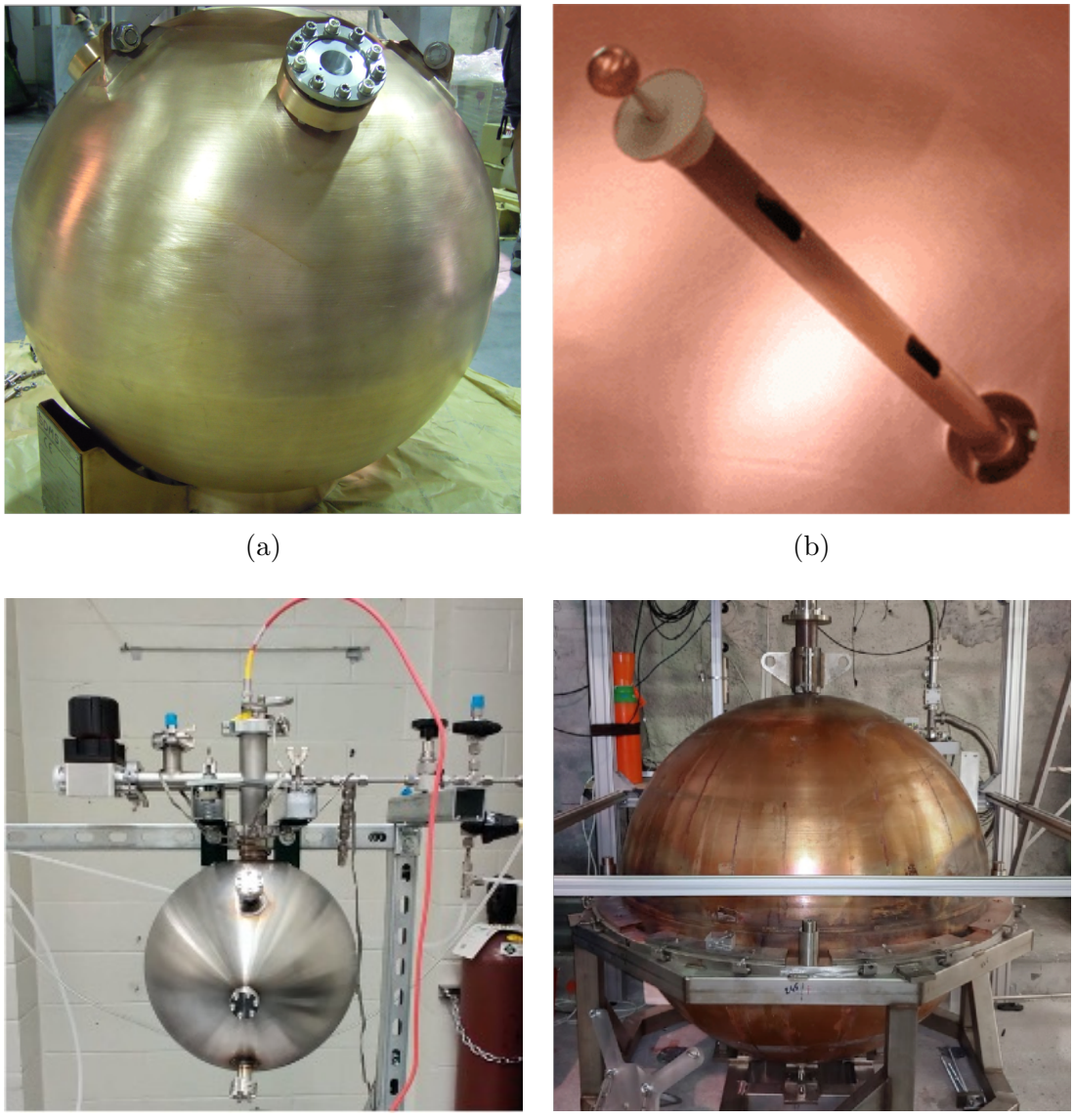

(a) (b)

(c) (d)

Figure 3.1: Example NEWS-G SPCs: (a) SEDINE [4], a 60 cm diameter Cu SPC operated at LSM; (b) an internal view SEDINE highlighting its sensor and rod structure; (c) University of Alberta's 30 cm stainless steel prototype SPC; (d) S140, a 140 cm diameter Cu SPC previously operated at LSM, shown without external shielding.

While the exact detector dimensions and sensor design may vary, as discussed later in Section 3.3, the basic operating principles of each SPC are fundamentally the same. The core feature of SPCs are that they exhibit a near-radial electric field due to the nature of their spherical geometries [63]. In an ideal SPC, we assume an inner detector radius of r_1 and a freely suspended anode (i.e. an anode unsupported by a rod) of radius r_2 set to an electric potential V_0. This creates a perfectly symmetric radial electric field, $\vec{E}$, whose magnitude is expressed as a function of detector radius, r, about the very centre of the SPC:

$$E(r) = \frac{V_0}{r^2}\rho, \text{ where } \rho = \frac{1}{r_2} - \frac{1}{r_1}. \tag{3.1}$$

In reality, due to the presence of the grounded rod supporting the anode, the electric field becomes warped, in particular near the rod, to where it can no longer be represented analytically. Therefore, for characterizing the electric field, the use of finite element software, such as COMSOL Multi-physics® [64], can be used to calculate $\vec{E}$ as seen in Figure 3.2. Further detail on the applications of such finite element software in modelling SPC electric fields will be discussed in Chapter 4.

The active volume of an SPC is typically filled with an inert gas target with noble gases such as helium, neon, and argon being most commonly used. The choice of fill gases and their properties will be discussed later in Section 3.2.1.

With the SPC structure, electric field, and fill gas in mind, Figure 3.3 illustrates the basic detection principle of an SPC from primary ionization (1) to signal formation (4). When incident radiation, such as an energetic WIMP, interacts with the detector (e.g., via elastic scattering with target nuclei in the fill gas), a process called "primary ionization" may occur. A given ionization event may happen either at a localized point (e.g., neutral particles) or over a sizeable path length (e.g., charged particles). Regardless of its distribution, several primary electrons will be released into the gas (more on this will be discussed in Section 3.2.2) which will begin to drift towards the central anode. As the primary electrons drift, interactions with other gas molecules

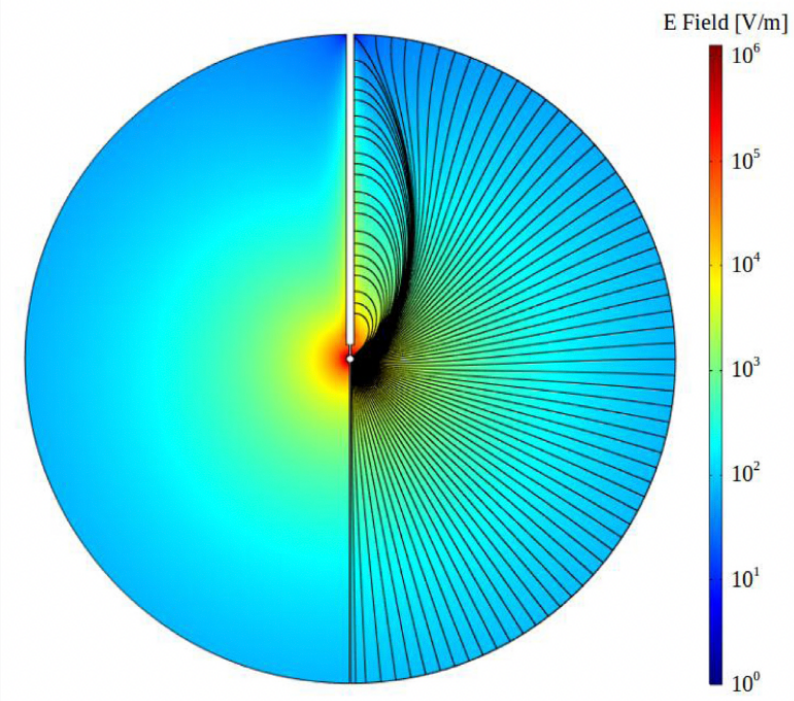

Figure 3.2: A cross-sectional view of SEDINE's (Figures 3.1 (a) and (b)) electric field using COMSOL Multiphysics® software [64, 65]. The right side of the detector is shown with an overlay of electric field lines in black, illustrating the warping effect of the rod. V_0 in this simulation is set to 2.52 kV with the rod and inner detector surface set to 0 V (i.e. grounded) [4].

will result in diffusion, introducing a level of variability in the electrons' drift, and thus arrival times at the anode. Once sufficiently close to the anode (approximately < 1 mm away), the electric field strength will accelerate the primary electrons to where they reach a critical kinetic energy such that each electron produces a cascading secondary ionization process known as a "Townsend avalanche" [61]. This process can result in the creation of thousands of secondary electron-ion pairs depending upon the amplification gain, determined by the specific detector geometry and sensor voltage. Primary and secondary electrons are then collected by the anode while the secondary ions begin a slow drift radially outwards towards the detector's inner surface. These drifting secondary ions induce a measurable current on the sensor that is considerably larger than the electronic charge current due to their long drift period as they move towards the vessel's inner surface. The induced current, which form

observable current "pulses", is proportional in amplitude to the initial ionization energy of the given event. These pulses are passed through a pre-amplifier stage before being read off as voltage pulses by a data acquisition system (DAQ). More on the signal formation process (4) will be discussed in Section 3.2.2 along with signal characteristics and processing in Section 3.2.4.

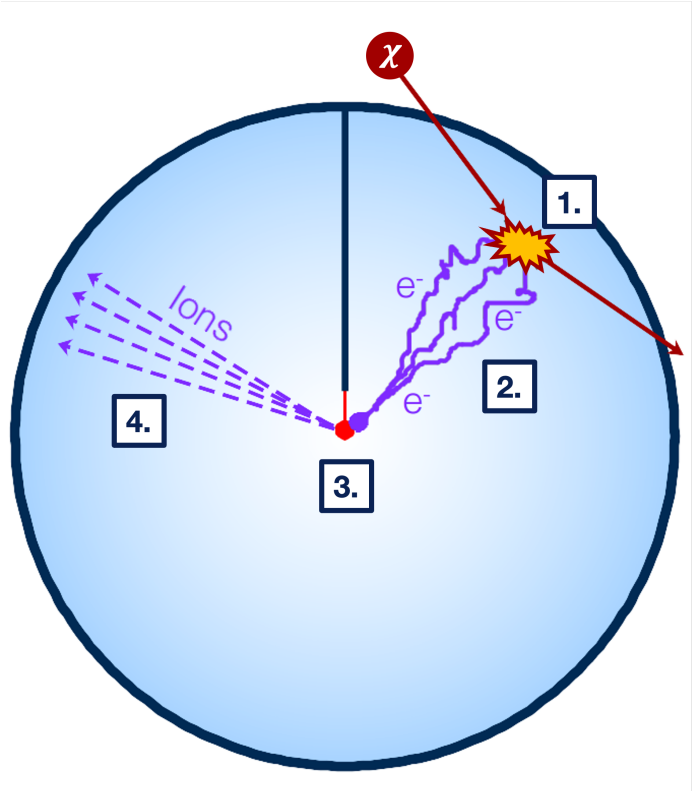

Figure 3.3: A simplified diagram of the basic SPC detection principle. (1) An energetic particle (e.g., a WIMP - labelled by χ) produces a number of primary electrons (PEs) through "primary ionization". (2) The PEs drift towards the central anode, exhibiting some amount of diffusion through interactions with the gaseous medium. (3) A Townsend avalanche occurs once primary electrons are sufficiently close to the anode (approximately < 1 mm away) [61]. (4) Secondary ions created during the avalanche drift away from the anode, inducing a measurable current signal on the sensor proportional to the initial ionization energy.

3.2 SPC Gas and Signal Properties

3.2.1 Fill Gases and Impurities

The choice of fill gas for an SPC has many considerations, mostly concerning the energy response behaviour of incident radiation, but here I will first focus on two key factors: it needs to act as a suitable target to optimize sensitivity to low-mass WIMP-nucleon scattering interactions, and it should minimally interfere with the drift of primary electrons. Naturally, this leads to noble gases serving as the primary choice of fill gas for SPCs. Due to their full valence shell of electrons, noble gases have ideal chemical properties preventing them from interacting with drifting electrons apart from diffusive collisions. As mentioned prior, most SPCs use either neon or argon due to their regular availability, affordability, and favourable SPC behaviour compared to other cheap alternatives like helium. Depending upon the specific WIMP mass regime of interest, going to even lighter target atoms such as with helium or hydrogen is required to probe the lower energy regime of the WIMP-nucleon parameter space [3]. In addition to the primary fill gas, SPCs may also require a small percent of a secondary "quencher" gas and are often subject to impurities which will be discussed next.

Gas Quenching

In practical use, SPCs typically require a mixture of gases rather than just a single fill gas. Generally, a secondary "quencher" gas making up a few percent ($\leq$10%) of the total gas mixture is included as well. The purpose of a gas quencher is to maintain the inherent proportionality of the SPC signal [4]. This gas prevents tertiary low-energy ionization events caused by electrons and photons produced during the recombination of secondary ions with free electrons on the inner surface of the detector. Gas quenchers require sufficient energy absorption features (e.g., via rotational or vibrational modes) to absorb the energy of these tertiary particles, preventing a perpetual

state of ionization [61]. Typically, hydrocarbon molecules behave sufficiently as gas quenchers with CH_4 being the most common choice for NEWS-G's SPCs.

Gas Impurities

Despite best efforts to ensure high gas purity through different purification methods (discussed later in Chapter 6), contaminant gases are still an ever present nuisance in SPCs. There are two forms of impurities of interest: radioactive backgrounds and electro-negative "trapping" gases. The radioactive backgrounds present within the fill gas, such as radon, include any radioactive contaminants present within the active gas when the chamber is initially filled or as a consequence of out-gassing from the detector's inner surface. Radio-purifying techniques such as radon trapping before injecting gas into the detector are used to minimize the introduction of airborne radiochemical impurities [66]. For surface contamination, extensive cleaning of all material surfaces both inside the main detector and gas handling systems are undergone before deployment and operation [5]. Advanced techniques such as ultra-pure copper electroplating are even used in NEWS-G's recent large SPCs like S140 (see Section 3.3.2) [67].

Highly electro-negative contaminant molecules also also affect the signal by "trapping" drifting primary electrons, preventing them from reaching the anode. The most notable contaminant is oxygen which, with only a small concentration, can significantly reduce the charge of observed event signals. The longer a primary electron has to drift to reach the anode, the greater the likelihood of becoming trapped by one of these molecules. Therefore, there is a clear relationship between energy loss due to trapping and an event's radial origin within the detector, as discussed in further detail in Chapter 4. To reduce these contaminants, filters (e.g., a "Getter") can be used prior to filling the detector. Exposing the SPC to high temperatures to "bake" the detector can also be an effective method at removing surface contaminants prior to filling.

3.2.2 Signal Formation

Primary Ionization

When an ionizing particle interacts with the gaseous medium of an SPC, some number of primary electrons will be produced. The principle determining factor which governs the exact number of freed primary electrons is known as the ionization energy, referred to as the "W-value" [4]. W represents the mean energy required to create a single electron-ion pair, specific to the gaseous medium. For a given ionization interaction, the number of primary electrons is a stochastic process with a mean $\mu = E/W$, where E is the deposited energy of the ionizing particle. There is a bit more nuance when it comes to W in the context of nuclear and electronic recoil events. For nuclear recoils, we introduce a quantity Q called a "quenching factor" (unrelated to gas quenching). Q represents the ratio between the mean ionization energies of both recoil types, with characteristically $Q < 1$ for nuclear recoils. Since a WIMP ionization event would occur via nuclear recoil, Q is a principle quantity that must be known for the given target gas. Entire (ongoing) campaigns have been performed by the NEWS-G collaboration dedicated to the measurement of Q for different gas mediums [68]. Two unique energy scales are also often used to distinguish between the ionization energy of the event and the true nuclear recoil energy. These are eV_{ee} ("electron-equivalent") and eV_{nr} (nuclear recoil) respectively.

W_{nr}, the W-value for nuclear recoils is written as $W_{nr} = W_{er}/Q$, where W_{er} is the W-value for electronic recoils. For NEWS-G, W_{er} has been expressed empirically as the following parametrization [4, 69]:

$$W_{er} = \frac{E_{er}}{E_{er} - U} W_0, \tag{3.2}$$

where U is the ionization potential of the gas, E_{er} is the electronic recoil energy, and W_0 is the "fundamental" W-value. In the high energy limit where the electronic recoil energy is large ($E_{er} >> U$) we find $W_{er} \approx W_0$; when stated in this thesis, W-values will refer to this fundamental unquenched ionization energy as this is normally the

value used when discussing W-values in literature.

As mentioned, the exact number of primary electron-ion pairs produced is stochastic. If such events were truly independent then primary ionization would exhibit Poissonian behaviour. However, studies of the primary ionization process in gas ionization detectors have found that the variance, σ_N^2, of such a distribution is actually characterized by the "Fano factor", F [70] - a characteristic property of the gas medium defined as

$$F = \frac{\sigma_N^2}{\mu}, \tag{3.3}$$

where F by definition is less than one for non-Poissonian ionization processes [71]. Consequently, the probability distribution found to more accurately account for primary ionization in SPCs is known as COM-Poisson [71–73]:

$$P(N|\lambda,\nu) = \frac{\lambda^N}{(N!)^\nu}\frac{1}{\sum_{s=0}^{\infty}\frac{\lambda^s}{(s!)^\nu}}. \tag{3.4}$$

Here ν and λ are simply control parameters for μ and σ_N^2 of the given distribution, and thus F (Equation 3.3). Therefore, for a known F and μ, one can determine an appropriate choice in ν and λ to determine the appropriate form of COM-Poisson expression.

Townsend Avalanche and Signal Amplification

Once primary electrons successfully drift towards the central anode, the cascading secondary ionization process previously mentioned as a "Townsend avalanche" will occur [61]. During this process, a single primary electron accelerated by the electric field close to the sensor is energetic enough to induce further ionization, resulting in the production of thousands of secondary electron-ion pairs. The process which governs the number of secondary electron-ion pairs produced for a single primary electron is described empirically by the Polya distribution [45]:

$$P_{polya}\left(\frac{n}{\langle n\rangle}|\theta\right) = \frac{(1+\theta)^{(1+\theta)}}{\Gamma(1+\theta)}\left(\frac{n}{\langle n\rangle}\right)^{\theta} e^{-(1+\theta)\frac{n}{\langle n\rangle}}. \tag{3.5}$$

Here $n/\langle n \rangle$ is the ratio of the number of produced secondary electron-ion pairs, n, to the average gain of the specific detector, $\langle n \rangle$. θ is a shaping parameter for the distribution that is found to be close to zero for SPCs, giving the Polya distribution a generally exponential profile (or a normal distribution when $\theta >> 1$) [45, 72]. This formula can be expanded upon to predict the number of secondary electron-ion pairs produced by N primary electrons by taking the N^{th} convolution of the Polya distribution. This, combined with the primary ionization model discussed earlier in this section, governs the energy response of the detector [4, 63]. Additional factors can come into play including via the effect of electron "trapping" (see Section 3.2.1). This occurs when highly electro-negative molecules (e.g., O_2) "trap" drifting primary electrons through electron attachment. This can reduce the energy efficiency of an SPC, particularly for events originating at greater radii. In Chapter 4 we will discuss this process in greater detail.

Induced Signal and Pre-amplifier Response

With the production of thousands of secondary electron-ion pairs, the slow drift of the secondary ions will induce a current, I_{ind}, onto the sensor - the primary driver of an SPC's measurable signal. The differential of induced charge due to a drifting ion near the sensor, dQ_{int}, is governed by the Shockley-Ramo theorem [63]:

$$dQ_{ind}(t) = -q_{ion}\frac{E(r)}{V_0}v_{ions}dt, \tag{3.6}$$

where q_{ion} is the ion's charge and v_{ions} is the ion's velocity. Using appropriate substitutions, we can re-express this as a time-dependent induced current on the sensor using Equation 3.1 and the expression for ion mobility, $\mu = \mu_0/P$, where $\mu E(r) = v_{ions}$ [63]:

$$I_{ind}(t) = \frac{dQ_{ind}}{dt} = -q_{ions}\alpha\rho(r_2^3 + 3\alpha t)^{-\frac{4}{3}}, \tag{3.7}$$

where α is

$$\alpha = \mu_0\frac{V_0}{P}\rho. \tag{3.8}$$

Here μ_0 is the ion mobility for the gas at normal pressure and temperature and P is the pressure of the gas. We also made use of the substitution $r^2 dr = \alpha dt$. Integrating both sides for $[r_2, r]$ and $[0, t]$ yields $r = (r_2^3 + 3\alpha t)^{1/3}$, as included in Equation 3.7. This time-dependent current pulse is fed through a pre-amplifier (e.g., a CREMAT charge pre-amplifier [74]) circuit which typically has an exponential response. The DAQ in use with the given SPC will observe a voltage signal, $S(t)$, from the pre-amplifier stage that is simply the convolution between the pre-amplifier's exponential response and $I_{ind}(t)$:

$$S(t) = -q_{ions}\alpha\rho e^{-\frac{t}{\tau}} \int_{t=0}^{t=t_{max}} e^{\frac{u}{\tau}} (r_2^3 + 3\alpha u)^{-\frac{4}{3}} du, \tag{3.9}$$

where τ is the pre-amplifier decay time. The time span over which this expression is integrated concerns the drift period of the secondary ions. The maximum drift time occurs when an ion's radial position is equal to r_1 - at the inner surface of the detector - when the ion finally recombines with free electrons at the detector's surface [63]. The upper limit on the ion drift time, t_{max}, is determined by solving for t when $r = r_1$ in $r = (r_2^3 + 3\alpha t)^{1/3}$:

$$t_{max} = \frac{r_1^3 - r_2^3}{3\alpha}, \tag{3.10}$$

with t_{max} being on the order of 10 s (as calculated for the SEDINE detector [63]).

3.2.3 Detector Calibration

To assess an SPC's energy response and linearity, several calibration sources and methods have been used and developed by the NEWS-G collaboration [45]. Aside from more common radioactive sources placed externally near the detector (e.g., ^{55}Fe and AmBe), there are two primary sources used with NEWS-G detectors: ^{37}Ar and a 213 nm UV laser.

^{37}Ar Calibration

^{37}Ar is a gaseous radioisotope of argon with a half-life of just over 35 days [75]. ^{37}Ar decays via electron capture, emitting low-energy X-rays and Auger electrons which

total to observable energy peaks in SPCs at 0.27 keV and 2.82 keV [45]. An example energy spectrum of ^{37}Ar as recorded with a 30 cm SPC is shown in Figure 3.4. The advantage of ^{37}Ar is that it has a gaseous form, diffusing uniformly throughout the detector volume and allowing for observable events originating from the entire fiducial volume. Since both primary energy peaks are known, ^{37}Ar can be used to both calibrate the observed digital-to-analog energy scale in treated signal pulses (see Section 3.2.4) and validate an SPC's energy-response linearity.

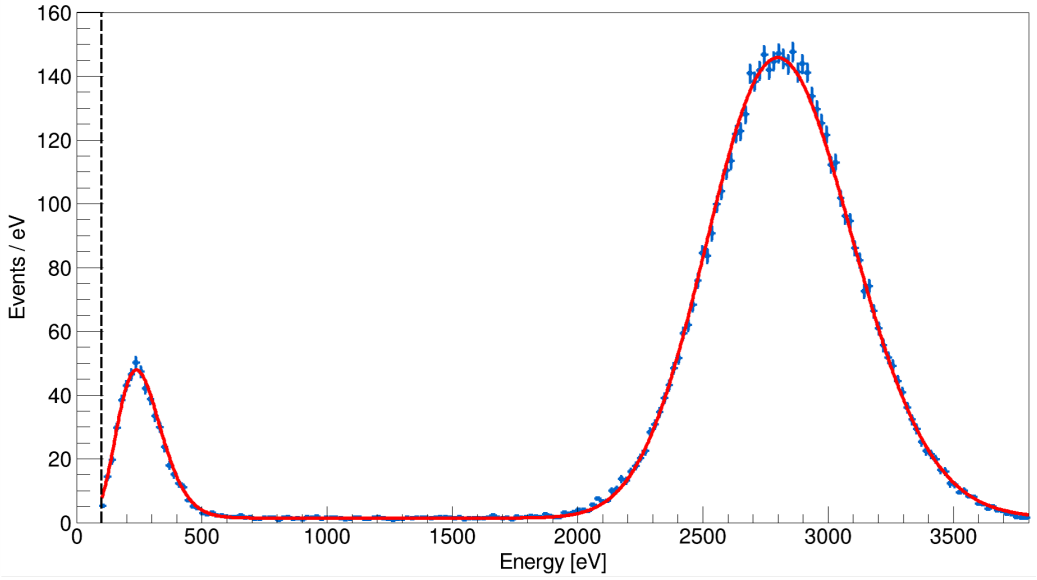

Figure 3.4: Example ^{37}Ar calibration energy spectrum as obtained with a 30 cm SPC [45]. The two spectrum peaks represent the primary measured ^{37}Ar X-ray decay peaks at 0.27 keV and 2.82 keV respectively.

Laser Calibration

One of the most important calibration sources used with NEWS-G's SPCs are solid state lasers capable of producing pulsed 213 nm UV light. The purpose of these lasers are to shine controlled pulses of UV light onto the inner surface of the detector, exciting photo-electrons from the metallic surface via the photoelectric effect. A split fibre is used to feed the UV laser output into both an optical port on the SPC as well as a silicon photodetector, as seen in the typical apparatus presented in Figure 3.5. The photodetector acts as a trigger such that "laser events" can be recorded each

time a pulse is fired. The UV lasers are an insightful tool in particular for low-energy calibration, including in the study of the single-electron response of SPCs [45]. By sufficiently lowering the intensity of the laser pulses such that statistically an average of one or less photo-electrons are excited per pulse, single-electron events and their characteristics are able to be studied. In fact, the study of single-electron events have been used for the characterization of the Polya distribution (Equation 3.5) and the study of surface electron drift times.

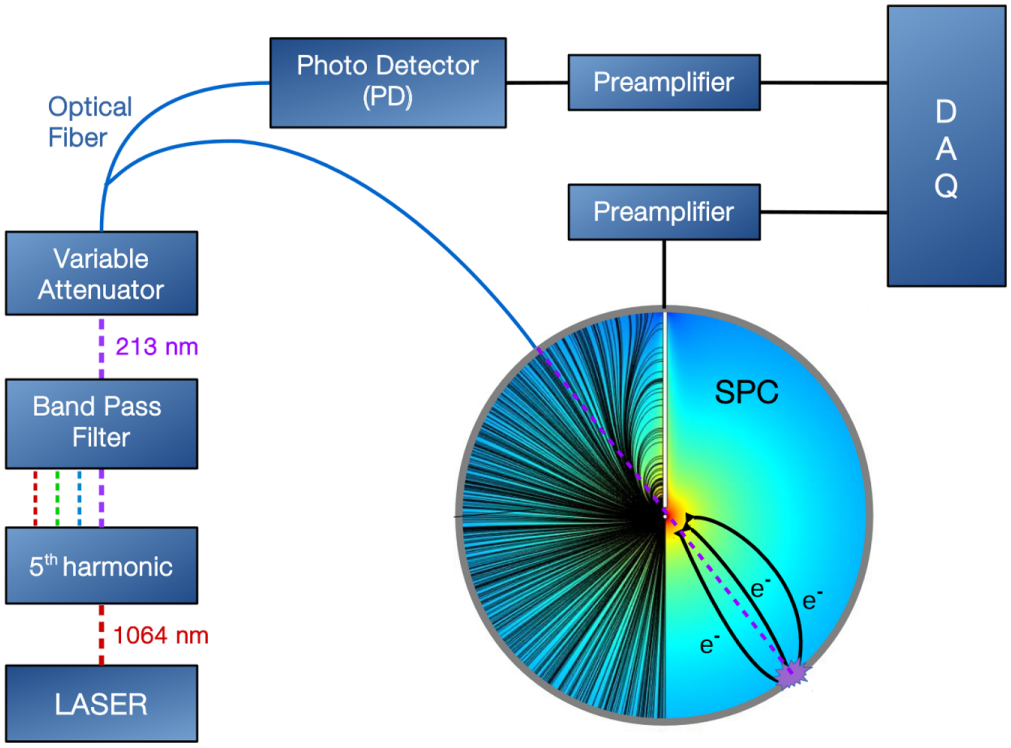

Figure 3.5: Apparatus schematic for low-energy calibrations with a solid state 213 nm UV laser (bottom-left) and an SPC [45]. Laser pulses are fed into the SPC via one end of a split optical fibre such that the pulses shine onto the inner surface of the detector, exciting photo-electrons. Events are then tagged by sending the other end of the split fibre to a photodetector (PD).

3.2.4 Signal Pulses and Pulse Treatment

Measured SPC pulses, as recorded from the pre-amplifier by a DAQ, are labelled as "raw" pulses with a vertical scale in analog-to-digital units (ADU). At this stage with

the untreated pulses, there are preliminary pieces of information that can be extracted including the "raw" signal amplitude and rise time [76]. Rise time, typically labelled as 10%-90% rise time (or 10%-75% rise time when working with shorter diffusion times, like when using neon), is a measure of the time interval for the pulses to reach 90% (or 75%) of their maximum amplitude relative to 10%. This measure is related to the diffusion of a particular event, with both properties being correlated to the event's radial origin within the SPC. Example baseline-corrected "raw" pulses are illustrated in the top row of Figure 3.6.

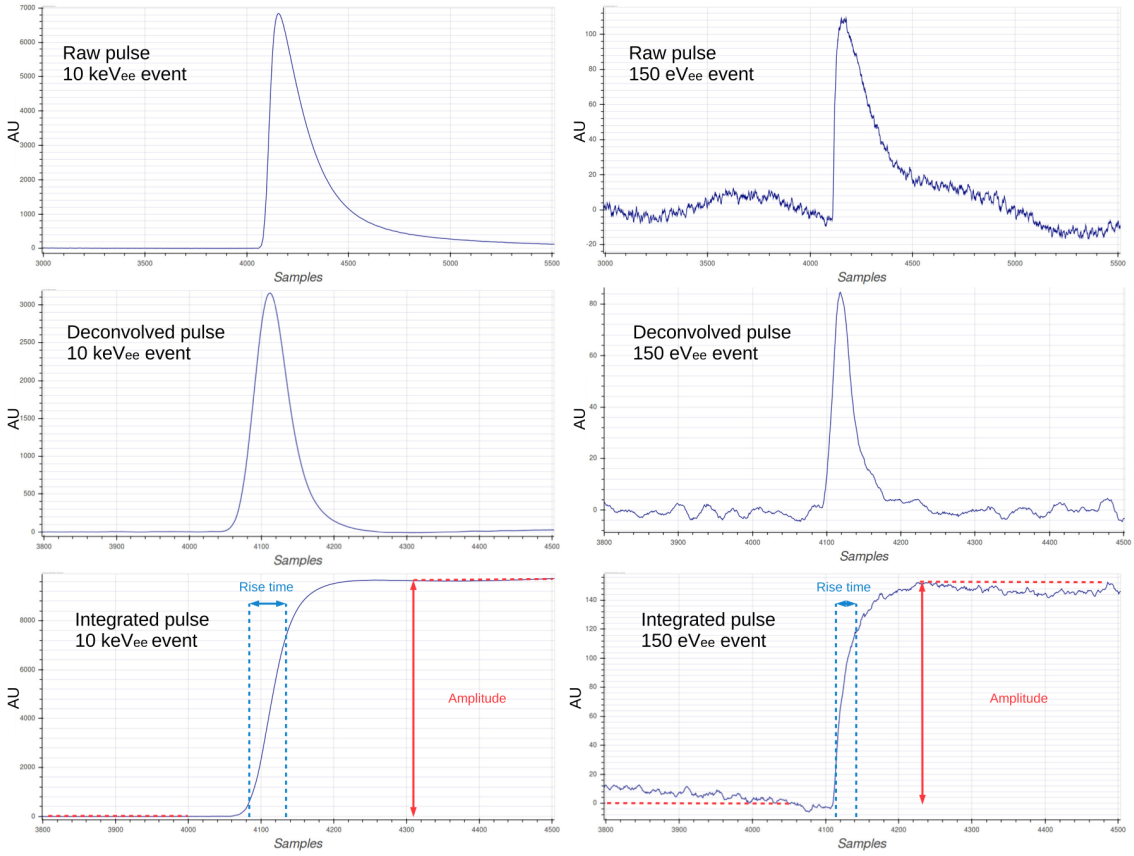

Figure 3.6: Pulse treatment steps (top-to-bottom) for example 10 keV_{ee} and 150 eV_{ee} pulses [4]. The time-window for these plots are recorded as 'samples' where one sample is equal to 480 ns. (Top) Raw pulses as recorded from the pre-amplifier in arbitrary units (AU). (Middle) Intermediary treated pulses after an applied trapezoidal filter and doubly deconvolved [76]. (Bottom) Fully treated integrated pulses exhibiting "step"-like behaviour; amplitude in AU and 10%-75% rise time are illustrated.

Raw pulses are a consequence of the original induced current pulses being convolved

with the exponential pre-amplifier response. Consequently, the pre-amplifier response can result in a loss of information, particularly in high-diffusion events [76]. Therefore, a deconvolution process is applied to treat pulses and better assess the aforementioned parameters.

Once the baseline is corrected using a simple horizontal linear fit on the end behaviour of the recorded pulse window, the entire pulse is smoothed with a trapezoidal filter. This reduces the effect of high-frequency fluctuations and improves the signal treatment process in subsequent steps. From here a double deconvolution is performed for both the pre-amplifier response and the ion-induced current response of the detector [76]. The resulting doubly deconvolved pulses, as seen in the middle row in Figure 3.6, appear as short impulses which correspond to the arrival times of primary electrons. The last step, as seen in the bottom row of Figure 3.6, is to perform a cumulative integration of all of the impulses in the deconvolved signal window. This yields a series of approximate step functions (or one large step function if there was minimal diffusion) with an amplitude proportional to the number of secondary electron-ion pairs created, and thus the event energy. The rise-times calculated from these fully treated pulses (either 10%-90% or 10%-75%) are still proportional to the event's diffusion and radial origin within the detector.

3.3 NEWS-G and the Search for Light WIMPs

Since first proposed in 2008 [62], the NEWS-G collaboration has expanded to operations in Canada, France, the United Kingdom, Greece, and the United States. Collaborators represent institutions including Queen's University, University of Alberta, CEA Saclay, LPSC Grenoble, Aristotle University of Thessaloniki, and the University of Birmingham, amongst others. Here I will discuss some of the principal experimental campaigns by the collaboration since its inception and some of the future SPC detectors currently in development across the globe. Particularly relevant to this thesis, there will be a greater focus on the detector called S140 (a.k.a.

"SNOGLOBE") - a 140 cm diameter SPC first operated at the Laboratoire Souterrain de Modane (LSM) in Modane, France and currently undergoing commissioning at SNOLAB in Sudbury, Ontario.

3.3.1 SEDINE

The first true dark matter measurement campaign undergone by the collaboration was performed during the spring of 2015 with an SPC detector called SEDINE [4]. SEDINE is a 60 cm diameter prototype SPC that made use of a 6.3 mm diameter ball sensor; SEDINE plus its sensory equipment are pictured in Figures 3.1 (a) and (b) respectively. The detector was made with ultra-pure copper and was commissioned at the aforementioned LSM where it successfully recorded 9.7 kg·days worth of data using 3.1 bar of a Ne + 0.7% CH_4 gas mixture. The natural rock shielding at LSM (4800 meter water equivalent (mwe) thickness) plus the use of 15 cm of lead and 30 cm of polyethylene shielding, all contributed to reductions in external backgrounds during the experiment's run-time. NEWS-G published its first results for WIMP-nucleon cross section exclusion limits using SEDINE's data in 2017. This exclusion limit curve can be seen in Figure 3.11, coloured in light green.

3.3.2 S140

Due to the successful campaign with SEDINE, the exploration of a larger detector geometry - the common progression for most direct detection experiments - was the natural next step for the NEWS-G collaboration. In 2018, it was proposed that an effort would be made to install a larger, 140 cm diameter SPC at SNOLAB - a deeper laboratory than LSM, ∼2 km underground (∼6000 mwe) in Creighton Mine located in Greater Sudbury, Ontario.

A concept 3-D CAD model rendering of this new detector, called S140, is pictured in Figure 3.7. This larger 140 cm SPC is composed of ultra-pure (∼99.99%) copper, with an internal ∼0.5 mm formed using advanced electroplating techniques for providing

internal shielding against radiation from the copper vessel [67]. As seen in Figure 3.7, there are two types of shielding used with S140. The first layer of shielding consists of 25 cm of lead with the innermost 3 cm comprising of more radio-pure, low-activity archaeological lead recovered after ∼2000 years from the bottom of the Mediterranean Sea in Roman shipwrecks. The second layer of shielding is made up of 40 cm of high-density polyethylene, manufactured at the University of Alberta.

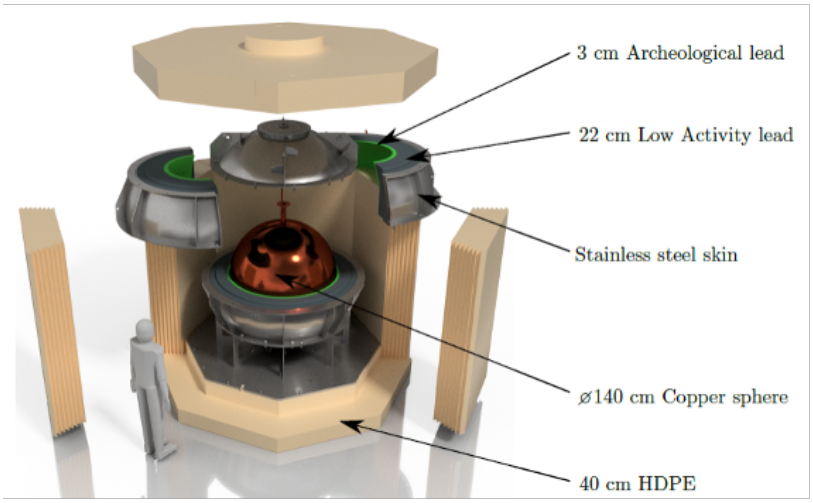

Figure 3.7: 3-D CAD rendering of the 140 cm diameter copper SPC, called S140 (nicknamed "SNOGLOBE"). This cutaway model highlights the layers of shielding made of polyethylene and lead (including low-activity archaeological lead) surrounding the SPC.

The ACHINOS Sensor

Given the overall size of S140, one concern over the use of the traditional single-anode ball sensors was that the SPC drift volume would not scale appropriately with larger detector volumes. This is because of how the electric field intensity significantly drops at larger radii; this reduces the detector's fiducial (active) volume and results in the slower drift of primary electrons. This perhaps could even lead to the incidence of "rogue" electrons with highly delayed arrival times at the sensor relative to their production. Increasing the radius of the sensor (r_2) was one proposed solution - a larger radius more optimally scales the electric field intensity at the surface, but

reduces the overall gain (signal amplification) of the detector. Alternatively, a greater applied electric potential (V_0) could increase the field's strength by improving the field gradient near the anode, increasing the sensor gain, but leaves the sensor prone to sparking and damage. Too high of an electric field also poses the risk of the SPC losing its proportionality and turning into a Geiger counter [61].

The proposed solution by collaborators in Greece at the Aristotle University of Thessaloniki was a multi-ball sensor dubbed an "ACHINOS" (the Greek word for 'sea-urchin') [77]. While having gone through several iterations and prototypes, the current ACHINOS design consists of eleven individual $\sim$0.85 mm diameter anodes held about the geometric centre of the detector [78]. An example image of the current ACHINOS design is presented in Figure 3.8 (left) along with an electric-field plot (right) for an applied HV of 2.03 kV. The advantage of this new sensor geometry is that for comparable HV requirements, there is an improvement in the scaling of the detector's electric field with both an improved drift volume and increased detector gain, as evident by the observation of surface UV laser events. The smaller anodes also do not sacrifice the gain of the detector, maintaining significant signal amplification. While the sensor shown in Figure 3.8 uses a base copper structure, to prevent sparking between the anodes and sensor's surface, a layer of diamond-like carbon (DLC) material is coated over top of the copper [78]. For the S140's ACHINOS, a 2-channel model is most commonly used (a 3-channel ACHINOS model also exists) where, in the photographed orientation, the upper five anodes (often labelled as the "north" or "near" channel) are electronically linked whereas the remaining lower six (labelled as the "south" or "far" channel) are linked. Each channel has its own unique pre-amplifier and are read out separately on the DAQ.

Signal Cross-talk

With a more complicated sensor geometry, the study of ACHINOS behaviour has been a key part of SPC characterization when it comes to S140. The most significant effect

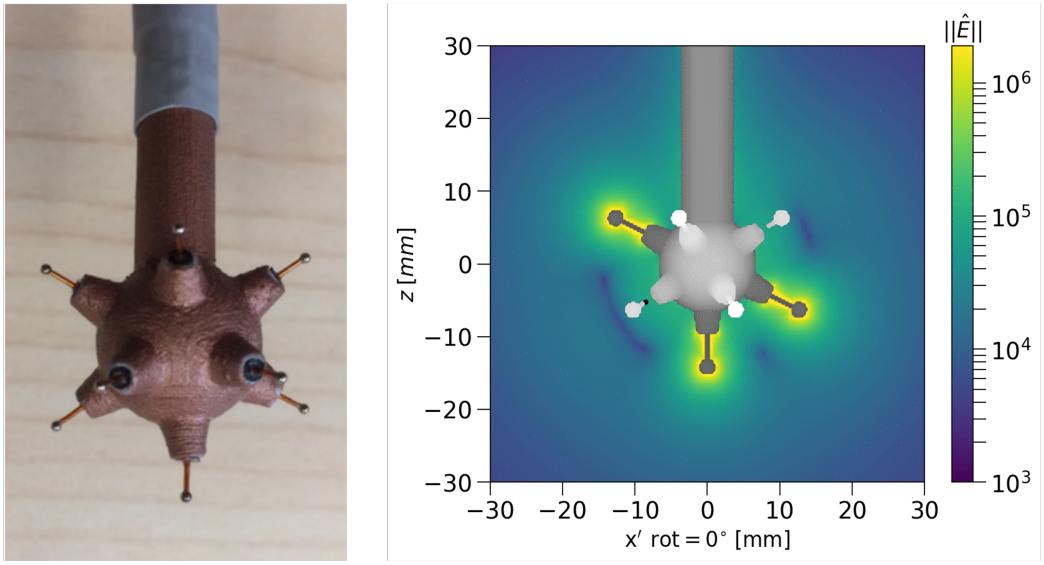

Figure 3.8: Example 11-anode ACHINOS multi-ball sensor. (Left) Model 2-channel ACHINOS used in the S140 detector (without diamond-like carbon coating). (Right) Simulated ACHINOS electric field using data from COMSOL simulations for a slice at $y = 0$ mm. Credit: D. Durnford.

that's introduced with the multi-ball readout is channel "cross-talk" (distinct from electronic cross-talk between channel cables). This cross-talk has been discovered to be a consequence of the Shockley-Ramo theorem whereby the charges produced during the Townsend avalanche process actually induce a simultaneous, opposing, current on the anodes in the neighbouring channel. We observe two signal pulses simultaneously (see Figure 3.9): one positive pulse on the primary channel and a negative secondary, smaller pulse on the opposing channel.

3.3.3 LSM Campaign with S140

While initially intended for sole operation at SNOLAB, the opportunity arose to run an initial commissioning data collection campaign with S140 over a few month period at LSM in mid-late 2019 [5]. After commissioning of S140 completed, data-taking began in September with an initial series of data runs using a 1 bar mixture of Ne + 5% CH_4 and an ACHINOS anode voltage of 1630 V. However, the more significant data collection runs came later that month when the fill gas was switched to 0.135

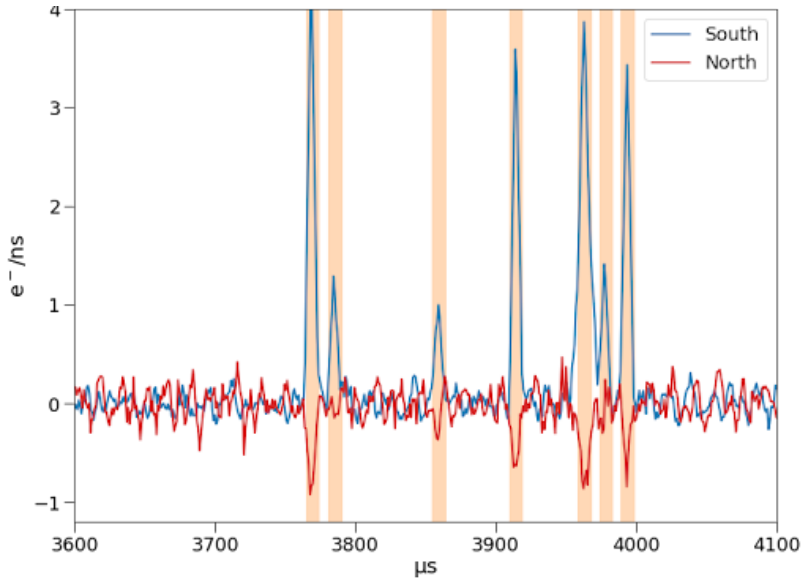

Figure 3.9: Example doubly-deconvolved event pulses displaying characteristic cross-talk pulses occurring on the north channel (in red) [5]. For this specific event, primary signal collection occurred on the south channel (in blue) with induced, negative pulses appearing on the north channel. Credit: D. Durnford.

bar of pure CH_4 and the anode potential increased to 2030 V. With a pure CH_4 target, the high concentration of hydrogen atoms allow for the search of even lower-massed WIMPs with a primary hydrogen target. Unfortunately, several factors lead to the offline decision of restricting analyses to only use south-trigger data. This includes a lack of laser calibration data on the north channel, a more isotropic south channel electric field, and generally poorer levels of noise on the north. This selection changes the fiducial volume to focus on the the south-channel-dominated region of the detector. A total of roughly ten days worth of data was recorded during this configuration and has been the main focus of NEWS-G's data analysis efforts since.

The data analysis of the LSM measurement campaign is near completion and publication as of the time of writing this thesis. As a contribution to this analysis, this thesis has dedicated Chapter 5 to the discussion of the simulation-based study of the fiducialization of S140 in its LSM configuration in an effort to characterize the fiducial volume efficiency of low-energy threshold ($\geq$2-electrons for S140 at LSM) events. Chapter 4 will focus on the MC electron drift simulation method adapted for

this specific application.

3.3.4 Future of NEWS-G

With the conclusion of the commissioning run at LSM, S140 was shipped to Canada for installation at SNOLAB in late 2019. While the detector installation has been delayed due to the COVID-19 pandemic, as of time of writing the detector has successfully been installed in the Cube Hall of SNOLAB, as photographed in Figure 3.10.

Figure 3.10: Fully assembled view of S140 as seen installed in the Cube Hall of SNOLAB during May 2022.

While the specific measurement conditions to be used during this campaign are still evolving, including over the allowable fill gases to be used on-site, a two-channel ACHINOS sensor will still be in use with the detector. Data taking is currently planned to start before the end of 2022, if not early 2023, likely using a neon and methane gas mixture to start, similarly to the LSM campaign.

As a part of this thesis, we will be taking a look at some of the instrumentation developments being undertaken at the University of Alberta with regards to S140's gas handling system at SNOLAB. In particular, the development of a live-monitoring CH_4 concentration measurement system using laser absorption spectroscopy techniques will be explored in Chapter 6 alongside S140's radon trapping system developed by P. O'Brien [66].

In addition to S140, NEWS-G is developing several new detectors including the likes of NEWS-G3 (at Queen's University), ECuME: Electroformed Cuprum Manufacturing Experiment (at SNOLAB), and DarkSPHERE (tentatively at the Boulby Underground Laboratory in the U.K.) [79]. NEWS-G3's 60 cm SPC which will be used to study CEνNS above ground at Queen's University. The other detectors are all proposed for studying low-mass WIMPs akin to S140 and SEDINE before it. These two detectors will improve upon existing techniques developed from the experience with S140 and earlier detectors. Projected SI WIMP-nucleon cross section limits (including S140 at SNOLAB) are shown in Figure 3.11 to demonstrate the predicted increase in sensitivity with advancing detector purity, technology, and analysis techniques. ECuME is a proposed underground copper electroforming facility at SNOLAB intended for constructing a new, upgraded 140 cm copper SPC with improved radio-purity relative to S140. DarkSPHERE on the other hand is a proposed copper SPC over twice the size of S140 at nominally 300 cm in diameter. This SPC is also intended to make use of advances in copper electroforming during its construction, with a tentatively planned measurement campaign to make use of a primary helium-based fill gas.

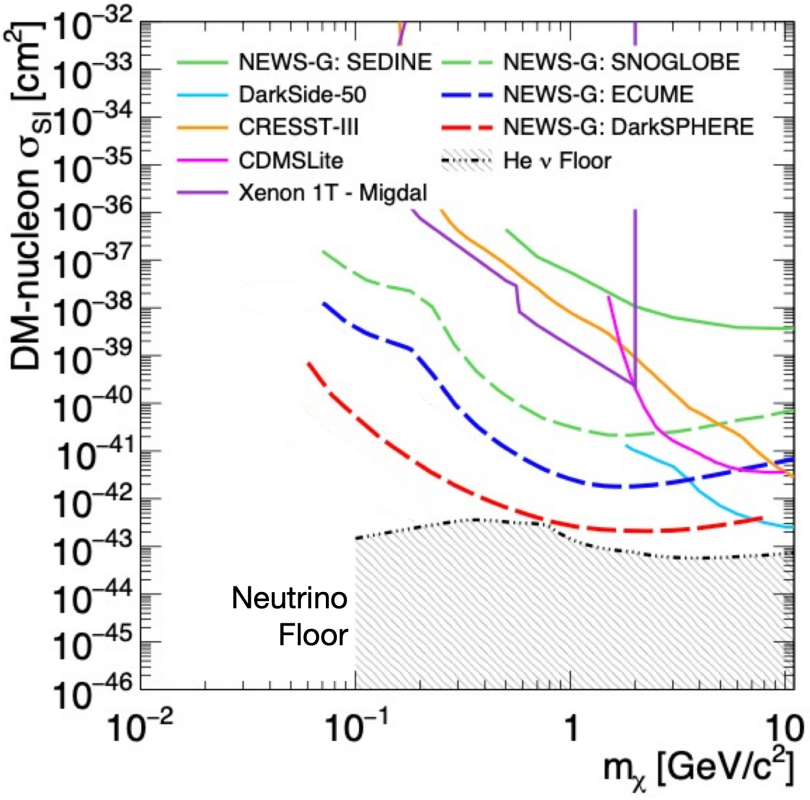

Figure 3.11: Projected SI WIMP-nucleon cross section limits for future NEWS-G measurement campaigns [79]. Highlighted are the SNOLAB campaign with S140 (green-dashed), the ECUME detector (blue-dashed), and DarkSPHERE (red-dashed).

With many new projects in the work, there is much to look forward to in the NEWS-G collaboration. In the meantime, efforts are primarily being focused towards the completion of the data analysis of S140's LSM campaign CH_4 data and the preparation for data taking at SNOLAB. The next two chapters of this thesis will walk through the study of the fiducialization of S140 during the LSM campaign from a simulation-based perspective using custom Monte Carlo electron drift simulations.

Chapter 4

MC Drift Simulations of S140

Simulations are valuable predictive tools in characterizing facets of detector behaviour. Using knowledge of a detector's physics to create and calibrate a simulation model, the capacity to study aspects of detectors not regularly attainable through typical operation is possible. In the case of NEWS-G, full detector simulations of SPCs have been in development at the University of Birmingham using a combination of GEANT4 [80, 81], a toolkit for simulating the passage of particles through matter, and Garfield++ [82], a gaseous particle detector toolkit written in ROOT [83], for finite element method analysis [84]. However, in light of the analysis work being undertaken on the LSM campaign's CH_4 data, there was a desire to use a first-principles method for studying S140's south-channel fiducialization. Since the structure of Garfield++ simulations are largely hidden behind back-end code, custom methods provide greater user control over simulations.

This chapter will describe a first-principles simulation model of S140 using a custom Monte Carlo (MC) electron drift simulation method developed at the University of Alberta. This includes the application of simulation tools like COMSOL Multi-Physics® software [64] and MAGBOLTZ [85, 86] in modelling S140's detector geometry and identifying gas-specific drift parameters. Lastly, we will take a look at the nomenclature and applications of such simulations, alongside future improvements that are currently being worked upon to bolster this novel tool's predictive accuracy.

4.1 3-D MC Electron Drift Simulation Overview

As a counterpart to existing data analyses and for use as a predictive tool, at the University of Alberta we developed in ROOT - Data Analysis Framework (a C++ based particle physics library [83]), a custom MC electron drift method that uses an electric-field model of S140 with an 11-anode ACHINOS sensor in COMSOL Multi-Physics® (typically shortened as "COMSOL") [64]. This custom method allows for the drift simulation of primary electrons, incorporating gas properties such as diffusion and electron attachment gathered from MAGBOLTZ simulation data [85, 86]. This 3-D drift simulation was originally developed by Y. Deng for studying electron drift and rise-times for varying event types in S140 [87]. In adapting the simulation infrastructure for use in studying S140's south-channel fiducialization, the drift method was expanded upon to include complete ACHINOS anode-discrimination for drifted electrons (i.e. primary electrons which have completed their drift) and additional gas properties like electron attachment.

This expanded simulation framework allows for the consecutive tracking of primary electrons, either individually or grouped as a collective event of N electrons. Thus, a typical simulation output would consist of the event-by-event count of primary electrons and their distribution about each of the eleven ACHINOS anodes including those electrons that did not successfully reach the sensor at all. Events of any sized or shape can be simulated, given valid starting coordinates within the detector. All primary electrons are drifted sequentially while coulombic interactions with any other drifting primary electrons (or secondary electron-ion pairs) are ignored (more on this in Section 4.5). Only diffusive interactions with the gaseous medium and electron attachment due to contaminants, like oxygen molecules, are taken into consideration for this method as discussed throughout Section 4.3.

4.2 COMSOL E-field Modelling

The COMSOL electric field model of S140 currently in use by the collaboration was first developed in 2019 and with the assistance of G. Savvidis and Y. Deng, has been updated to match the same geometry as the physical S140 detector and ACHINOS sensor as used at LSM (see dimension details provided in Appendix A). This includes the structural materials and applied high-voltage settings as discussed in Chapter 3 for the recording of the pure CH_4 data runs. Thus, the geometry is approximately the same (e.g., the inner diameter of the model is 0.675 m) up to any uncertainties in the recorded dimensional measurements which will be addressed in Section 4.5. There are three aspects to the COMSOL model, as illustrated in Figure 4.1.

First, a CAD model of the detector must either be provided to COMSOL or constructed directly in the software, as illustrated in Figure 4.1 (a); in our case the current model geometry was defined directly in COMSOL. This model contains the physical and material specifications of S140. COMSOL can then be used to create a surface-mapped triangular mesh of a pre-set resolution (chosen from selections such as "normal", "fine", "very fine", etc.); the "very fine" meshing used in the S140 model is illustrated in Figure 4.1 (b). It is this mesh structure which COMSOL uses to create an electric field mapping of the empty, gaseous volume using finite-element method analysis [64]. Figure 4.1 (c) shows a sampling of COMSOL-generated electric field lines calculated for both the north channel (in blue) and south channel (in red) from the surface-mapped electric potential of 2030 V on each of the eleven ACHINOS anodes and anode wires. The remaining electric field mesh which is surface-mapped to the inner surface and remaining sensory components of the S140 model is grounded akin to the real detector. The electric field is also consequently defined as 0 V/m inside the volumes of all physical structures that make up the detector. Electric field values calculated at points outside of the model are labelled as undefined ("NaN", read as: "Not a Number") and are removed prior to use in the simulation method.

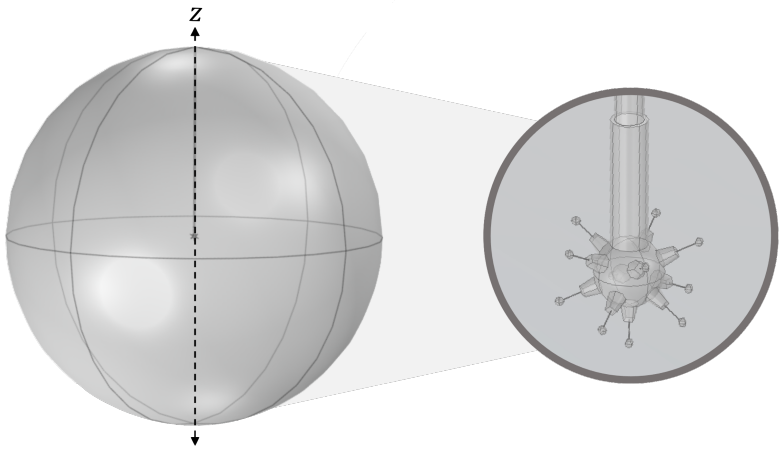

(a)

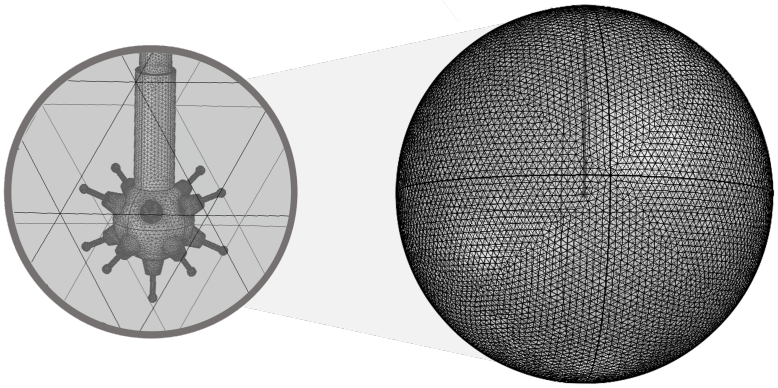

(b)

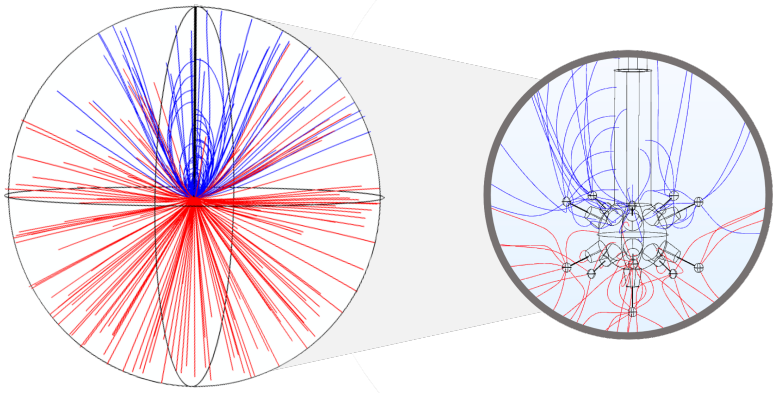

(c)

Figure 4.1: COMSOL model of S140; illustrated are (a) the S140 CAD model (with z-axis labelled), (b) a COMSOL-generated "very fine" mesh-grid, and (c) sampled north (blue) and south (red) E-field lines. COMSOL images credit: Y. Deng.

In the MC drift simulation code, the COMSOL model is exported as a finite-sized composite 3-D histogram ROOT file (called a "TH3D" object) comprised of each scalar Cartesian component of $\vec{E}$: E_x, E_y, and E_z (all exported in units of V/mm) using the rod axis as z (see Figure 4.1 (a)). This 3-D histogram object has a binning size of 100 x 100 x 100 defining a cubic region with each axis ranging between -675 mm and 675 mm, yielding a spatial resolution of 13.5 mm along each axis. As mentioned prior, points along this cube where the electric field are NaN are removed, but the dimensional resolution remains the same. To access electric field values at a given coordinate location, the value is pulled from the TH3D object with the ROOT "FindBin()" function. With this function, we get the electric field components from the bin corresponding to the position closest to the argument's positional coordinates, introducing another layer of spatial resolution limitations. To alleviate this close to the ACHINOS sensor ($r < 30$ mm) where this resolution is on the same order of magnitude as the size of the fine features of the sensory components, a secondary COMSOL file is used that has a greater spatial resolution with binning of 240 x 240 x 240. While this new file also defines a cubic region, this time ranging between -30 mm and 30 mm along each axis, we only make use of it conditionally when the current electron's radial position is less than 30 mm from the centre of the SPC. This improves the electric-field point density closest to the most common drift-terminating location of primary electrons to a spatial resolution of 0.25 mm. Combined with the drift-stepping method described next in Section 4.3, the reliable anode-wise spatial discrimination of drifted primary electrons is achievable with this model due to the sufficient spatial resolution of the COMSOL meshing and subsequent sampling of the components of $\vec{E}$. Simple linear cuts along each Cartesian axes can be used to identify the specific anode that each electron successfully drifted to.

4.3 MC Electron Drift Methodology

Once the initial coordinates for a given primary electron are defined within the detector, a series of drift steps are performed until termination due to the electric field at the electron's location being 0 V/m (this is ignoring the effect of electron attachment for the time being which may end the drift process early as detailed in Section 4.3.3). This indicates the presence of a physical structure; either the electron has reached or surpassed a point where the surface mesh was located in the original COMSOL model. The final location of the electron then determines whether or not it had successfully drifted towards one of the eleven ACHINOS anodes. During each drift step, there are two principle calculations performed: determining the change in coordinate position of the electron ($\Delta\vec{s}$, see Section 4.3.2) and the probability of attachment (P_{ATT}, see Section 4.3.3). This section will describe each calculation alongside the parameters used from MAGBOLTZ simulations to define the electron drift method.

4.3.1 MAGBOLTZ Drift Parameters

For the calculations performed during each drift step, we use parameters generated from MAGBOLTZ simulations that are fit using a cubic spline interpolation (saved as ROOT "TGraph" objects) of both mean values and 1σ uncertainties. MAGBOLTZ computes electron drift parameters via a MC method whereby an electron undergoes a number (usually $\mathcal{O}(10^7)$) of collisions with a defined gas composition at a given pressure and temperature [86]. These parameters are computed over a logarithmically spaced number of points within a defined electric field range. Five total parameters that are used during the drift calculations are taken directly from MAGBOLTZ: the drift velocity v_d (labelled as "V" in MAGBOLTZ), the transverse and longitudinal diffusion coefficients D_T and D_L (labelled as "DT" and "DL"), the electron attachment coefficient η (labelled as "ATT"), and lastly the Townsend coefficient α (labelled as "ALP"). Example raw data plots (pre-cubic-interpolation in ROOT) for these five

MAGBOLTZ parameters with 1σ uncertainties in pure CH_4 are illustrated in Figure 4.2 (see Section 5.2.1 for more information on the specific MAGBOLTZ simulations performed for these data sets). In these plots, the parameters are presented as a function of R: the subset domain of the z-axis between the bottom (i.e. "southernmost") anode and the southernmost point of the detector's inner surface. The value of E for each point in the presented MAGBOLTZ simulations is mapped to a location within the R domain corresponding to the magnitude of E as evaluated by COMSOL.

This set of plots highlights some of the key differences when varying two of the modifiable gas conditions: pressure and O_2 concentration. More details on why these two parameters are highlighted will be provided in Section 5.2.1, but it should be noted here that pressure has a notable effect on diffusion, whereas the presence of O_2 introduces non-zero electron attachment at higher radii (lower electric field strength). Another feature of interest in these plots is that η and α, when zero-valued, will fall off of the logarithmically scaled axes, and that no missing data points are presented despite what these two plots may imply (hence the presentation of both a linear and logarithmic scale).

In the drift simulation method, the cubic-spline interpolation functions for each of the five drift parameters are constructed using MAGBOLTZ data plotted as functions of electric field magnitude, E (unlike the R-domain plots used in Figure 4.2). The drift parameter values used during each step of an electron's drift are drawn from Gaussian distributions. These are constructed using the aforementioned interpolation functions, taking the mean parameter values and 1σ uncertainties as the mean and resolution of each Gaussian for the instantaneous value of E at the given electron's current location within the detector.

4.3.2 Calculation of $\Delta\vec{s}$

For the change in position, $\Delta\vec{s}$, three MAGBOLTZ parameters are pulled from their respective cubic spline interpolations given the electric field magnitude at the current

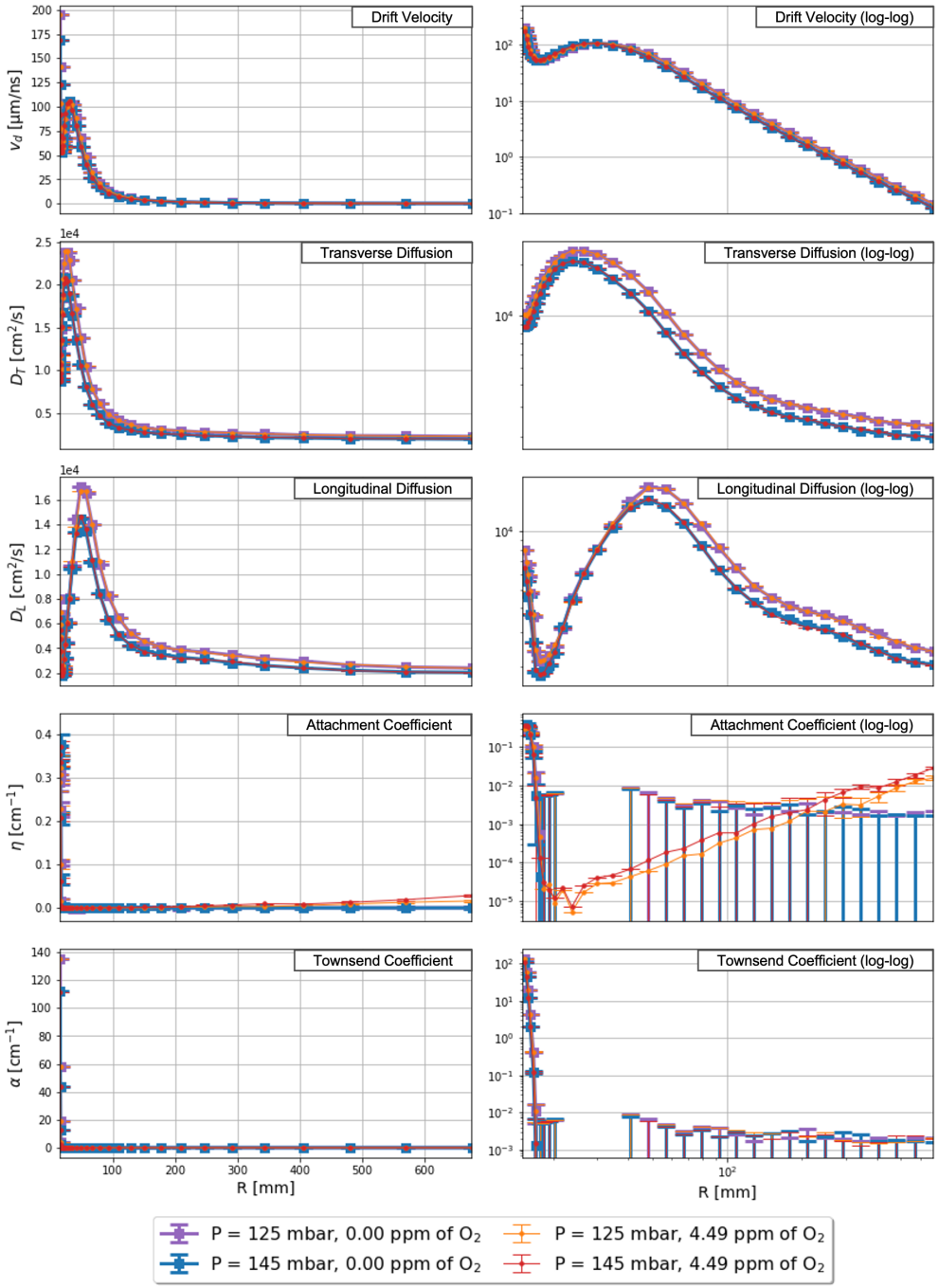

Figure 4.2: Example pure CH_4 MAGBOLTZ simulation parameter outputs presented in linear (left) and logarithmic (right) scales for different combinations of gas pressure and O_2 concentration. The E-field values are mapped to S140's z-axis (see Figure 4.1 (a)) between the bottom anode and southernmost most point of the inner-surface; this domain along z is labelled R. Choice gas settings are discussed further in Section 5.2.1. Due to zero-valued parameters, the logarithmic scale presentations of η and α have some data points located off-scale.

electron's coordinate position: v_d (in μm/ns), D_L and D_T (in cm^2/s).

For determining a given drift step, $\Delta\vec{s} = (\Delta\vec{x}, \Delta\vec{y}, \Delta\vec{z})$, a nominal scalar step size must first be determined which is labelled Δs_0. Δs_0 itself can be set to an arbitrary size but is the primary control parameter for optimizing the drift step resolution and simulation run-time. To keep large-scale ($\sim$1e5 electron statistics) simulation run-times to reasonable, sub-week long time periods, the radial detector axis (r) was divided into three domains: an inner surface region with $r > 65$ cm; a sensor region with $r < 5$ cm; and an intermediary region with 65 cm $\geq r \geq$ 5 cm. These regions modify a choice, arbitrarily-valued fundamental step size ($\Delta s_0^{'}$) such that the spatial resolution of a given drift step is greater closer to high-likelihood terminal locations such as the sensor and inner detector surface. For all simulation results shown in this thesis, a fundamental step size of 1 cm is selected. Further optimization of this step size and the stepping method presented below was deemed unnecessary for this thesis due to the current method's agreement with LSM data analyses in the ^{37}Ar calibration study presented in Chapter 5.

In the inner surface region ($r > 65$ cm), $\Delta s_0^{'}$ is scaled as $1 - r/r_{max}$, with r_{max} being a constant 67.5 cm - the inner surface radius of the COMSOL S140 model. A small limiting term is added of $0.001/r_{max}$ to prevent a zero step size when $r = r_{max}$ as follows:

$$\Delta s_0 = \Delta s_0^{'} \frac{(r_{max} + 0.001 - r)}{r_{max}}. \tag{4.1}$$

For the intermediary region (65 cm $\geq r \geq$ 5 cm), Δs_0 is not modified and by default uses the fundamental step size value ($\Delta s_0^{'} = 1$ cm). In this radial domain, it was found to be exceedingly rare (zero cases on average) for an electron to trigger a drift termination condition. In this case, a relatively larger step size does not result in a loss of accuracy in the electrons' final positions, meaning further time investment into optimizing this fundamental value was unnecessary and would likely only increase simulation run times.

Lastly, for the sensor region ($r < 5$ cm), $\Delta s_0^{'}$ is scaled as r/r_{max}. An additional

arbitrary scalar coefficient of 1/5 was applied to reduce the fundamental step size even further. As with other arbitrary values presented in this stepping method, further optimization of this parameter was not pursued due to the efficacy of the method in its current state as presented in this thesis. The full sensor region scaling is presented as:

$$\Delta s_0 = \frac{1}{5}\Delta s_0^{'}\frac{r}{r_{max}}. \tag{4.2}$$

Since $\Delta\vec{s}$ is a vector, we need to determine its scalar Cartesian components to modify the electrons' position along each axis: Δx, Δy, and Δz. To do this we must use information from the electric field (from COMSOL) and thermal fluctuations - randomized diffusive variations in position - along with Δs_0. Before introducing the primary equations used for determining the components of $\Delta\vec{s}$, diffusive steps are calculated using the three previously mentioned MAGBOLTZ parameters. We first use v_d to calculate an estimate time-step (Δt, in units of s) as:

$$\Delta t = \frac{\Delta s_0}{v_d}. \tag{4.3}$$

Thermal fluctuations in the components of $\Delta\vec{s}$ are decomposed into three directions: parallel to the direction of motion (longitudinal) and two perpendicular components (both transverse). Assuming a simple random walk diffusion model [88], each of the three independent axis of motion will experience a Gaussian spread in possible fluctuations given as:

$$\sigma_D = \sqrt{2D\Delta t}, \tag{4.4}$$

where σ_D is the resolution of the Gaussian distribution of thermal fluctuations (in cm) and D is the corresponding diffusion coefficient (in cm^2/s). For each axis of motion, a σ_D value is calculated for the given time-step and a uniquely drawn diffusion coefficient from the relevant MAGBOLTZ cubic spline. σ_{D_L} is calculated using a drawn value of D_L along the longitudinal axis. For the two transverse axes, σ_{D_T} and $\sigma_{D_{T_\perp}}$ are calculated using separately drawn D_T values. Lastly, the diffusive steps (labelled as Δd_L, Δd_T, and $\Delta d_{T_\perp}$, all in cm) are determined by a random draw from

Gaussian distributions with means of 0 cm and standard deviations of σ_{D_L}, σ_{D_T} and $\sigma_{D_{T_\perp}}$ respectively. We can finally then use the following set of equations (credited to Y. Deng) to determine the scalars: Δx, Δy, and Δz:

$$\Delta x = \Delta d_T \frac{E_z}{E}\frac{E_x}{E_{xy}} + \Delta d_{T_\perp}\frac{E_y}{E_{xy}} - (\Delta s_0 - \Delta d_L)\frac{E_x}{E}, \tag{4.5}$$

$$\Delta y = \Delta d_T \frac{E_z}{E}\frac{E_y}{E_{xy}} + \Delta d_{T_\perp}\frac{E_x}{E_{xy}} - (\Delta s_0 - \Delta d_L)\frac{E_y}{E}, \tag{4.6}$$

and lastly

$$\Delta z = -\Delta d_T \frac{E_{xy}}{E} - (\Delta s_0 - \Delta d_L)\frac{E_z}{E}, \tag{4.7}$$

where all components of E are converted to units of V/cm, with E_{xy} being the magnitude of the component of E in the x-y plane. Adding each of the above values to the electron's initial coordinates at the beginning of the step will yield the new location of the electron. This process is repeated until the electron's drift has ended according to the stopping conditions as outlined earlier in this section. Apart from thermal fluctuations, this method results in drift behaviour where the electrons generally follow the electric field lines emanating outwards from the ACHINOS anodes. Thus, the final location of the vast majority of electrons (ignoring electron attachment, this will be outlined in the following section) will indeed be at one of the eleven anodes. Simple cuts along the z-axis and in the x-y plane are used to identify which of the eleven anodes a given electron reached, labelled A_1 through A_{11}, with A_1 being the southernmost anode, A_2 - A_6 being the remaining south channel anodes, and A_7 - A_{11} being the north channel anodes.

4.3.3 Calculation of P_{ATT}

To determine the probability of a primary electron being attached (i.e. captured) by contaminant gases such as O_2 molecules, we make use of the two remaining MAGBOLTZ quantities: the attachment coefficient, η (in cm^{-1}), and the Townsend coefficient, α (in cm^{-1}). η is a measure of the probability of a drifting electron being

captured by interacting with an electron-trapping molecule. α, in this case, measures the probability of an electron creating a successful ionization interaction. For the purposes of this simulation, it is assumed that once a primary electron has undergone secondary ionization that any subsequent attachment of that electron will not effect the observation of signal.

As with previous values taken from MAGBOLTZ, the actual value for η and α are drawn from Gaussian distributions where σ is the MAGBOLTZ error of the respective parameter. Once the nominal step size, Δs_0, is calculated, the probability of attachment is immediately determined for the given step as follows:

$$P_{ATT} = e^{-(\eta-\alpha)\Delta s_0}. \tag{4.8}$$

This probability is then compared to a random value drawn between 0 and 1; if this value is less than or equal to P_{ATT} then the electron's drift is terminated early and is not considered collected by any of the anodes (recorded as a "lost" electron). By performing this step prior to the final determination of $\Delta\vec{s}$, there is a slight reduction in run time while still retaining reliability since $\Delta s \approx \Delta s_0$ even if with the effect of thermal diffusion applied.

4.4 ACHINOS Simulation Nomenclature

Within the simulation framework detailed in this section, electrons can be simulated in different groupings known as "events". The number of electrons per event and the distribution of their initial positions can vary and are normally constructed to represent real ionizing particle interactions within the detector or calibration tools (see laser calibration in Chapter 3). For the S140 fiducialization studies performed in this thesis, as presented later in Chapter 5, a concrete nomenclature is needed for labelling the anode-wise terminal positions of electrons and event categorization.

For anode identification, the north-south channel labelling for two-channel ACHINOS sensors (see Chapter 3) serves as a useful basis. Here I propose a slightly more

complex labelling system, shown in Figure 4.3, which will be used to identify the final locations of electrons for fiducialization studies.

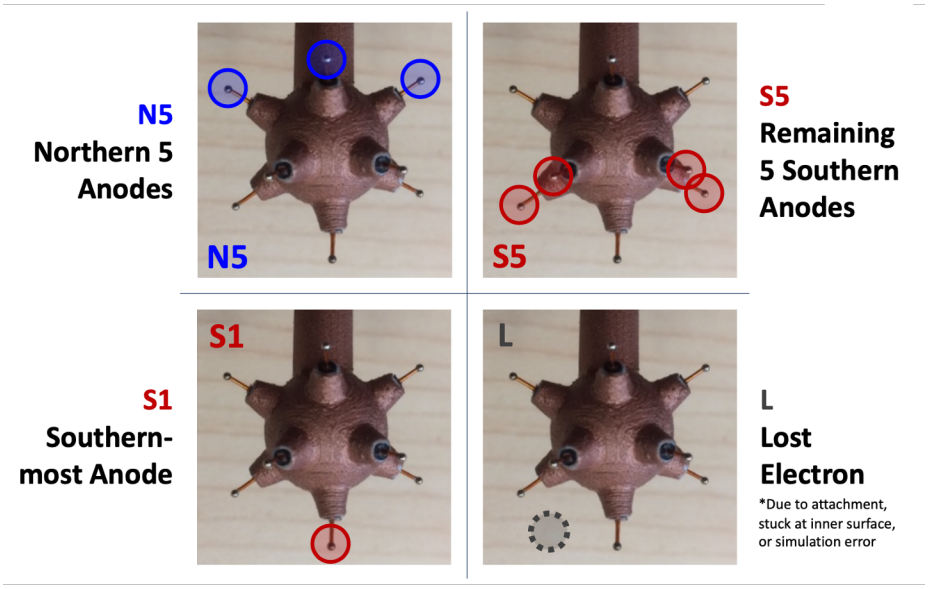

Figure 4.3: Diagram of anode labelling notation when referring to groups of anodes. Additionally, "A" is used to include all 11 anodes: "A11".

This anode notation also serves as a root identifier for "event notation". In event notation, we include a superscript that quantifies the number of electrons ascribed to the root location of interest. For example, "$S5^{(1+)}$" is a label that refers to all events where one or more electron goes to a "S5" anode (i.e., any southern anode minus the southernmost anode). These base event labels can also be combined to denote more complex event varieties. For example, we can combine the "$S5^{(1+)}$" event label with "$N5^{(1+)}$" as "$S5^{(1+)}N5^{(1+)}$". This label encompasses all events where one or more electron goes to one of the five non-southernmost anodes and one of the north anodes. This would be an example of a type of "shared" event. This nomenclature for both anode and event identification will be used for the remainder of this thesis.

4.5 Future Work

The simulation framework presented in this chapter has been primarily intended for the use in studying the fiducialization of S140 in the LSM configuration; this appli-

cation specifically will be the subject of the next chapter. Consequently, only simple a simple diffusion and electron attachment model have been implemented, but there is still work to be done in improving the simulation accuracy for applications such as drift time calculations. As shown through work performed by Y. Deng [87], this simulation method still finds slight disagreements in predicting both electron drift times and thus signal rise times (see Appendix B for more on using this framework to simulate signal rise times) when compared to existing S140 data. Proposed solutions include the study of "space-charge" effects, a consequence of primary electrons interacting with the slow-drifting secondary ions populating the detector. The implementation of these secondary interactions between the primary electrons and other ions could be the missing piece which improves the results of such studies.

The accuracy and reliability of the COMSOL model itself is still subject to further improvements. No dimensional measurement uncertainties have been taken into account when constructing the model up to this point. For future models, such as an S140 model in its SNOLAB configuration, these measurement uncertainties need to be taken into account to better assess modelling systematics. Additionally, the appropriate choice of electric field meshing needs to be evaluated to eliminate further finite-element modelling systematics. Currently, the "very-fine" mesh setting is chosen solely due to it having the highest visible mesh resolution of available COMSOL pre-sets. The corresponding electric field values need to be compared alongside other mesh options to assess any possible disagreements and the level of convergence between models. For the remainder of this work, and as discussed in Chapter 5, I will ignore the COMSOL model as a possible systematic, assuming that the calculated electric field and exported TH3D data points are static variables. Evaluated systematics will be solely targeted around the drift parameters, as generated via MAGBOLTZ simulations.

Further optimization of both the drift stepping method and COMSOL model will continue to be studied in further applications of this drift simulation framework.

Chapter 5

Study of the Fiducialization of S140 at LSM via Simulation

A crucial component in the determination of exposure limits for WIMP-nucleon cross sections, as discussed in Chapter 2, is the mass exposure of a given detector to WIMP interactions. In the data analysis for NEWS-G's LSM campaign, which has been refined to south-channel triggered data with a 2-channel ACHINOS, the method that we use to characterize the target mass of pure CH_4 is the study of S140's fiducialization (i.e. the characterization of the detector volume where a signal is observable). Specifically, we are most interested in this detector property for select minimum energy events (e.g., 2-electron events) where the effective mass exposure of the south-channel to these select events contributes towards S140's low-mass WIMP sensitivity and discovery potential.

In this chapter, I focus on the use of MC drift simulations in characterizing S140's south-channel fiducial volume with a 2-channel ACHINOS and pure CH_4 fill gas. I will discuss the application of the simulation methodology described in Chapter 4 for studying fiducialization and simulation calibration using ^{37}Ar events. I will also present low-energy fiducialization results for S140 alongside fiducialization efficiencies that will be used in the upcoming publication of the LSM data analysis results. Future applications of these simulations will also be discussed for upcoming NEWS-G projects, specifically the study of a possible SPC directionality channel.

5.1 ^{37}Ar Calibration Methodology

To determine the efficacy of the MC electron drift simulations in studying S140's fiducialization, first, the simulation must be verified through calibration with known LSM data. As described in Chapter 3, one of the principle calibration sources used with S140 is ^{37}Ar – a diffuse gaseous radioactive source with a prominent ∼2.8 keV decay observable with SPCs. In the pure CH_4 data recorded at LSM, analyses have been performed looking specifically at such ^{37}Ar data. This section will take a look at the technique for how we can use this existing data analysis to perform the calibration of the simulation described in Chapter 4.

5.1.1 ^{37}Ar Simulation Basics

The challenge with the 2-channel ACHINOS sensor used in S140 at LSM is that observable events may display signal dissociated about both electronic channels. In other words, primary electrons for a multi-ionization event may drift towards multiple anodes that span both channels resulting in (non-cross-talk related) signal appearing on both channel readouts simultaneously. Therefore, individual ^{37}Ar events (in fact, all multi-ionization events) are characterized based upon the channel-wise distribution of observed signal as either being "north", "south", or "shared". Normally, from a simulation standpoint, we can be more pedantic and define these groups by the ratio of primary electrons which arrive at each channel as illustrated in Figure 5.1.

While this simulation-based method can be a powerful tool in characterizing the fiducialization for various types of events, this way of categorizing is not directly comparable to data analyses since individual primary electrons cannot be identified. Instead, we look at the observable signal asymmetry of each event:

$$Asymmetry = \frac{A_S - A_N}{A_S + A_N}, \tag{5.1}$$

where A_N is the north channel's signal amplitude (in ADU) for a given event and A_S is the south channel signal amplitude (in ADU). Cuts placed upon this coordinate

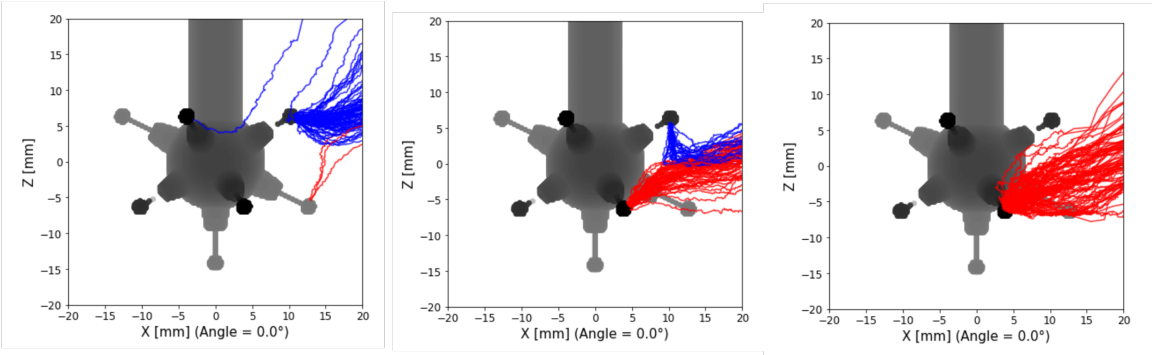

Figure 5.1: Examples of "north" (left), "shared" (centre), and "south" (right) ^{37}Ar simulated events. Trace colours identify the channel that each individual primary electron was collected by: blue for north and red for south. Exact north-south event thresholds are determined via event asymmetry for calibration purposes; events with sufficiently few electrons in the non-dominant channel may still be considered non-shared in these analyses as demonstrated here for the "north" (left).

transformation quantity is how each of the three event categories is defined for ^{37}Ar calibration data. An example of this is presented in Figure 5.2 (a) which shows CH_4 LSM ^{37}Ar data pulse amplitudes for events triggered on either channel. Here the north channel signal amplitude per event is plotted against the respective south channel signal amplitude. In Figure 5.2 (b), the asymmetry transformation is applied to more clearly distinguish between the north and south dominated populations. The total combined signal amplitude of each channel is plotted against the asymmetry of each event.

By applying cuts to these asymmetry values, we define "north", "shared", and "south" events. An asymmetry cut where shared events fall within the domain [-0.75, 0.75] is illustrated in Figure 5.2 (b) [89]. Visually, this divides the detector into two channel-dominated regions with an interference region where "shared" dominate. These regions are presented in Figure 5.3 where on the left events which have failed the asymmetry cut (i.e. are "pure" north or south events) are presented as a colour-scaled function of fraction of south-channel primary electrons (see Section 5.1.2 for how this is determined). On the right are those "shared" events which passed the asymmetry cut.

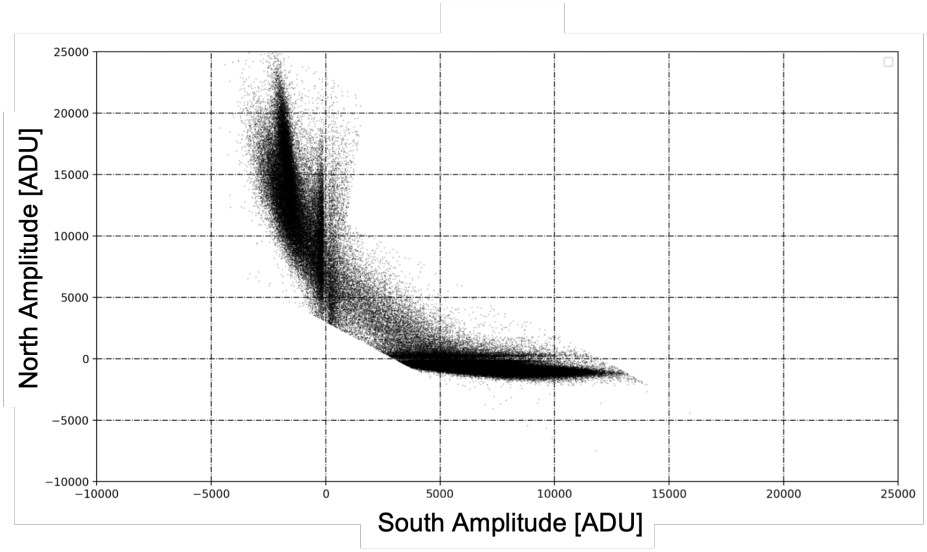

(a)

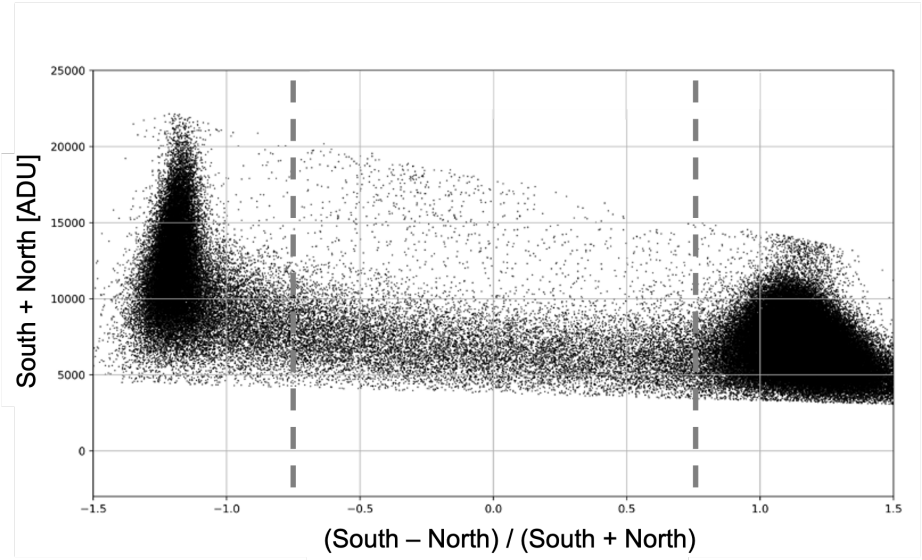

(b)

Figure 5.2: Sample LSM ^{37}Ar data for 135 mbar of pure CH_4 using data triggered on both channels [89]. (a) Treated north channel pulse amplitudes verses their respective treated south channel pulse amplitudes. (b) Applied asymmetry transformation following Equation 5.1 highlighting a clearer definition in north dominated and south dominated events. Standard asymmetry cut of [-0.75, 0.75] is highlighted by vertical dashed grey lines with north events at lower asymmetries and vice versa. Credit: G. Savvidis.

With this choice of cut, current LSM analyses of ^{37}Ar data find that (22.73 ± 0.65)% of events are "pure" north, (68.38 ± 0.70)% are "pure" south, and (8.88 ±

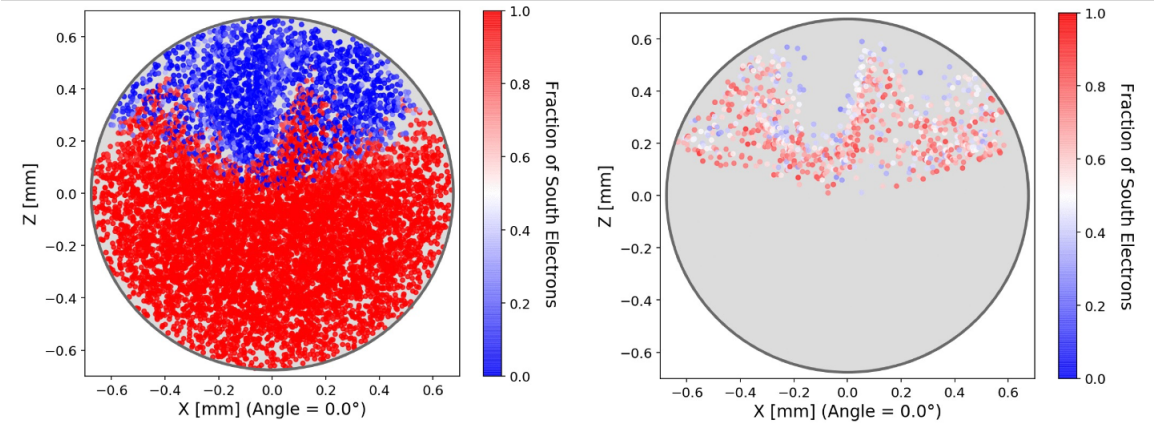

Figure 5.3: (Left) 3-D simulated view of ^{37}Ar events (out of 10,000 simulated events) excluded by the [-0.75, 0.75] asymmetry cut. (Right) The same 3-D simulated view illustrating ^{37}Ar which pass the asymmetry cut and are "shared". Plotted as a function of fraction of south-channel primary electrons, events that appear more red are south dominated where as those that appear more blue are north dominated.

0.40)% are shared [90]. This provides a calibration point for simulations of ^{37}Ar events. This process involves the complete emulation of such analyses, including replicating signal amplitudes as explored in Section 5.1.2. The remainder of this section will look at how we approximate this asymmetry result to validate the geometric results obtained from the base simulation method in determining the terminal locations of primary electrons.

In order to simulate an ^{37}Ar event, we consecutively drift a random number of corresponding primary electrons according to the prescribed electronic drift method in Chapter 4. The random number of primary electrons simulated per event is defined by a Poisson probability distribution. Poisson is favoured over the COM-Poisson distribution due to its simplicity in implementation; the slight narrowing of the probability distribution's resolution due to the Fano factor will minimally affect simulation calibration results. Using results from existing LSM data analyses performed by D. Durnford [91], the mean number of electrons per ^{37}Ar event is determined using the W-value parametrization presented in Equation 3.2 where $U = 15.70^{+0.52}_{-0.34}$ eV and $W_0 = 30.0^{+0.14}_{-0.15}$ eV. Since the mean energy of a single ^{37}Ar event, 2.82 keV $>> U$, we

assume that $W_{er} \approx W_0$. In determining a given simulated event's number of electrons we divide 2.82 keV by a value of W_0 drawn from the following log-likelihood function as defined by R. Barlow for approximating asymmetric uncertainties [92]:

$$\ln L(\hat{x}; x) = -\frac{1}{2}\frac{(\hat{x} - x)^2}{V + V'(x - \hat{x})} \tag{5.2}$$

where $V = \sigma_-\sigma_+$ and $V' = \sigma_+ - \sigma_-$. In this function, x represents a variable with asymmetric uncertainties (σ_+ and σ_-) with $\hat{x}$ being its central value. In the case of W_0, a log-likelihood function, $\ln L(\hat{W_0}; W_0)$, can be constructed for the purpose of generating random values of W_0, effectively propagating its uncertainty into the determination of a given simulated ^{37}Ar event's number of primary electrons.

The starting coordinates, (x_i, y_i, z_i), for a given event are randomly selected within the gaseous volume of the detector and applied to all drawn electrons corresponding to that event, making the assumption that each ^{37}Ar event is purely point-like. Each primary electron in the simulation has one of three outcomes: either they reach a north or south ACHINOS anode or they are lost through electron attachment, existing in a non-drift region close to the detector's inner surface, or rare simulation error. A typical ^{37}Ar simulation result may look something like the distribution shown in Figure 5.4.

5.1.2 Signal Amplitude Construction

The MC drift simulations are only capable of providing information on the geometric distribution of events via counts of the final anode and non-anode positions of primary electrons. Consequently, to determine an event's asymmetry, a signal amplitude must be associated with each simulated primary electron that successfully reaches any of the eleven anodes.

Pre-existing information from other LSM-related data analyses can be used to do this. The main points of consideration are the values of gain associated with each anode determining the base signal amplification response via the Polya distribution

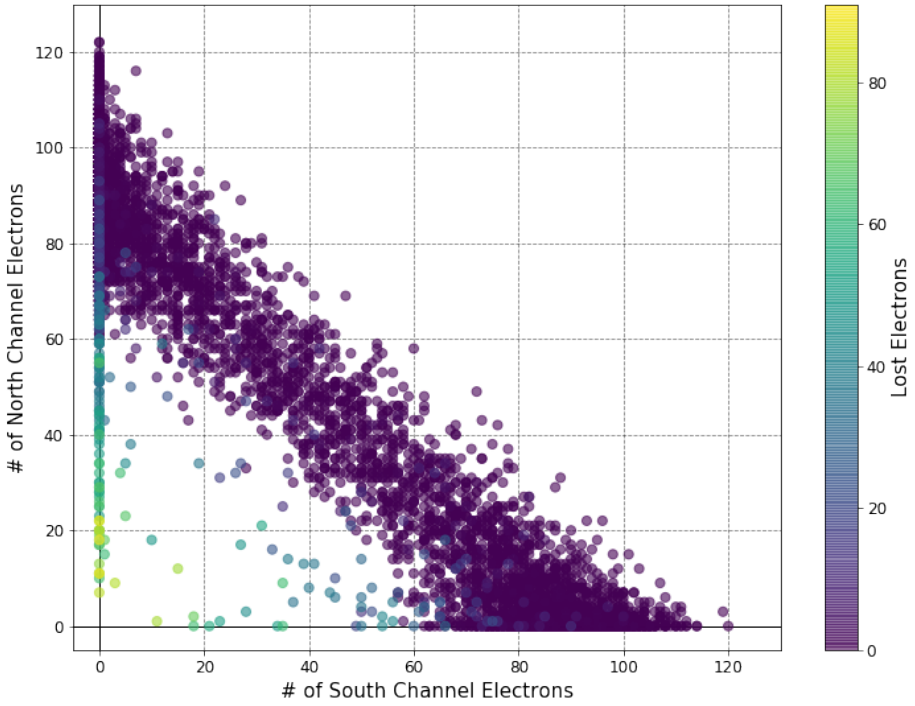

Figure 5.4: An example raw ^{37}Ar simulation output of the number of primary electrons which reached a north channel anode versus the number that reached a south channel anode for 10,000 uniformally distributed events in 125 mbar of pure CH_4. The colour-scale indicates the number of "lost" electrons which did not successfully reach any of the eleven anodes.

(Equation 3.5), channel cross-talk, and the baseline noise of each channel. Additional correction factors can be applied to account for systematic uncertainties likely due to unknowns in electric potential variation between anodes or signal gains, but will not change the underlying geometric component to the simulation results. Throughout this section, Figure 5.5 will be used for visual reference to illustrate these steps.

(1) Anode Gains

In the study of the ACHINOS gain at LSM, the characterization of the individual gains on the six south-channel anodes via analysis of south-trigger ^{37}Ar data was performed. This analysis made use of a new electron-capture cascade decay model for ^{37}Ar [93], new to the LSM data analysis, to study ^{37}Ar data energies and ascribe each south-channel anode a best-fit value of gain with uncertainty [91]. These values

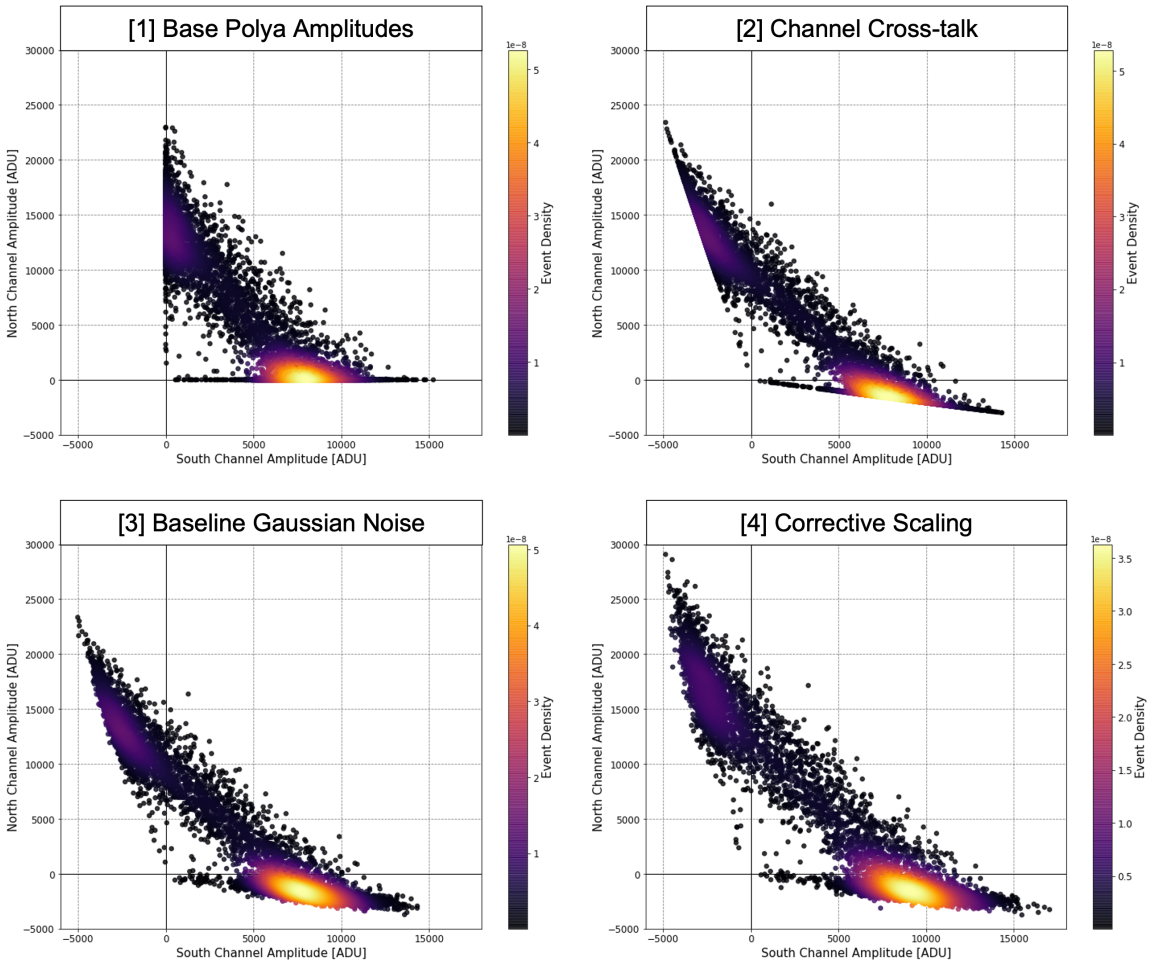

Figure 5.5: Steps for event signal construction for 10,000 uniformly distributed ^{37}Ar events in 125 mbar of pure CH_4. Steps include: (1) generation of base signal amplitudes from Polya distributions (Equation 3.5); (2) applying channel cross-talk; (3) Gaussian baseline noise smearing; and (4) corrective signal amplitude and resolution scaling. The colour scale indicates "event density" using a Gaussian kernel density estimation to highlight denser populations of events.

describe a 6-D Gaussian structure with mean anode gains, $\langle G_S \rangle$, given by the matrix:

$$\langle G_S \rangle = \begin{pmatrix} 69.915 & 88.172 & 88.619 & 88.674 & 106.871 & 106.877 \end{pmatrix}. \tag{5.3}$$

The uncertainties of said 6-D Gaussian are presented by the following covariance matrix:

$$\langle G_S \rangle_{cov} = \begin{pmatrix} 0.011781 & 0.0219668 & 0.0167971 & 0.009227 & 0.0205775 & 0.0212301 \\ 0.0219668 & 0.0638725 & 0.0410983 & -0.00711555 & 0.0475056 & 0.05199 \\ 0.0167971 & 0.0410983 & 0.0663086 & -0.0377682 & 0.0310707 & 0.0366512 \\ 0.009227 & -0.00711555 & -0.0377682 & 0.0798538 & 0.0106861 & 0.00502408 \\ 0.0205775 & 0.0475056 & 0.0310707 & 0.0106861 & 0.0423165 & 0.00435906 \\ 0.0212301 & 0.05199 & 0.0366512 & 0.00502408 & 0.0435906 & 0.0494383 \end{pmatrix}. \tag{5.4}$$

Using these two sets of values to define our 6-D Gaussian, for a given ^{37}Ar simula-

tion, a unique set of six anode gains defining $\langle G_1 \rangle$ through $\langle G_6 \rangle$ (corresponding to anodes A_1 through A_6 respectively) are drawn at random such that the six anode gains approximately match Equation 5.3 to within uncertainty. Each anode is assigned a respective value of gain in increasing order such that $\langle G_1 \rangle$, the gain of the southernmost anode, is the smallest. Therefore, on average the total south channel gain is approximately 91.521 (taken to 5 significant figures).

Unfortunately, without a comparable gain analysis for the north-channel due to a lack of north-trigger data analysis in the LSM campaign, we use the ratio between the average channel gains to approximate the five north anode gains instead. Any corrections that may need to be performed as a consequence of this approximation will be addressed in step (4). The average gain on each channel as used in this thesis was taken as a part of the identical analysis study which determined the LSM data asymmetry cuts presented in Section 5.1.1 [90]. Even though this is a different analysis than described earlier, the ratio of average gain between channels for the same data set should be approximately the same. Using the asymmetry cuts to identify "pure" north and south ^{37}Ar events, the average signal amplitude on each channel was recorded as 12,127.31 ADU for the north and 7,108.06 ADU for the south. Since both values are proportional to the average signal gain on each channel, we can use their ratio of 1.70614. Therefore, for the five north anode gain values ($\langle G_7 \rangle$ through $\langle G_{11} \rangle$), we use the same values as with the southern anodes excluding the southernmost anode, A_1 (which has no symmetric north channel anode), but scaled by this ratio of channel gains.

Also from the LSM analyses performed by D. Durnford is the Polya shaping parameter, $\theta = 0.125^{+0.026}_{-0.023}$, that is used in each Polya distribution [91]. To propagate the uncertainty in θ, I again make use of the Barlow approximation for asymmetric uncertainties to construct a log-likelihood function using Equation 5.2. With this function, a single random value of θ may be generated for use in each of the eleven anode's respective Polya distributions.

Using these eleven gain values associated with each anode and θ, each electron in the given ^{37}Ar simulation is then associated with a fundamental signal amplitude using the unique Polya distribution (see Equation 3.5) corresponding to its respective anode. The sum of the signal amplitudes yields the first stage in the north-channel versus south-channel signal amplitude plot in Figure 5.5 (1).

(2) Channel Cross-talk

To replicate the observable cross-talk in the north and south channel signals due to Shockley-Ramo effects (see Section 3.3.2) [63], the following set of equations was used on the base signal amplitudes of the north and south channels from step (1):

$$N_{signal} = N5 - X_{S1}S1 - X_{S5}S5, \tag{5.5}$$

$$S_{signal} = S1 + S5 - X_{N5}N5. \tag{5.6}$$

Here we distinguish between the southernmost anode and the other five southern anodes using S1 and S5 notation for the base signal amplitudes (see Section 4.4), with the base signal for the north channel labelled as N5. X_{S5}, X_{S1}, and X_{N5} represent cross-talk factors between each channel.

The reason that we distinguish between S1 and S5 in the study of cross-talk is that through characterization of the ACHINOS sensor used during the LSM campaign, it was found that the level of cross-talk induced onto the north-channel is slightly different. At Queen's University, using the stainless steel S30 SPC, ^{241}Am and ^{55}Fe sources were placed at the southernmost point of the detector where primary signal would solely be observable on S1 (i.e. A_1). In comparison to diffuse ^{37}Ar, the cross-talk signal was slightly larger for these localized sources. The cross-talk factors X_{S5} and X_{N5} were found to be both equal to 0.21 with X_{S1} being 0.20 [94]. With these cross-talk values applied, the observable signal change can be seen in step (2) of Figure 5.5.

Gaussian Baseline Noise

Both the north and south-channel signals observe a baseline offset and Gaussian noise which smears the base signal amplitudes. This is simple enough to add to the existing signal amplitudes by creating two unique Gaussian distributions, one for each channel. In the referenced study of LSM data asymmetry, the baseline noise levels of each channel, including mean noise and resolution, were estimated to 2 decimal places [90]. Using those results, we set the north-channel Gaussian to a mean (signal offset) of -29.91 ADU and resolution (σ) of 322.19 ADU. The south-channel Gaussian is set to have a mean of -51.60 ADU and resolution of 182.85 ADU.

For each event in the simulation, a noise value is pulled from each of these two Gaussians and then added to the existing signal amplitudes. The resulting change to the north and south-channel signal distribution is, in effect, the result of convolving each with their respective baseline noise Gaussian distributions. The effect of this step is illustrated in Figure 5.5 step (3).

(4) Corrective Scaling of Mean Signal Amplitudes and Resolution

With solely the three previously described signal construction steps applied, regardless of simulation systematics, it is typically the case that there is a discrepancy between the north and south population distributions and what is observed in treated data [90]. Specifically, at this stage, if we look at only events which pass our asymmetry cut (i.e., remove those with an asymmetry [-0.75, 0.75]), we observe a clear difference in two metrics of the "pure" distributions: the mean signal amplitudes (μ) and their resolutions (σ). The simulated data (within systematic uncertainty) using steps (1) through (3) is found to always underestimate the resolution of these two populations, but only sometimes underestimating the mean signal amplitudes in high electron attachment scenarios.

What this discrepancy suggests is one, or a combination, of possibilities: the fundamental MC drift simulation has inherent inaccuracies or unaccounted-for systematics,

and or the first-principles steps used to create the signal amplitudes are inaccurate, and or the assumptions made (e.g., the north anode values of gain) are incorrect.

Despite this disagreement in distributions, what we find is that the calibration asymmetry results produced using this simulation method are still in agreement with LSM data both with and without this corrective scaling step (see section 5.2.3). Since the purpose of the calibration is solely to demonstrate the validity of the MC drift simulation via this very comparison, applying a corrective step in the signal creation process seemed appropriate. This would test the rigidity of the method by accounting for possible unknowns or systematics missed during this process and illustrating their effect on the resulting asymmetry.

The exact method for correcting our two metrics is somewhat arbitrary and thus an ad hoc Gaussian convolution method was chosen following some experimenting with linear scaling. In this method, we use information from the unscaled "pure" north and south distributions (see Figure 5.5 (3)) to construct both convolution Gaussian distributions as shown in Figure 5.6.

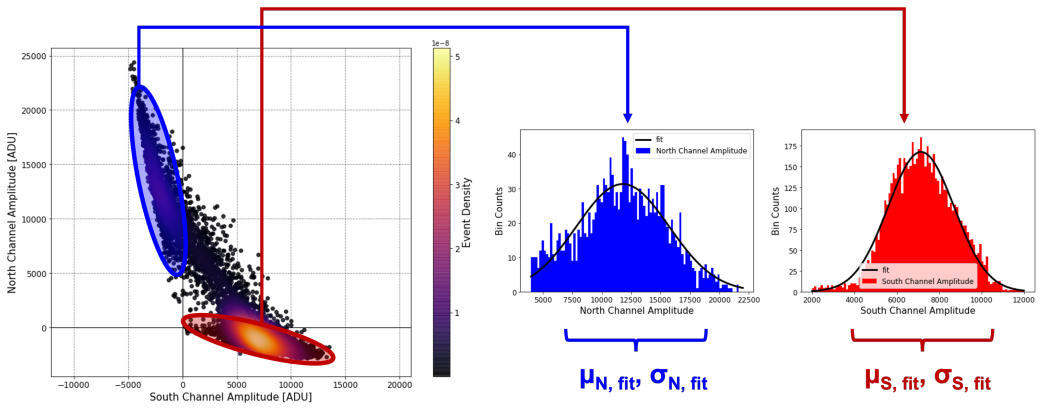

Figure 5.6: Example selection of 10,000 simulated events using an asymmetry cut of [-0.75, 0.75] to identify "pure" north and south populations. The remaining distributions are fit to Gaussian distributions where the mean signal amplitudes ($\mu_{N,fit}$ and $\mu_{S,fit}$) and resolutions ($\sigma_{N,fit}$ and $\sigma_{S,fit}$) are used in constructing convolution Gaussians for the north and south channels.

These convolution Gaussians have two properties, with the first being that their means

are the difference between data μ_{data} and the simulated distribution μ_{fit}:

$$\mu_{conv} = \mu_{data} - \mu_{fit}. \tag{5.7}$$

The second property is that resolution must follow:

$$\sigma_{conv} = \sqrt{\sigma^2_{data} - \sigma^2_{fit}}. \tag{5.8}$$

In principle, the effect of these Gaussians when convolved with their respective simulated distributions is that they should yield a Gaussian distribution approximately the same as observed in the data in terms of μ_{data} and σ_{data}.

The one drawback of this method is that every event will be smeared by the same Gaussian, which means that the degree to which a given signal amplitude can change is not correlated with the number of electrons per channel per event, resulting in significant over-corrections for few-electron events. Therefore, an additional linear scaling factor is applied to the convolution amplitude added to each event in both the north and south which we define as: $N_e/\langle N_e \rangle$. Here N_e is the number of electrons in the specific channel for the respective event and $\langle N_e \rangle$ is the average number of electrons per event in the channel. This scales the possible convolution value by the number of electrons in the given event normalized to the mean number of electrons per event in the channel.

In practice, what this method looks like is very similar to the Gaussian baseline noise step whereby for each event a random scaled value is drawn for the north and south convolution Gaussians and added to their respective signal amplitudes. An example of how this step looks in is given in Figure 5.5 step (4). For more discussion on how this scaling method affects the asymmetry results please see Section 5.2.3.

5.1.3 Asymmetry Coordinate Transformation

With the base signal creation process complete, the asymmetry transformation (see Equation 5.1) can be applied. When performed on the step (4) plot in Figure 5.5, we

observe the following asymmetry distribution by plotting the total signal amplitude versus asymmetry akin to Figure 5.2 (b), as presented in the example distribution in Figure 5.7.

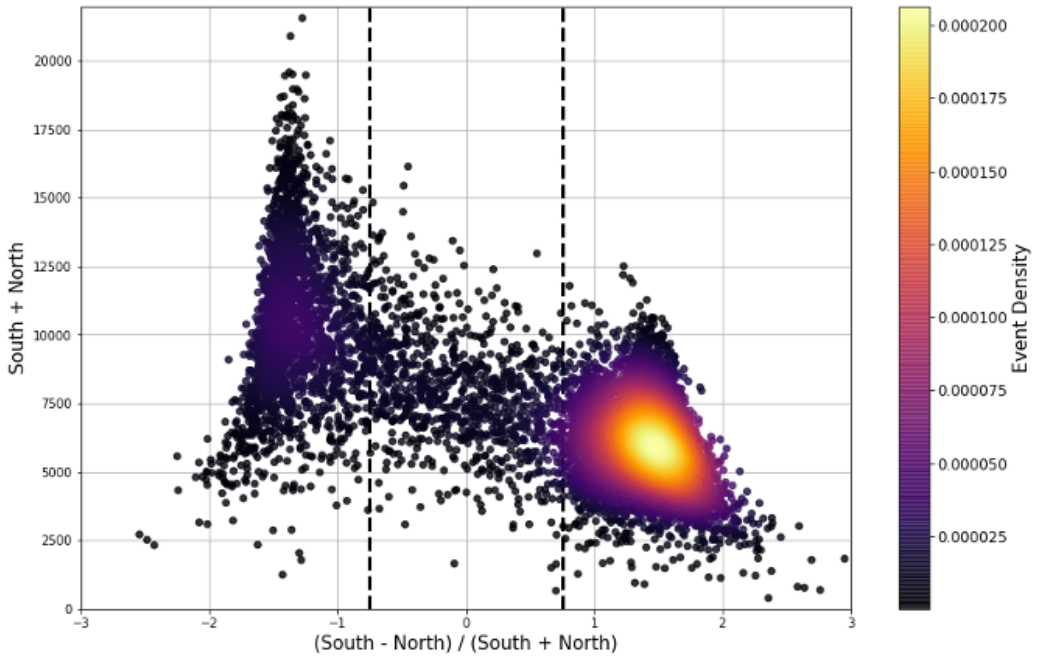

Figure 5.7: Example distribution of event asymmetry with highlighted cuts at asymmetries of -0.75 and 0.75.

This concludes the process for how we can compare simulated fiducialization results to LSM data. The following section will discuss the specific simulations that were performed, what systematics were considered, and the statistical evaluation of the ratio of north, south, and shared events for ^{37}Ar events, followed by the final ^{37}Ar calibration results.

5.2 ^{37}Ar Simulation Calibration Results

With a recipe in place for assessing simulated event asymmetry, the final piece in determining simulated ^{37}Ar calibration results is the characterization of uncertainties. This includes possible systematics (see Section 5.2.1) as well as statistical fluctuations (see Section 5.2.2) in the final calculated asymmetry ratios.

5.2.1 Evaluation of Systematics

There are two levels to possible systematics which may affect simulated ^{37}Ar results. Firstly, there are systematics regarding the fundamental MC drift simulations and secondly, there are systematics regarding the creation of signal amplitudes. Since the ultimate goal of this simulation-based work is to use the geometric distribution of electrons to characterize the fiducialization of low-energy events in the S140 detector, our main focus is on characterizing systematics on the simulation side, rather than while creating signal amplitudes that can be corrected for later (see step (4) of the previous section).

With our simulation framework, there are certain aspects that we assume are static whereas possible systematics can be evaluated around these fixed structures. These include the fundamental MC drift method, including arbitrary aspects such as the choice of step sizes, and the physical structure of S140 as modelled in COMSOL (Figure 4.1). This leaves the parameters derived from MAGBOLTZ simulation files and the COMSOL electric field data as possible sources of systematics. Regarding the latter, assuming that the model is fixed and accurate, the electric potential mapping on each of the eleven anodes is what principally determines the electric field. Nominally the high-voltage is set to 2030 V, identical to the high-voltage power supply used at LSM. However, the high voltage supply that was used with S140 at LSM is assumed to have negligible uncertainty (< 0.5 V precision) and thus it stands to reason that treating this as a significant systematic is unnecessary for this calibration. As also discussed in Chapter 4, there are elements to the physical dimensions and mesh structure of the COMSOL model which may impose additional systematics which will need to be further assessed in future iterations of this work. For now, I am assuming that the model is accurate and a static part of the simulation with possible systematics defined around this fixed element of the simulation methodology.

MAGBOLTZ comparatively is more complicated since several parameters can be

modified for a given simulation to change the five usable output variables (recall V, DT, DL, ATT, and ALP from Chapter 4). We can divide these into two categories: physical parameters and simulation parameters. We will assume that the MAGBOLTZ "simulation" parameters are also fixed; these include the specified electric field range, number of computed data points, and number of electron collisions simulated [85]. Physical parameters include gas pressure and temperature as well as the concentrations of contaminant gases such as water vapour and oxygen.

From this list, the two most prominent systematics identified were MAGBOLTZ gas pressure and oxygen concentration. The gas temperature was ignored due to its correlation with varying gas pressure. Water vapour was found to have at most a slight reduction effect in observed changes to the five MAGBOLTZ outputs when coupled with oxygen, but solely did not significantly affect these parameters and thus was deemed negligible for this study.

The choice of systematic range for both parameters was determined through observational uncertainties in the recording of data at LSM. Nominally at 135 mbar of pure CH_4, the analog pressure gauge that was used to record the pressure of S140 had a graduation spacing of 10 mbar. Thus, a systematic range of [125 mbar, 145 mbar] was selected for this study.

Oxygen Concentration Systematic

Evaluating the systematic of oxygen concentration proved to be a more complicated prospect because the calibration of oxygen within an SPC is a study that has yet to be performed by the NEWS-G collaboration. Oxygen is a common contaminant gas whose presence results in the previously mentioned effect called "electron attachment". Due to their high electro-negativity, O_2 molecules are effective at trapping drifting primary electrons which prevents them from forming an observable signal. In multi-electron events, this results in an observable energy loss correlated with the initial radial position, and thus the rise-time of the point-like event. To illustrate this

effect, sample pure south-trigger CH_4 data from the LSM campaign shown in Figure 5.8 demonstrates how electron attachment can effectively lower the observed signal energy for ^{37}Ar ($\sim$2.8 keV) events with increasing rise times.

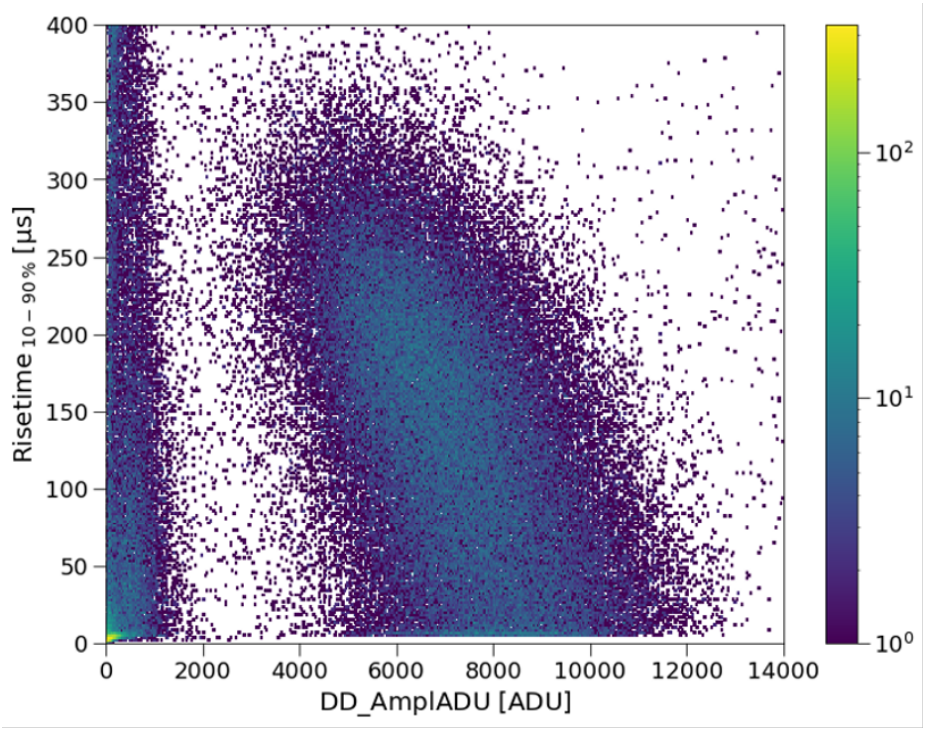

Figure 5.8: Sample south-trigger ^{37}Ar data recorded at LSM in 135 mbar of pure CH_4 illustrating electron attachment with a loss in energy ("DD_AmplADU") as a function of 10%-90% signal rise time. Such results indicate the presence of some unknown contaminant concentration of O_2. Credit: D. Durnford.

Given the lack of an O_2 concentration calibration for SPCs, a precise measurement of the concentration of O_2 present in the detector is unavailable from LSM data. However, as explored in Chapter 4, electron attachment is something that can be simulated in the MC drift simulation framework through the probabilistic removal of primary electrons using the attachment and Townsend coefficients (η and α). Therefore, via MC drift simulation, we can compare the effect of electron attachment on simulated data to that observed in the LSM data to set reasonable systematic estimates on the MAGBOLTZ concentration of O_2.

For this study, I performed simulations of uniformly distributed sets of 10,000 ^{37}Ar

events using varying MAGBOLTZ simulation data files. For each event, a 10%-90% rise-time value was calculated using the method described in Appendix B. Sample simulation results for two different concentrations of O_2 (0.00 ppm and a selected test case at 3.25 ppm) and at the two identified systematic pressures are provided in Figure 5.9 to visually demonstrate these simulation results.

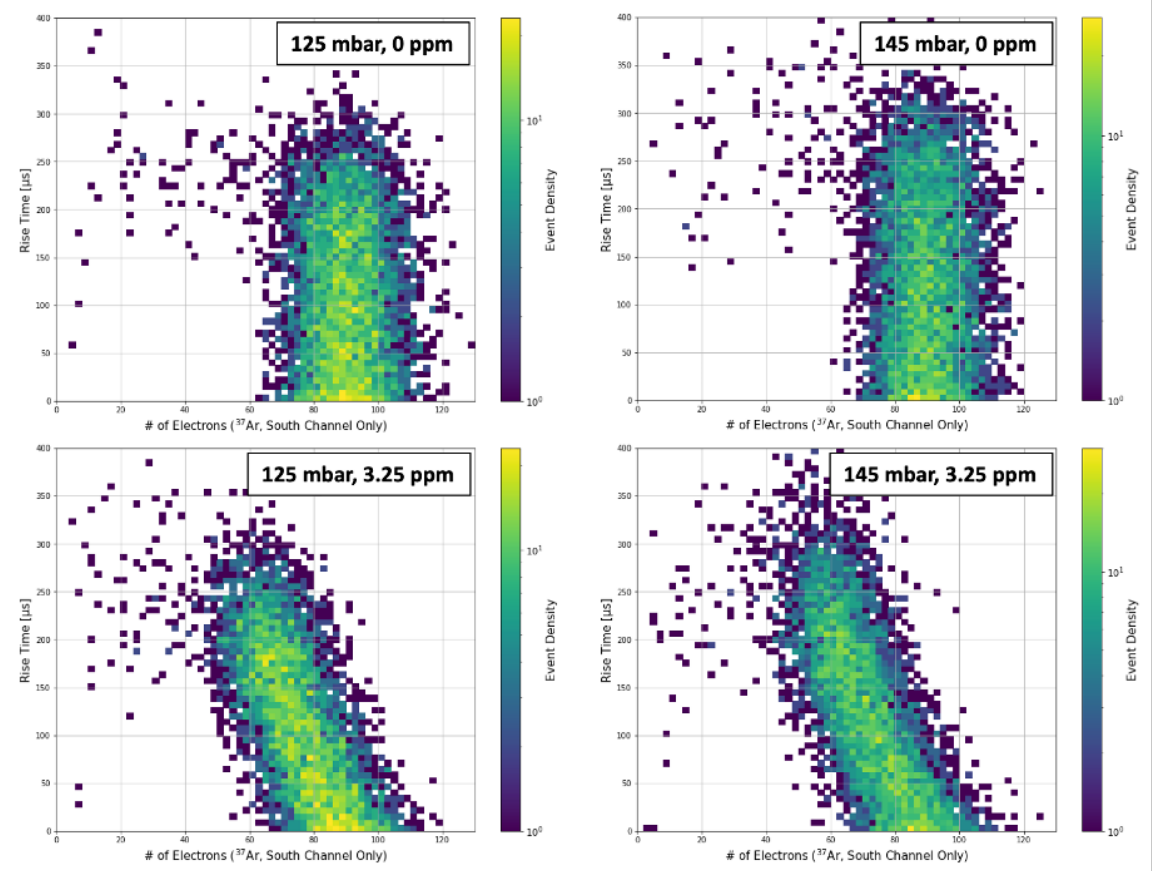

Figure 5.9: Example 10%-90% rise times vs. counts of electrons (linearly proportional to signal amplitude) illustrating the effect of increasing electron attachment for two different selected concentrations of O_2 (0.00 ppm and 3.25 ppm) and at the two identified systematic pressures (125 mbar and 145 mbar).

To establish a basis of comparison with the LSM data presented in Figure 5.8, I introduce the "attachment fraction" parameter - a measure of the relative mean loss in energy for ^{37}Ar events having a rise-time within the select range of [150 μs, 200

μs]. Expressed as an equation, we have:

$$\text{Attachment Fraction} = \frac{\langle N_e \rangle_{[]150\mu s, 200\mu s]}}{\langle N_e \rangle_{<50\mu s}}, \tag{5.9}$$

where $\langle N_e \rangle_{[150\mu s, 200\mu s]}$ is the mean number of electrons within the rise-time range of [150 μs, 200 μs], and $\langle N_e \rangle_{<50\mu s}$ is the mean number of electrons within the rise-time range of [0 μs, 50 μs]. For real data, we can substitute the average number of electrons with the mean signal amplitude on the south channel for the given rise time cut; both energy scales are linearly proportional and comparisons via this method are therefore valid. The choice of equally sized rise time cuts in the attachment fraction formula are set to provide enough statistics and standardizes the radial selection of where event attachment is measured. The [0 μs, 50 μs] rise time domain is used as a reference point where minimal attachment occurs and is equivalent to the 0 ppm of O_2 case.

When applied to the data presented in Figure 5.8, using 1σ Gaussian uncertainties, I estimated a mean signal amplitude of 6.6x10^3 $\pm$ 1.4x10^3 ADU for a rise time cut of [150 μs, 200 μs] and 8.2x10^3 $\pm$ 1.6x10^3 ADU for rise times less than or equal to 50 μs. This yields an attachment fraction of 0.805 $\pm$ 0.040. It should be noted that this method is purely an estimator for assessing a reasonable set of systematic limits on O_2. It is recommended that a more rigorous analysis be studied by the NEWS-G collaboration in the future alongside a rigorous O_2 calibration methodology.

Performing this attachment fraction on a series of simulated ^{37}Ar data sets, we can graphically compare attachment fractions as shown in Figure 5.10. Here I performed simulations using the lower pressure systematic of 125 mbar since this would require the highest comparable O_2 concentration for observing the same attachment fraction as in the LSM data. I generated eight sets of simulated 125 mbar ^{37}Ar data with 10,000 starting events each roughly linearly spaced between 1.00 ppm and 7.00 ppm (plus one simulation at 0.50 ppm).

Empirical results suggest that the relationship between the attachment fraction and concentration of O_2 is linear, so a linear regression was performed on the entire

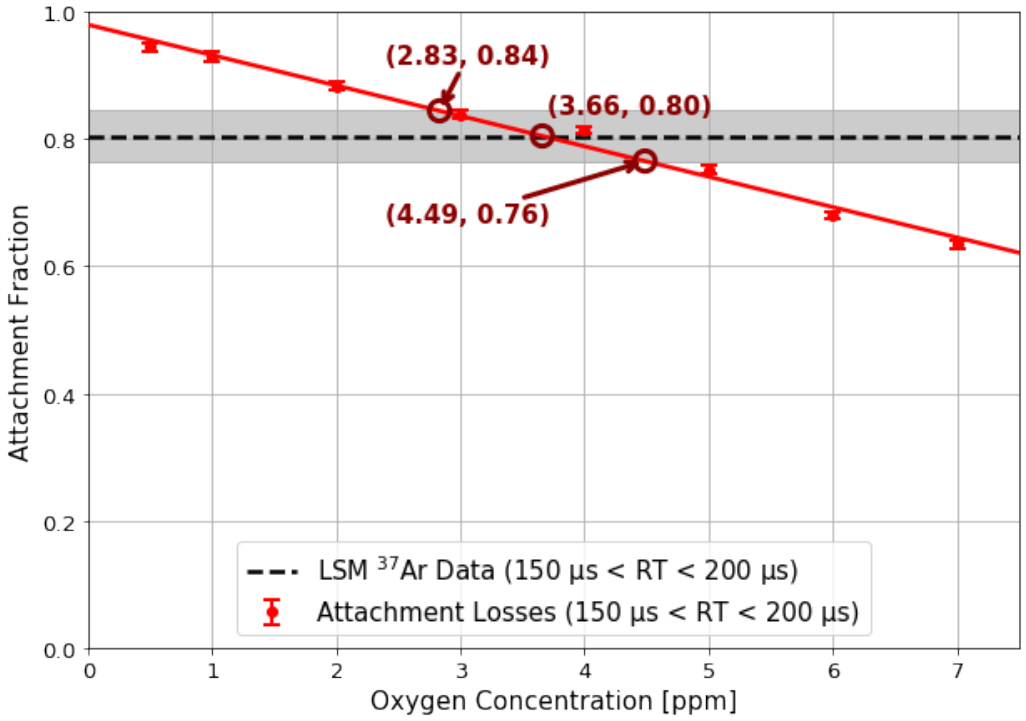

Figure 5.10: Simulation approximation measurement of O_2 concentration in S140 at LSM assuming a lower pressure systematic of 125 mbar. The approximate measurement intersection point occurs at 3.66 ppm (with 1σ of 0.83 ppm). Logarithmically and linearly spaced simulations in O_2 concentration were performed to assess the appropriate attachment fraction regime.

set of simulated data points. This line was found to intersect the 1σ uncertainty range on the LSM attachment fraction at concentrations of 2.83 ppm and 4.49 ppm. As the more conservative estimator, we consequently chose 4.49 ppm to be our upper systematic limit on the concentration of MAGBOLTZ O_2 concentration (not necessarily equivalent to the true O_2 concentration). This value represents a reasonable estimate of the largest concentration of O_2 needed in the MC drift simulation to ensure that similar levels of attachment to the LSM data are reflected in the ^{37}Ar calibration results. For simplicity, and due to the lack of a known O_2 calibration making the estimation of a lower systematic difficult, the lower systematic limit was chosen conservatively at 0.00 ppm - the truly pure CH_4 fill gas scenario.

5.2.2 Evaluation of Statistical Uncertainties

To characterize possible statistical variation in the resulting asymmetry fractions, large data sets of ^{37}Ar calibration events were simulated for each of the four systematic gas conditions identified in Section 5.2.1 (combinations of 125 mbar or 145 mbar gas pressure and 0.00 ppm or 4.49 ppm of O_2). These simulated data sets were chosen to contain 1e6 events each using random, uniformally distributed starting coordinates identical for each of the four sets for improved comparability. Of the 1e6 events, first, a cut is applied to remove "unobserved" events corresponding to when zero electrons reach any of the eleven anodes. The remaining events are then put through the signal amplitude construction process as described in Section 5.1.2. The final asymmetry results are then categorized based upon the [-0.75, 0.75] asymmetry cut.

The ratio of events in each of the north, south, and shared categories relative to the total number of events that passed the zero electron cut is taken as the mean ratio for each event categorization. The uncertainty on these values is taken as the normal approximation on a binomial (multinomial) proportion confidence interval:

$$\sigma_X = Z\sqrt{\frac{p_X(1-p_X)}{N}}, \tag{5.10}$$

where X labels either the north, south, or shared event category, σ_X is the ratio uncertainty of the particular event type, p_X is the probability of an event being in the specified event category (taken as the mean ratio for that event type), Z is the z-score value (we use either 1.00 or 1.96 here for 1σ 2σ uncertainties respectively), and N is the number of events which successfully passed the zero electron cut. Starting with an initial data set of size 1e6, typical uncertainties for each event ratio are found to be on the order of 1e-4 (or 1e-2 when reported as a percent).

5.2.3 Calibration Results

The following section lays out the ^{37}Ar simulation calibration asymmetry results for the four aforementioned MAGBOLTZ gas conditions using 1e6 event statistics. Tabu-

lated results are presented with and without corrective scaling, as described in Section 5.1.2 step (4), in Table 5.1 and Table 5.2 below.

Table 5.1: ^{37}Ar calibration tabulated results for unscaled simulated asymmetry data with 1σ binomial uncertainties.

	LSM Analysis	**P = 125 mbar 0.00 ppm O_2**	**P = 145 mbar 0.00 ppm O_2**	**P = 125 mbar 4.49 ppm O_2**	**P = 145 mbar 4.49 ppm O_2**
% North	22.73 ± 0.65	22.76 ± 0.04	22.83 ± 0.04	22.78 ± 0.04	22.86 ± 0.04
% South	68.38 ± 0.70	68.69 ± 0.05	68.83 ± 0.05	68.70 ± 0.05	68.83 ± 0.05
% Shared	8.88 ± 0.40	8.55 ± 0.03	8.34 ± 0.03	8.52 ± 0.03	8.30 ± 0.03

Table 5.2: ^{37}Ar calibration tabulated results for scaled simulated asymmetry data with 1σ binomial uncertainties.

	LSM Analysis	**P = 125 mbar 0.00 ppm O_2**	**P = 145 mbar 0.00 ppm O_2**	**P = 125 mbar 4.49 ppm O_2**	**P = 145 mbar 4.49 ppm O_2**
% North	22.73 ± 0.65	23.29 ± 0.04	23.33 ± 0.04	22.89 ± 0.04	22.71 ± 0.04
% South	68.38 ± 0.70	68.86 ± 0.05	69.01 ± 0.05	68.44 ± 0.05	68.30 ± 0.05
% Shared	8.88 ± 0.40	7.85 ± 0.03	7.66 ± 0.03	8.67 ± 0.03	8.99 ± 0.03

The unscaled asymmetry results, presented in Table 5.1, imply a combined systematic range on the north fraction of events as [22.72%, 22.90%], south fraction of events as [68.64%, 68.88%], and shared fraction of events as [8.27%, 8.58%]. For the scaled asymmetry results, presented in Table 5.2, we have a systematic range on the north fraction of events as [22.67%, 23.37%], south fraction of events as [68.25%, 69.06%], and shared fraction of events as [7.63%, 9.02%]. As shown visually in Figure 5.11 there is also overlap (i.e. agreement) with the LSM data analysis results (the coloured background domains) for both unscaled (bold) and scaled (faded) results. The scaled results display a greater variability than the unscaled results, but nevertheless stay within agreement of the LSM analysis.

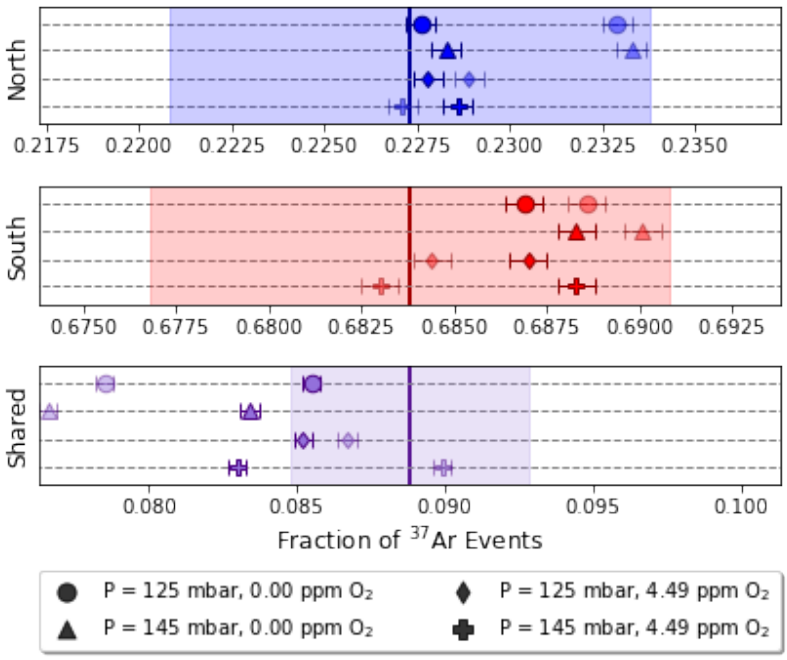

Figure 5.11: Combined simulated ^{37}Ar asymmetry calibration results for scaled and unscaled data. Unscaled asymmetry data points are faded relative to the scaled asymmetry data points.

The conclusion from these calibration results is that the MC drift simulation method is capable of recreating the same geometric distribution of events as observed in the LSM data. Despite the assumptions made during the signal amplitude reconstruction process, the final asymmetry results with and without scaling are in agreement with the observed asymmetry in the LSM data suggesting rigidity in the method. It is reasonable to assume that further characterization of the north channel anode gains and gain uncertainties would not throw these results into disagreement due to observations in the correctively-scaled results. It can be safely assumed that this MC drift simulation can be an effective predictive tool for characterizing the fiducialization of low-energy events, as explored in the following section.

5.3 Study of the Low-Energy Fiducialization of S140

With a clear agreement in ^{37}Ar calibration results, this validates the use of the MC drift simulations as a predictive tool in studying the geometric distribution and fidu-

cialization of low-energy events in S140. In this section, we will first demonstrate the fiducialization of select low-energy events with 2, 3, and 4 primary electrons as well as looking at the direct use of this MC drift simulation tool for determining south-channel fiducialization efficiency cuts for use in setting S140's mass exposure in the LSM data analysis.

5.3.1 Low-Energy Fiducialization for $2e^-$ to $4e^-$ Events

As with higher energy events, like 2.8 keV ^{37}Ar events, lower energy events with only a few electrons can be simulated in similar fashion. However, to speed up simulations we can also make use of pre-existing simulated data sets, such as those generated during the ^{37}Ar calibration study of the previous chapter, and simply sample electrons to create sets of electron data. All of the data sets presented in this section make use of sampling from the ^{37}Ar calibration data. Specifically for this section, all presented event ratios were calculated using 1,000 data sets of $5\text{x}10^6$ events each. Five low-energy events were sampled from each of the $1\text{x}10^6$ simulated ^{37}Ar calibration events.

The advantage now of studying S140's fiducialization is that only the distribution of simulated electrons' drift-terminating anodes are needed to calculate a fraction of a particular predefined event species. Since in the simulation we know exactly where each electron terminates its drift, this process is simply a matter of counting electrons by event and categorizing their final coordinate location. As an example, I present in Table 5.3 a set of two-electron events where every possible permutation given for our MAGBOLTZ systematics.

The next three tables present low energy results for events with 2, 3, and 4 electrons in Tables 5.4, 5.5, and 5.6 respectively. The main difference here with Table 5.3 is that we assume that each electron must successfully reach an anode for the event to be counted. This provides better direct comparability not only between simulations under different gas conditions, but also allows us to establish trends for events of dif-

Table 5.3: Full break down of simulated 2 electron results for 1,000 data sets of 5x10^6 events with 1σ binomial uncertainties. All possible permutations are shown for both electrons, grouped based upon typical event classifications.

	e^-_1	e^-_2	P = 125 mbar 0.00 ppm O_2	P = 145 mbar 0.00 ppm O_2	P = 125 mbar 4.49 ppm O_2	P = 145 mbar 4.49 ppm O_2
North-5	N5	N5	20.58 ± 0.02	20.70 ± 0.02	13.51 ± 0.01	10.59 ± 0.01
	N5	L	0.268 ± 0.002	0.275 ± 0.002	7.23 ± 0.01	9.12 ± 0.01
South-5	S5	S5	58.20 ± 0.02	58.12 ± 0.02	40.49 ± 0.02	32.27 ± 0.02
	S5	L	0.592 ± 0.003	0.619 ± 0.004	17.17 ± 0.02	22.80 ± 0.02
South-1	S1	S1	9.54 ± 0.01	9.57 ± 0.01	6.84 ± 0.01	5.55 ± 0.01
	S1	L	0.091 ± 0.001	0.099 ± 0.001	2.825 ± 0.007	3.827 ± 0.009
Shared	N5	S5	7.51 ± 0.01	7.33 ± 0.01	4.88 ± 0.01	3.643 ± 0.008
	N5	S1	0	0	0	0
	S5	S1	2.975 ± 0.008	2.871 ± 0.008	2.085 ± 0.006	1.600 ± 0.006
Lost	L	L	0.426 ± 0.003	0.414 ± 0.003	4.97 ± 0.01	10.60 ± 0.01

ferent sizes. Here we also assume that a "pure" north or south event must exclusively contain electrons in the appropriate channel.

Table 5.4: Fiducialization results for 2 electron events. Computed for 1,000 data sets of 5x10^6 events each with 1σ binomial uncertainties. Only events where both electrons reach an anode are counted.

	P = 125 mbar 0.00 ppm O_2	P = 145 mbar 0.00 ppm O_2	P = 125 mbar 4.49 ppm O_2	P = 145 mbar 4.49 ppm O_2
% North	20.87 ± 0.02	21.00 ± 0.02	19.92 ± 0.02	19.74 ± 0.02
% South	71.52 ± 0.02	71.57 ± 0.02	72.88 ± 0.02	73.47 ± 0.03
% Shared	7.61 ± 0.01	7.43 ± 0.01	7.20 ± 0.01	6.79 ± 0.02

In summary, the systematic ranges of the north channel fraction of events in order of increasing electron count is given as: [19.72%, 21.02%], [17.79%, 19.04%], and [16.51%, 17.76%]. For south electrons we have: [71.50%, 73.50%], [69.68%, 72.34%], and [68.57%, 71.62%]. Lastly, for shared events we have: [6.77%, 7.62%], [9.89%,

Table 5.5: Fiducialization results for 3 electron events. Computed for 1,000 data sets of 5x10^6 events each with 1σ binomial uncertainties. Only events where all three electrons reach an anode are counted.

	P = 125 mbar 0.00 ppm O_2	**P = 145 mbar 0.00 ppm O_2**	**P = 125 mbar 4.49 ppm O_2**	**P = 145 mbar 4.49 ppm O_2**
% North	18.88 ± 0.02	19.02 ± 0.02	17.83 ± 0.02	17.82 ± 0.03
% South	69.70 ± 0.02	69.81 ± 0.02	71.65 ± 0.03	72.31 ± 0.03
% Shared	11.42 ± 0.01	11.17 ± 0.01	10.52 ± 0.02	9.87 ± 0.02

Table 5.6: Fiducialization results for 4 electron events. Computed for 1,000 data sets of 5x10^6 events each with 1σ binomial uncertainties. Only events where all four electrons reach an anode are counted.

	P = 125 mbar 0.00 ppm O_2	**P = 145 mbar 0.00 ppm O_2**	**P = 125 mbar 4.49 ppm O_2**	**P = 145 mbar 4.49 ppm O_2**
% North	17.54 ± 0.02	17.74 ± 0.02	16.53 ± 0.02	16.78 ± 0.02
% South	68.59 ± 0.02	68.71 ± 0.02	70.93 ± 0.03	71.59 ± 0.03
% Shared	13.87 ± 0.02	13.55 ± 0.02	12.54 ± 0.02	11.63 ± 0.02

11.43%], and [11.65%, 13.89%]. From these results, we can observe that as we increment the number of electrons, this added degree of complexity increases the likelihood that at least one electron crosses over to an opposing channel. The ratio of purely south events, of most interest for use in the LSM data analysis, clearly shrinks as we go to higher energy events.

5.3.2 South Channel Fiducialization Efficiency Cuts

For the pure 135 mbar CH_4 LSM data analysis in setting new WIMP-nucleon cross section limits for the NEWS-G collaboration, the fiducialization of S140, as determined via the simulation framework presented in this work, is used as a factor of determining the effective mass exposure of the S140 during the measurement campaign. At LSM, ∼9.8 days worth of south-trigger data were recorded with a total of ∼114 g of CH_4 (∼28.7 g of hydrogen). As established throughout this chapter,

by limiting ourselves to south-trigger data only, the total available fiducial volume, and thus the effective mass exposure of S140 will change compared to the analyses with the inclusion of north-trigger data. Therefore, for practical use, we must look at how the fiducialization of S140 behaves for specific event energies of interest: near low-threshold energies. In the LSM analysis, the minimum energetic events that can be successfully identified with sufficient information on diffusive properties (ability to identify origination, for example as surface event, etc.) via signal analysis consist of two electrons. Single electron events are ignored for the purposes of the offline analysis despite S140's sensitivity to these energies due to a lack of information on their origin.

The other, unaddressed aspect of the low-energy fiducialization of S140 is that the fraction of pure south events as defined in the previous section does not paint the complete picture. The likelihood of a given low-energy event falling into either the north, shared, or south categories is a function of the initial 3-D spatial coordinates of said event. Therefore, there will be a spatial efficiency to any mass-exposure cuts placed upon data used for setting new WIMP-nucleon limits.

The specific simulation measurable that we will look at is the ratio of events where zero electrons reach the north channel ($N5^{(0)}$) to all events ($A11^{(0+)}$) because such events would be rejected by the offline analysis cuts. As examples of their spatial dependency, I present the plots in Figure 5.12 which illustrate sample spatial distributions for this ratio.

Three types of low-energy events are looked at here: 2 (top), 4 (middle), and 10 (bottom) electron events. The left column displays each event type's radial (r-dependent) fiducialization efficiency for each of the four systematic MAGBOLTZ gas conditions. Each data point, or bin, in the simulated data presented in this column was computed by sampling 10,000 N electron events from existing simulated ^{37}Ar data over 100 trials per bin. The resulting mean and standard deviation of the distribution for each bin with 100 trials is taken as the bin value and 1σ uncertainty. These

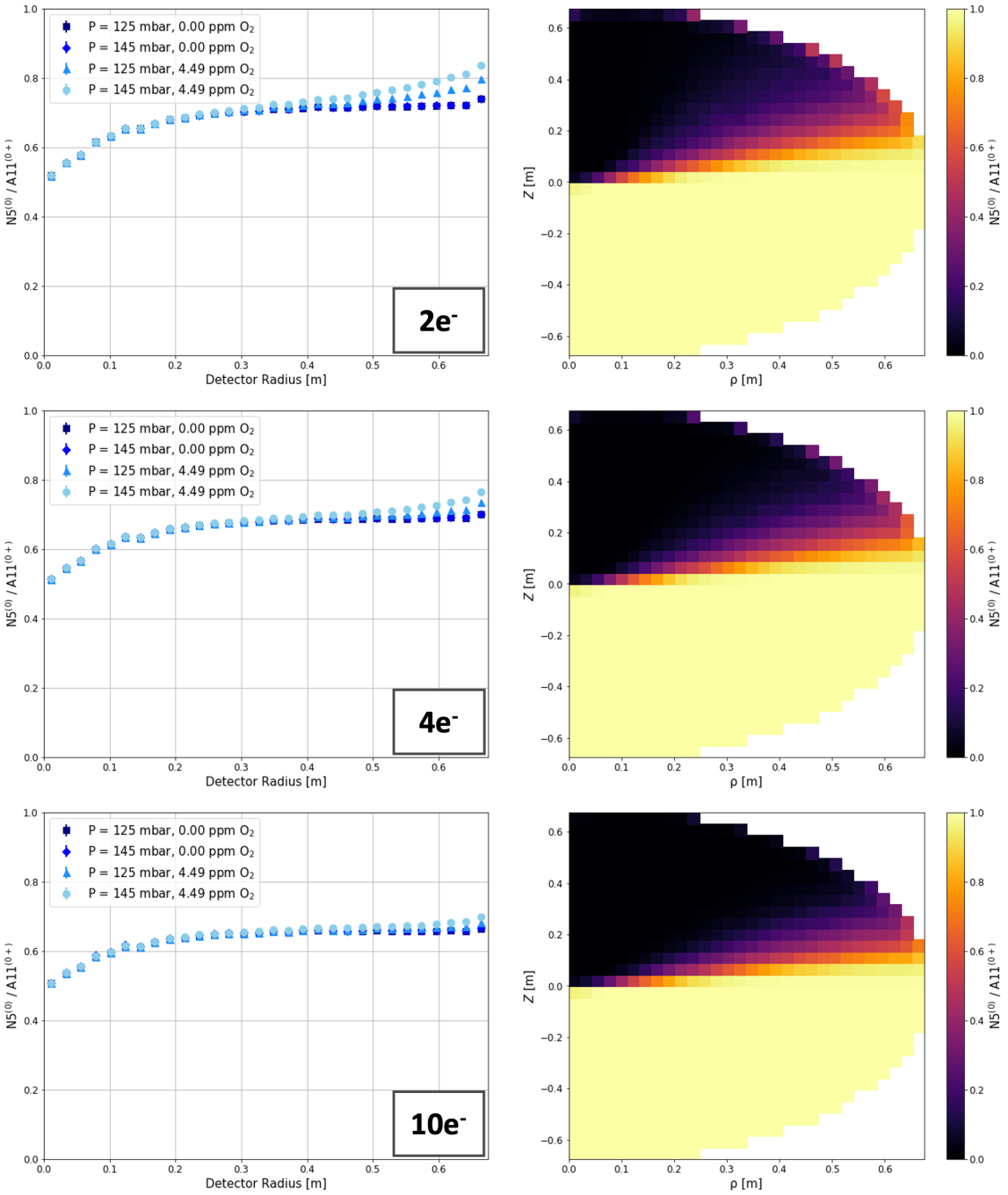

Figure 5.12: Visualizations of the south-channel fiducialization efficiency for select low-energy events in varying gas conditions as a function of S140 radius (left column) and in the z-ρ plane (right column). 1σ uncertainties on the fractional points on the left columned data are too small to visualize (order 5e-3).

specific events were selected to reflect Tables 5.4 (2 e^-) and 5.6 (4 e^-) at near-energy-threshold levels, plus a select slightly higher energy event (10 e^-) to gauge the rate of

convergence between spatial variations under different gas conditions. As expected, in scenarios where there is a greater likelihood of attachment and fewer initial electrons, the likelihood of events being unobserved (complete electron attachment) increases. Therefore, the scenario where there is 125 mbar of gas pressure and 0 ppm of O_2 represents the most conservative efficiency on $N5^{(0)}$ events. The two-dimensional plots in the right column are for the same sets of data redistributed as a function of z and ρ (the polar angle about the z axis of S140). The data in this column are only displayed for the most conservative gas conditions mentioned prior.

Using this information, in setting fiducialization efficiency we will narrow our scope to the conservative case of removing $N5^{(0)}$ (125 mbar, 0.00 ppm O_2) and look at the r-dependent fiducialization efficiency of 1 through 15 electron events (1 electron events are included for a more complete picture, but are not used in the WIMP-limit analysis). 15 electron events are selected as our upper-energy events of interest due to computational times in the CH_4 WIMP analysis code.

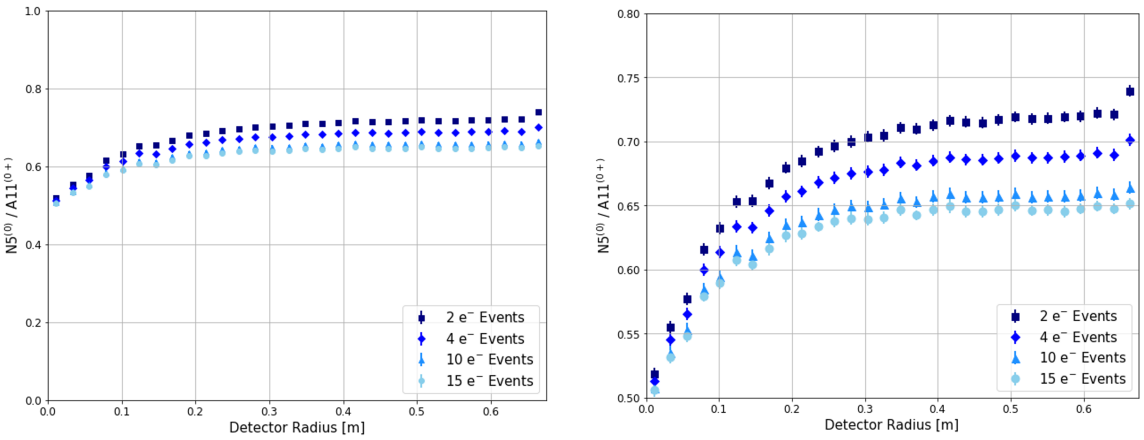

Figure 5.13: (Left) Simulated south-channel fiducialization efficiencies for select low-energy (few electron) events as a function of S140 radius, r. (Right) Narrower axis range highlighting 1σ uncertainties (order 5e-3). The ratio $N5^{(0)}/A11^{(0+)}$ selects all events where zero electrons reach a north channel anode out of all simulated events. The integration of these curves identifies the effective mass of S140's volume for the respective event category, placing a cut on the mass acceptance.

It is this simulated data and binomial uncertainties which are to be used in the WIMP-limit analysis for the 135 mbar CH_4 LSM data. Using these simulated $N5^{(0)}$

efficiencies, we can remove events as a function of event energy (i.e. number of electrons) and radial origin; specifically the integration of such efficiency curves is used to remove a fraction of the nominal detector mass. As expected, the lower in energy the event is, the smaller the fiducialization cut due to an increased probability of zero electrons reaching the north channel. The ultimate WIMP-nucleon cross section limits that this result contributes towards will be released soon after the publication of this thesis, with more details to be found there.

At this stage there are still a few things to be verified with the current south channel efficiency curves. When looked upon closely, specific fluctuations in the curvature of each data set appear correlated with one another. It is unknown as to whether some of the finer structures of these efficiency curves are a consequence of a physical aspect of the detector, a consequence of the COMSOL electric field model, or a deficiency in the event sampling methodology. Therefore, two tests are planned: first, to redo the south channel fiducialization efficiency curves using uniquely generated non-sampled events and, secondly if necessary, to generate curves for differing COMSOL mesh resolutions. The purpose of this second step is to verify whether or not the observed correlated fluctuations are a consequence of calculation errors or general systematic uncertainties present within the COMSOL electric field modelling. If consistent between models, it is possible that such fluctuations observed in these efficiency curves are indeed some sort of physical quality of the data.

5.4 Summary and Future Applications of MC Electron Drift Simulations

The use of a MC electron drift simulation to characterize the fiducial volume of a 2-channel ACHINOS sensor in S140 for the LSM campaign has proved to be a fruitful effort. Thanks to a successful calibration using ^{37}Ar data, the simulation framework's use in the low-energy fiducialization study presented in this chapter yielded results useful for setting cuts on the effective mass exposure for S140. Moving for-

ward, following the release of the WIMP-nucleon cross section limits and analysis to be published soon by the NEWS-G collaboration, the application of simulations for future NEWS-G projects like S140 at SNOLAB will be of mind. As discussed in Chapter 4, the simulation framework is continually being improved upon including further study of "space-charge" effects and other secondary ionic interactions of drifting particles. Advances in analysis, calibration, and or general simulation techniques are to be determined, but the work presented in this thesis lays the groundwork for a successful and informative simulation method in the first-principles study of different SPC physics.

In the future, this simulation framework may apply to the study of other facets of SPC applications including the study of a directionality channel. As discussed in Chapter 2, one of the upcoming challenges for direct detection experiments is contending with prominent CEνNS backgrounds found in the "neutrino floor" [26, 59]. Since CEνNS backgrounds in NEWS-G's energy regime of interest originate primarily from the Sun, having the capacity to discriminate a solar axis of events via the measurement of incident event directionality could prove to be a pivotal aspect of future direct detection technologies. For SPCs specifically, with the use of this simulation architecture including full ACHINOS anode discrimination, the study and reconstruction of track-like events may be possible. By simulating gas conditions favourable for large path-length events, the fiducialization analysis on an anode-by-anode basis may provide insight into the resolution and path reconstruction capabilities of an even greater multi-channeled ACHINOS sensor. This, combined with advances in Shockley-Ramo simulations to study increased channel cross-talk could be the key to unlocking the directionality channel in SPCs, critical for future SPC detectors with heightened sensitivity like DarkSPHERE [79].

Chapter 6

Developments in Instrumentation for S140's Gas Handling System

At the University of Alberta, one of NEWS-G's primary endeavors is the development of instruments for use in the gas handling system of S140 at SNOLAB. Since S140 is a gaseous detector, the complete operation of such an apparatus requires many external systems required for preparing and replacing the fill gas of the SPC including gas purification, monitoring, and pumping. For the SNOLAB installation, many of these systems are already developed and in place on-site underground, but future systems are in development or undergoing iterable improvements throughout the NEWS-G collaboration.

This chapter will focus on the University of Alberta NEWS-G team's development of systems for gas purification and monitoring. Specifically, the development of a radon trap, designed and tested by P. O'Brien [66], will be briefly covered alongside one of the main focal points of this thesis: the development of a prototype methane-monitoring system using Laser Absorption Spectroscopy (LAS). The efficacy of the radon trapping system at both the removal of radon, but also other desirable gases like methane, requires a new system for performing absolute gas concentration measurements. Current prototype apparatus designs, analysis techniques, calibration, and operational tests will be discussed alongside planned iterative improvements to address current deficiencies in system performance.

6.1 S140 Gas Handling System

For the installation at SNOLAB, the design of S140's gas handling system has been largely finalized since 2019 by NEWS-G's engineering team at Queen's University lead by K. Dering alongside S. Crawford. This system covers all gas inputs, purification systems, vacuum system, and other components related to the fill gas of S140. Specifically, the gas handling system that will be the focus of discussion is related to the detector once fully installed on-site at SNOLAB's Cube Hall [6]. This section will take a closer look at the overall system design, current installation, and the specific plans and status for the radon trapping system developed at the University of Alberta.

6.1.1 System Overview

The original design plans for S140's gas handling system at SNOLAB can be divided up into six main sections. While not all sections are currently in use or even installed on-site, the schematic P&ID diagram presented in Figure 6.1 highlights each section which are detailed below.

Green: Gas Containment & Input

Highlighted in green are the stored gas containers. These gases represent possible fill gases (including prepared gas mixtures) for the detector prior to any purification stages. Choice gases for S140 at SNOLAB include Ne + CH_4 mixes, Ar, N_2, and pure CH_4. Initial physics runs with S140 will make use of Ne + ∼6-10% CH_4 gas mixtures, but plans for pure CH_4 data runs like those performed at LSM are currently under consideration within SNOLAB's operational guidelines.

Orange: Purification & Circulation

The orange highlighted section represents the gas purification and circulation board, containing a number of systems and potential instruments at the heart of the gas

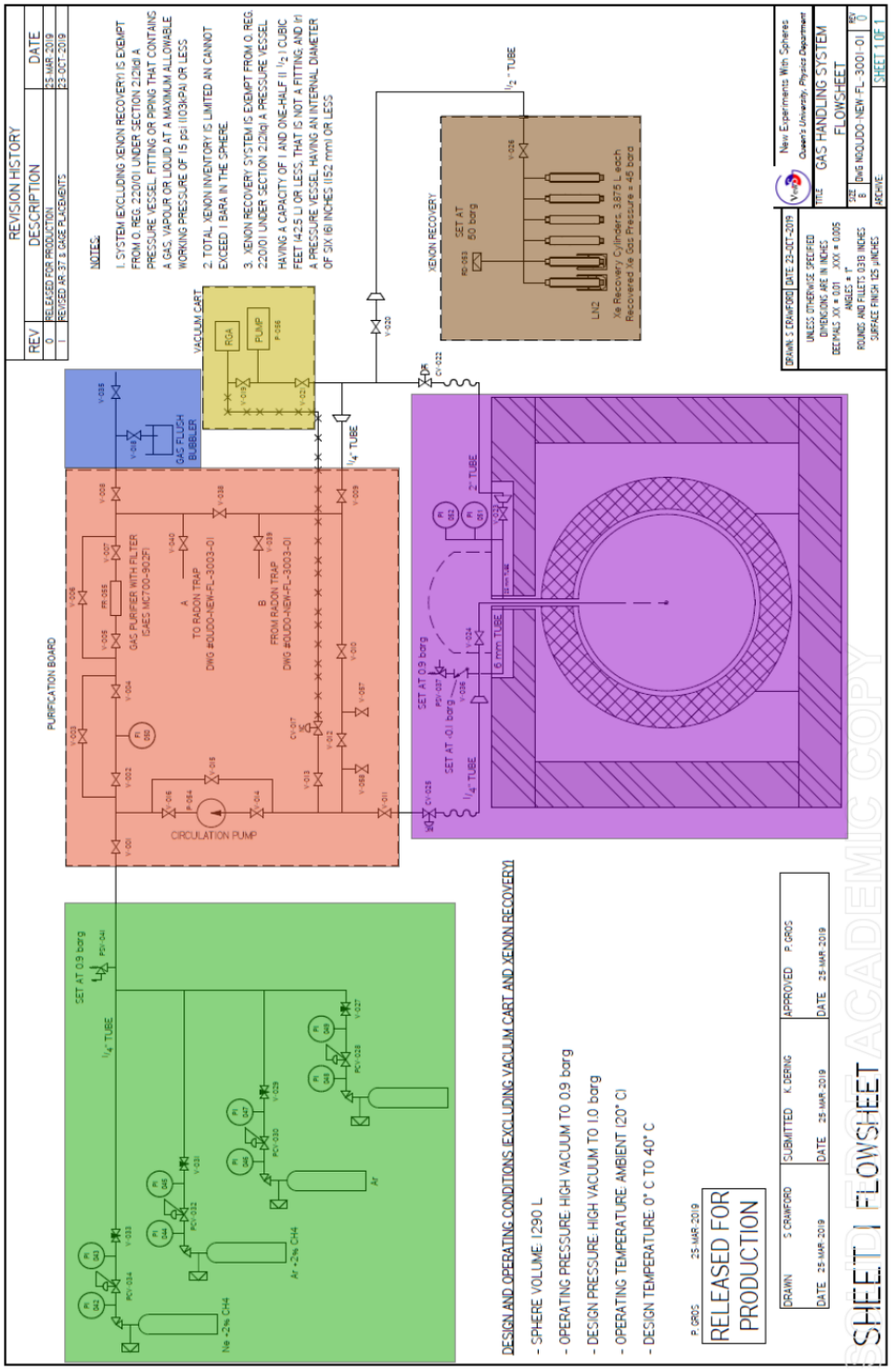

Figure 6.1: P&ID diagram of S140's gas handling system on-site at SNOLAB. The sections include the gas supply (green), purification system (orange), exhaust (blue), vacuum pump and RGA (yellow), xenon recovery system (brown), and detector itself (purple). Credit: S. Crawford and P. O'Brien.

handling system. The components here are mounted onto a custom-made gas handling board as photographed in Figure 6.2. The instruments mounted on the board in this section include a Getter (a type of gas purifier), the radon trap (to be discussed later in Section 6.1.2), and circulation pump. The circulation pump is used to flow gas through both purification systems. The Getter removes electro-negative contaminants found in air like O_2, N_2, and water vapour. The radon trap's purpose is to remove radon from the fill gas prior to entering the sphere, preventing radioactive contamination of the detector and excessive backgrounds.

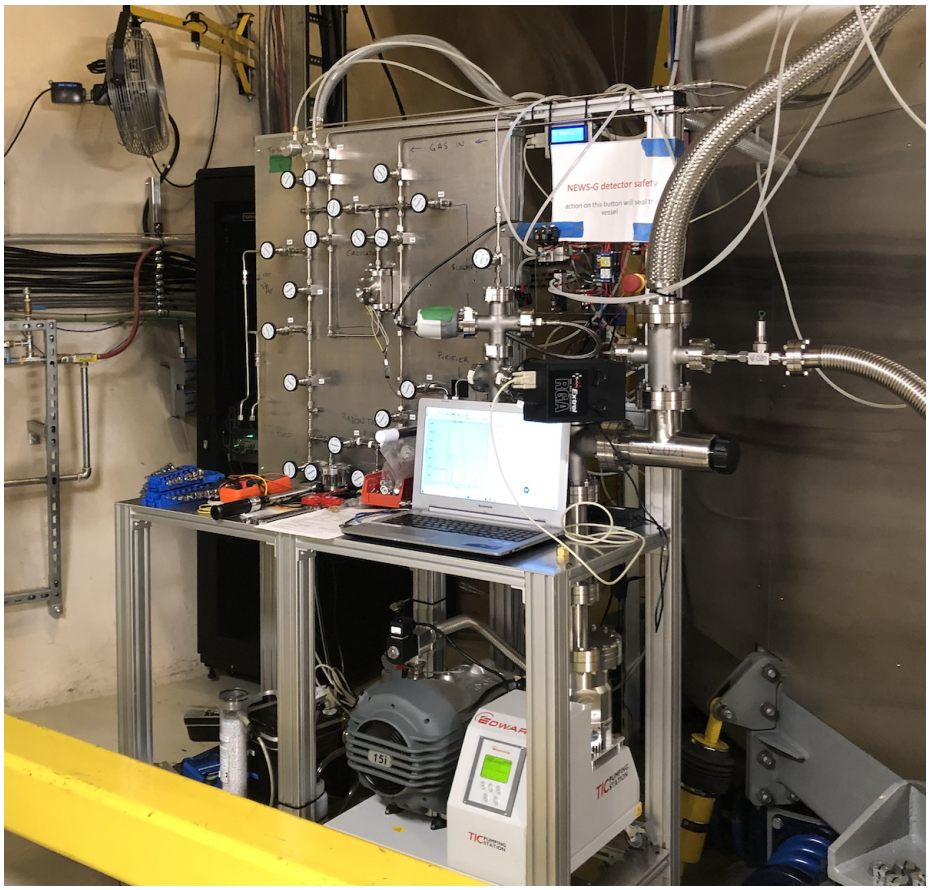

Figure 6.2: Photograph of the gas handling board at SNOLAB with mounted piping, valves, and purification instruments as indicated in orange in Figure 6.1. The vacuum pump is also depicted below the gas handling board.

Blue: Exhaust

In blue is the exhaust port of the gas handling system where over-pressure gas can be removed from the gas handling system and or detector (in accordance with SNOLAB regulating guidelines). A "bubbler" setup can be placed in parallel to indicate the flow of gas exiting the system.

Yellow: RGA & Vacuum Pump

The yellow highlighted portion of the P&ID diagram covers the vacuum pump and RGA (Residual Gas Analyzer). The vacuum pump is the global pumping unit for the entire gas handling system, including the detector itself. Vacuuming of the entire detector can allow for the fill of new gases. The RGA serves as a low-pressure ($\sim$ 1x10^{-7} bar) monitor for gas concentrations, mainly used for measuring trace contaminants like O_2 and H_2O.

Brown: Xenon Recovery

Highlighted in brown is a proposed xenon recovery system. Due to the high cost of operating a large SPC with xenon gas, physics runs with xenon have largely been abandoned since the original development of this P&ID diagram in favour of cheaper, and more readily available noble gases such as argon and neon. However, NEWS-G still has recovery systems on hand if necessary with this particular sub-system installable if required.

Purple: S140 Detector

The final section in the diagram is the S140 detector itself, this is the final stage of the gas handling system where purified fill gases enter the detector volume from the top of the detector. This section is isolated from the rest of the gas handling system during detector operation.

6.1.2 UofA Radon Trapping System

The radon trapping system illustrated in Figure 6.1 has not yet been installed at SNOLAB. A prototype radon trapping system has been in development at the University of Alberta with the design and initial testing preformed by P. O'Brien [66]. The purpose of this system is to remove contaminant radon molecules within the fill gas prior to entering the detector in an effort to prevent radioactive backgrounds. The primary backgrounds of concern are sourced from two radioisotopes of radon: ^{220}Rn and ^{222}Rn. These two radioisotopes are created via the decay of ^{238}U and ^{232}Th respectively, both of which are naturally occurring within most materials. These radioisotopes of radon have relatively short half-lives: 3.82 days for ^{220}Rn and 55 seconds for ^{222}Rn [95]. Both decay via the production of alpha particles - producing highly energetic backgrounds within S140. Studies by former Ph.D. student A. Brossard found that the acceptable limit of radon contamination within the fill gas of the detector should not exceed radioactivity levels on the order of 1 mBq [96], placing an absorption efficiency target onto the new radon trapping system design.

The prototype design for the radon trap consists of a ∼20 cm long 1/2" stainless steel pipe filled with an absorbent filter held inside by internal fibreglass caps. This pipe, along with a bypass to allow for the option to open and close the trap, would be installed in series with a test gas circulation setup. Since radon is an inert gas, it is extremely rare for it to react with other substances, therefore non-chemical properties must be used to strip it from bulk gases. The solution proposed by P. O'Brien was to use materials with optimal absorptive properties for absorbing radon atoms [66]. Select materials that were tested with suitable properties included activated charcoal (a.k.a. activated carbon), such as Carboxen®, and a new absorbent made of silver zeolite [97]. For testing the efficacy of the radon trap for different materials and under different gas conditions, a test gas circulation setup was prepared at the University of Alberta following the P&ID diagram in Figure 6.3.

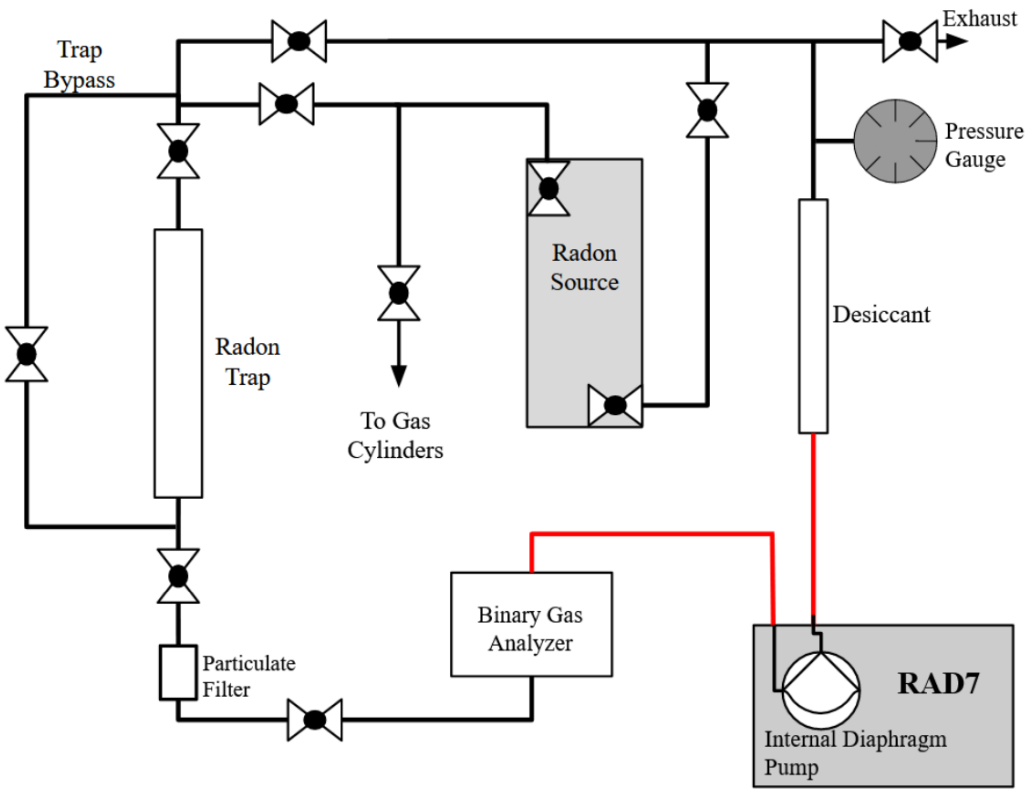

Figure 6.3: P&ID diagram of the gas circulation system used for testing UofA's custom radon trap [66]. Red lines indicate the use of flexible pipes where as black lines indicate 1/2" stainless steel piping. Credit: P. O'Brien.

In this test configuration, ^{222}Rn from a Pylon 1025 ^{226}Ra source could be injected in circulation with the selected fill gas to test the losses in radon activity when exposed to the trap. A RAD7 device was also used in series to monitor the concentration of radon for the duration of any measurement period. In order to reset the trap to perform any new measurements, the trap would be heated using a hot air gun (for $\sim$20 minutes) causing the absorbent material to release trapped gas molecules.

The principle quantity for characterizing the efficacy of a given radon trapping material under different gas conditions is called the radon reduction ratio, R:

$$R = \frac{A_0}{A_{f,avg}}, \tag{6.1}$$

where A_0 is the initial radon activity prior to the trap being opened (as measured

by the RAD7) and $A_{f,avg}$ is the average "final" radon activity (the time period for determining the "final" activity is experiment-specific). The exact time frame over which R is determined must be the same per measurement run for valid comparisons. Tests were performed initially by P. O'Brien as well as later by J. Hernandez following the work presented in P. O'Brien's Masters thesis [66]. Test measurements were performed at both room temperatures and sub-zero (-80°C) temperatures for Ar, N_2, and Ar + 3% ($\pm$10%) CH_4 for both trapping materials [66]. In order to perform sub-zero temperature measurements, dry-ice was used in a Styrofoam container to cool down gas entering the radon trap through a segment of bent 1/2" piping. The system with the added coolant piping is photographed in Figure 6.4 (a) and with the Styrofoam container in Figure 6.4 (b). The most recent version of the radon trapping system features a new regeneration (i.e. heating) system using a wrapping of 1/2" silicon heating tape as depicted in Figure 6.4 (c).

A summary of tests that have been performed by P. O'Brien and J. Hernandez are displayed in Figure 6.5 where their respective R-values are compared. These tests have demonstrated that the more effective radon trapping material without the need for a coolant is silver zeolite, with measured R-values of on the order of up to ~1e5 (Carboxen®attains similar R-values, but only under the dry ice conditions). What is of notable importance is that silver zeolite, unlike activated charcoal, is effective at removing radon from circulation at room temperatures (R ~1e5).

Despite the proven effectiveness of silver zeolite as a trapping medium for radon, there are some drawbacks with this system. It was also notable that during test with Ar-CH_4 mixtures while monitoring relative gas concentrations with a Binary Gas Analyzer (BGA, also in circulation as shown in Figure 6.3) that the trap appears to absorb some amount of CH_4 alongside radon [66]. Evidence, such as in the BGA time-span plot in Figure 6.6, illustrate a sudden drop in concentration as the trap is opened. In this figure, activated charcoal was used at sub-zero temperatures, but similar evidence has been found for both trapping materials and even at room

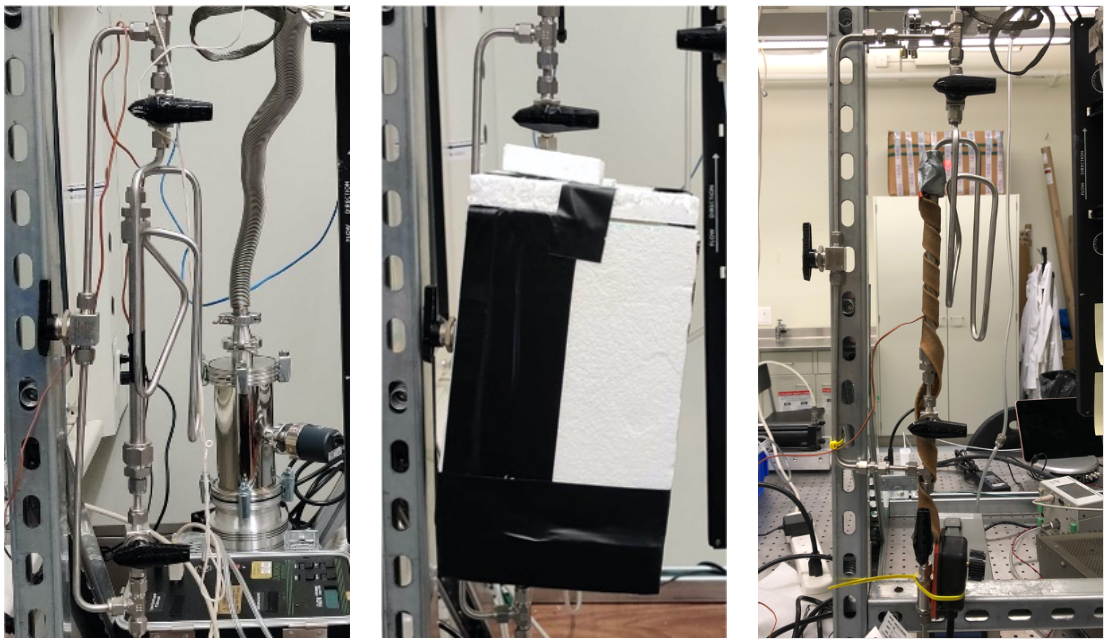

(a) (b) (c)

Figure 6.4: Photographs of different configurations of the radon trap system in circulation as depicted in Figure 6.3. (a) The radon trap during room temperature tests by P. O'Brien and J. Hernandez [66]. (b) Styrofoam container for dry ice storage and cooling during -80° C tests by P. O'Brien [66]. (c) Current radon trap setup with silicon tape for heating and the regeneration of the trapping material.

temperature [66]. Unfortunately, due to changes in gas composition and non-static kinematics, the BGA is an unreliable means of ascertaining the exact loss in CH_4 concentration. It is also unknown if for trace levels of initial radon whether or not the intial concentration of radon and or methane affects the absorption efficiency of the radon trap. Therefore, new methods in CH_4 monitoring are required for evaluating these unknowns, as will be explored next in the next section.

6.2 Laser Absorption Spectroscopy

As a consequence of the evident losses in the concentration of CH_4 through the use of the prototype radon trap, an effective means of measuring and monitoring the absolute concentration of CH_4 is required. As discussed in Chapter 2, CH_4 as a choice fill gas or fill gas component serves two critical roles within an SPC detector. First, CH_4 acts

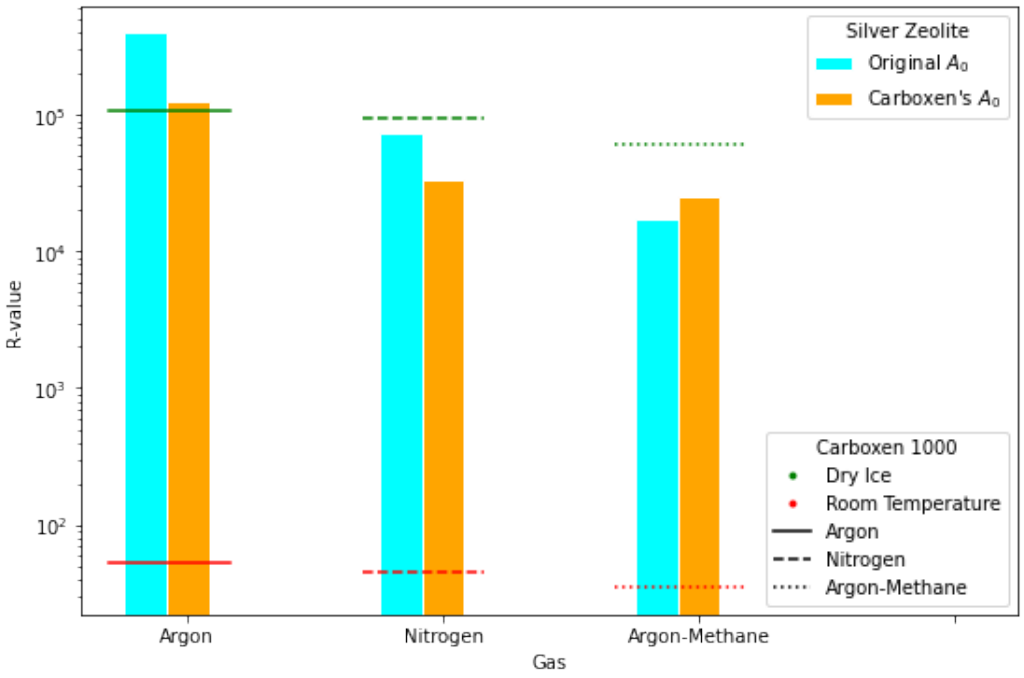

Figure 6.5: Compiled data summarizing radon trap tests recorded by P. O'Brien [66] and J. Hernandez for different trapping media (silver zeolite and Carboxen®) at dry ice temperatures (-80°C) and lab temperatures. Credit: J. Hernandez.

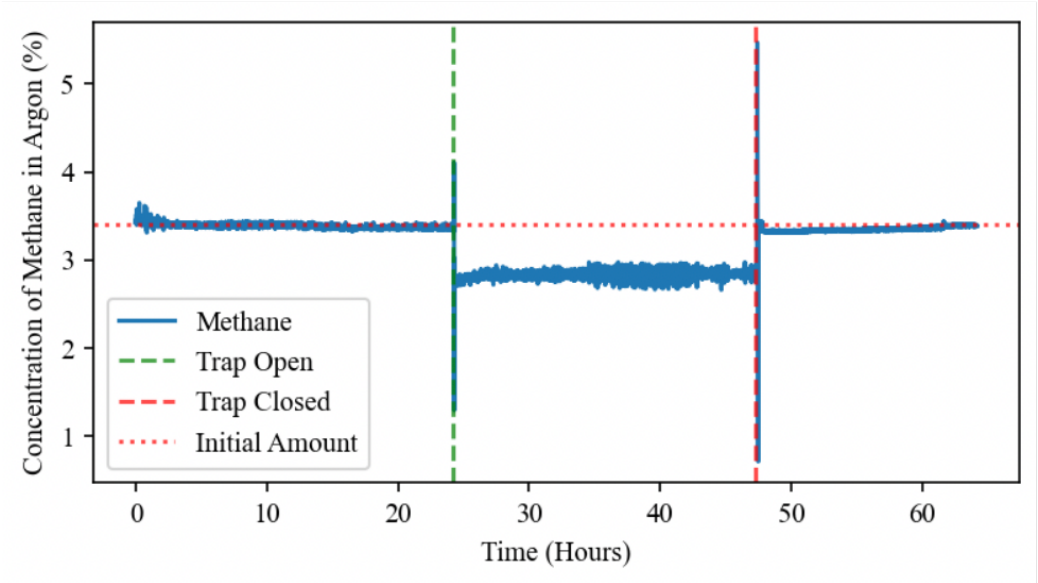

Figure 6.6: Carboxen tests at -80° C demonstrating relative changes in CH_4 concentration after opening the radon trap [66]. Regenerating the trap appeared to recover approximately the CH_4 concentration that was lost to the trap initially.

a gas quencher with a $\leq$10% concentration used to maintain the proportionality of an SPC's signal, preventing runaway tertiary ionization [4]. Secondly, the hydrogen atoms present within each CH_4 molecule serve as ideal nuclear recoil targets for lower-massed WIMPs - the speciality of NEWS-G's SPC detectors for use in direct detection experiments. While the exact concentration of CH_4 used in the fill gas mixture for a given SPC depends upon the specific experiment (e.g., 0.7% with SEDINE [4], 100% with S140 at LSM [5], etc.), notably in the cases where noble gases are used as the primary fill gas, evidence suggests that the use of the radon trapping system will reduce the nominal concentration of CH_4 prior to filling [66]. For example, with S140 at SNOLAB, a fill gas of Ne + up to 10% CH_4 is planned to be used, but the radon trap may remove a fraction of this nominal CH_4 concentration from the mixture during the pre-fill gas circulation phase. This has a consequence in directly impacting possible cross-section limits produced from these experimental runs by reducing the mass of hydrogen within the detector volume, and thus the possible mass exposure to a WIMP signal.

Since the Binary Gas Analyzer (BGA) only provides relative, and often unreliable, concentration data for a static two-gas system, an alternative method for reliably measuring the absolute concentration of CH_4, regardless of gas kinematics, would prove a more effective solution for CH_4 monitoring with S140's gas handling system. Additionally, an ideal system would contain zero noise and fit in-line with the purification system (highlighted in orange in Figure 6.1) to perform measurements at near-atmospheric gas pressures. One explored option would be an RGA (Residual Gas Analyzer) system, however an RGA poses two challenges. In order to operate in-line with near-atmospheric level gas pressures, the RGA would require a gas-sampling capillary which would not be directly in-line with the gas circulation. This is because an RGA would require its own pumping unit in order to operate at vacuum or near-vacuum pressures. An RGA pump would introduce a new source of acoustic noise for the entire S140 setup, plus the gas sampling efficiency based upon the flow rate

of the RGA capillary does not necessarily guarantee a reliable gas measurement.

One other possible solution came about in late 2019 through collaborative discussions with the University of Alberta's Professor A. Meldrum, whose PhD student at the time, W. Morrish, was working on a spectroscopy technique known as Laser Absorption Spectroscopy (LAS). This technique is used for the detection and absolute concentration measurements of select gases, such as CH_4 and CO_2, as W. Morrish demonstrated in his recent PhD thesis [98]. Of importance though is that these measurements do not introduce any noise into the system and can be preformed at non-vacuum gas pressures. This section will detail the basics of this method and what sort of apparatus is needed to perform concentration measurements.

6.2.1 Basic Principles of LAS

The principle of Laser Absorption Spectroscopy (LAS) is centred around the identification of different types of gas molecules via the absorption of laser light. The structure of a given molecule, specifically its rovibrational modes (energy transitions involving both rotational and vibrational modes), result in a spectrum of absorption features unique to the specific gas [99, 100]. For example, CH_4 molecules feature a series of absorption features in the near-infrared (NIR) wavelength range as demonstrated in Figure 6.7 with the wavelength range of $\sim$1.6 μm to $\sim$1.7 μm.

If laser light is passed through a sample of gas, such as CH_4, the amount of laser light detected on the opposing side by a detector will be attenuated based upon the absorption strength of the gas at the given wavelength of laser light and the quantity of absorbent gas between the laser and detector [100, 102]. The quantity of gas is predominantly determined by the path length of the laser light and the concentration of the absorbent gas. The larger any of these three quantities are, the greater the attenuation in light will be observed. LAS looks to exploit this phenomenon by focusing on isolated absorption features to measure the level of attenuation of a given gas sample to identify the presence, and potentially the quantity of said gas.

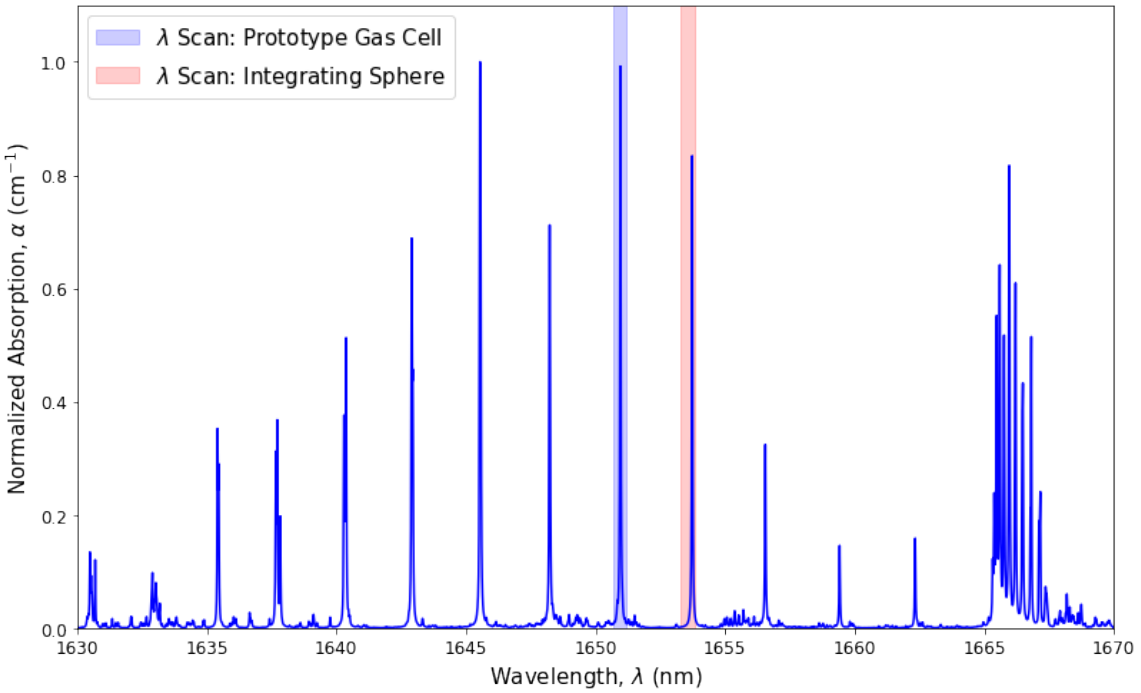

Figure 6.7: A sample of the NIR absorption spectrum of CH_4 between wavelengths of 1.63 μm and $\sim$1.67 μm normalized to the largest absorption peak value within the wavelength domain. Highlighted in blue and red are the wavelength scan regions corresponding to the prototype gas cell (Section 6.3) and integrating sphere (Section 6.4) respectively. Data used to generate this plot was taken from HITRAN 2020 data base [101].

One of the simplest forms of LAS, and the primary focus of this chapter, is Tunable Diode Laser Absorption Spectroscopy (TDLAS, of which we will refer to as just LAS for now on) [102]. In this technique, a gas cell of an experiment-specific geometry is placed between an IR laser and a corresponding photodetector (PD), as depicted in Figure 6.8.

The IR laser's drive current is modulated by a ramp signal, resulting in a ramp-like response in both the intensity of the laser output and the wavelength λ. For an appropriate choice of ramp signal, this results in a tight scan of wavelengths which can be tuned about a specific absorption feature for the gas of interest. As the laser light passes through the gas, the amount of absorption follows Beer's Law [98, 100]:

$$I = I_0 e^{-\alpha L c}, \tag{6.2}$$

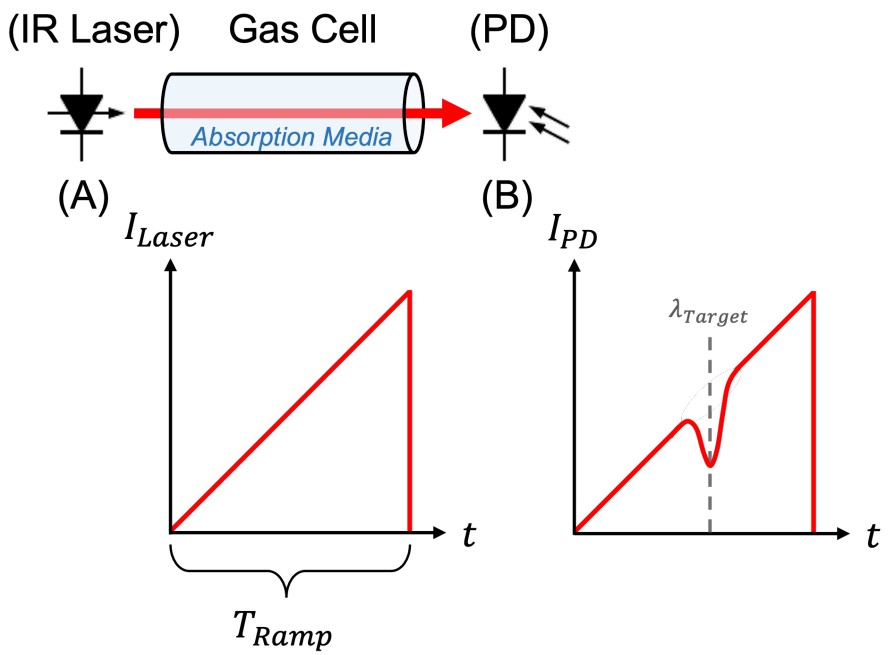

Figure 6.8: Basic principles of Tunable Diode Laser Absorption Spectroscopy (TDLAS) [103]. (A) The IR laser (laser diode, etc.) is modulated such that its optical intensity varies (I_{Laser} or I_0) like a ramp signal with period T_{Ramp}. The corresponding laser wavelength will also vary linearly, tuned such that the target absorption wavelength, λ_{Target}, is within the scan region. (B) Laser light passing through the gas cell will observe attenuation via Beer's Law (Equation 6.2) matching the absorption features of the absorption media. A photodetector (photo diode, etc.) will produce a ramp-like signal response with observed absorption peaks corresponding to the features of the target gas with heights corresponding to absorption, α.

where I and I_0 (interchangeable with I_{PD} and I_{Laser} in Figure 6.8) are the measured and initial laser intensity, α is the absorption coefficient (in cm^{-1}), L is the path length of the laser light (in cm), and c is the mole fraction of absorbent gas. What is then observed on the detector side of the gas cell is a ramp-like signal corresponding to the scan in laser intensity. This waveform will feature absorption peaks matching the absorption features of the gas in terms of both wavelength (location within the scan) and relative intensity.

For a given gas measurement, the primary control parameters are L and α. The smaller the value of c for the gas sample, the larger the path length that is required to observe an absorption signal, possibly also requiring the selection of a larger ab-

sorption feature. There are many different types of apparatus which are designed to maximize L such as integrating spheres (will be discussed further in Section 6.4) or multi-pass cells [100, 104].

6.3 Prototype LAS Gas Cell

During the initial conception phase, pre-dating the work presented in this thesis, the plan was to integrate a LAS system into an SPC itself. Using a prototype SPC, much like the 30 cm prototype at the University of Alberta (photographed in Figure 3.1 (c)), having the LAS system use the gas directly inside the detector as the absorbent medium would allow for the direct measurement of the fill gas. However, this would be a very invasive process and so it was deemed more sensible to pursue an external gas cell apparatus that would operate in circulation with an SPC to test the capabilities of the method. An external system poses logistical challenges in that it would require a continuous circulation with the SPC fill gas to perform measurements simultaneously with the SPC in operation, but at the very least for radon trap measurements the external system would be suitable.

A simple gas cell system made from a metallic pipe structure that would connect in circulation with the existing gas handling system at the University of Alberta (and later possibly with S140 at SNOLAB) was the initial prototype plan. Section 6.3.1 will discuss the current prototype design for this structure along with the complete testing apparatus for performing LAS measurements in circulation with the prototype 30 cm SPC and radon trap. We will also discuss data acquisition with the current apparatus, gas cell calibration, and measurement limitations and the next phase of this apparatus intended to directly address some of these concerns in assessing its suitability for use alongside S140 for CH_4-sensing.

6.3.1 Prototype Design

The current gas cell prototype design was built around the use of 1/2" stainless steel piping and pre-machined parts selected from Swagelok's available inventory. The key design specification was that the total gas column should length of at least ∼30 cm (the current prototype's gas column has a length of just under ∼42 cm), roughly the same as the inner diameter of the prototype SPC. This represents the minimum path length that a photon would need to travel for a fully SPC-integrated design. The intention here was that since a fully integrated design would be more logistically useful for live measurements of CH_4, using an external apparatus with a comparable path length would yield a better sense of the measurement capabilities of such an apparatus with up to 10% of CH_4.

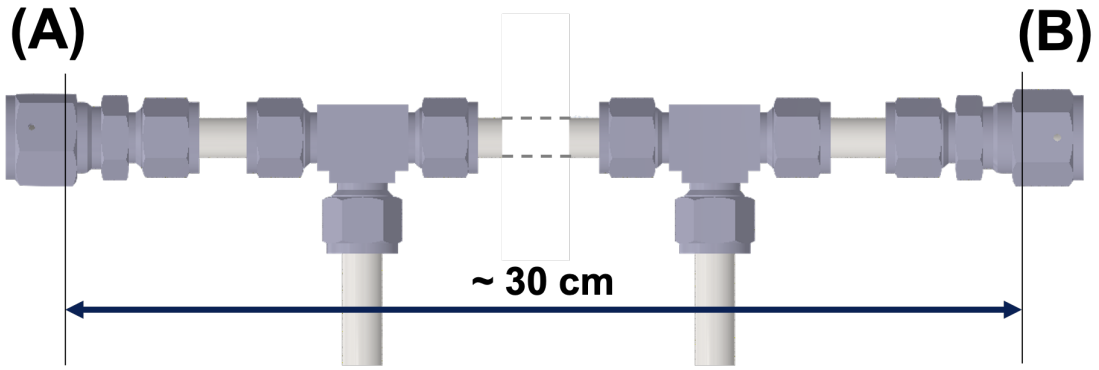

Figure 6.9: External CAD model of the ∼30 cm prototype LAS gas cell. Parts shown are assembled with existing Swagelok components and 1/2" stainless steel piping (the input/output pipes, in reality, are 1/4", just not in this CAD model). Side (A) represents the lens end cap, with side (B) containing the sapphire window. Internal views of the two end caps are provided in Figure 6.10. CAD model credit: Y. Ko.

The prototype was designed with help of Y. Ko and M. Baker, with a CAD model of the external setup presented in Figure 6.9. The design uses three segments of 1/2" stainless steel piping with two end caps (labelled (A) and (B)) and two tees to allow for the attachment of 1/4" piping to put the apparatus into circulation. The purpose of the end caps is to house the optical components necessary to pass IR laser light through the apparatus. An internal view of the end caps is provided in Figure 6.10.

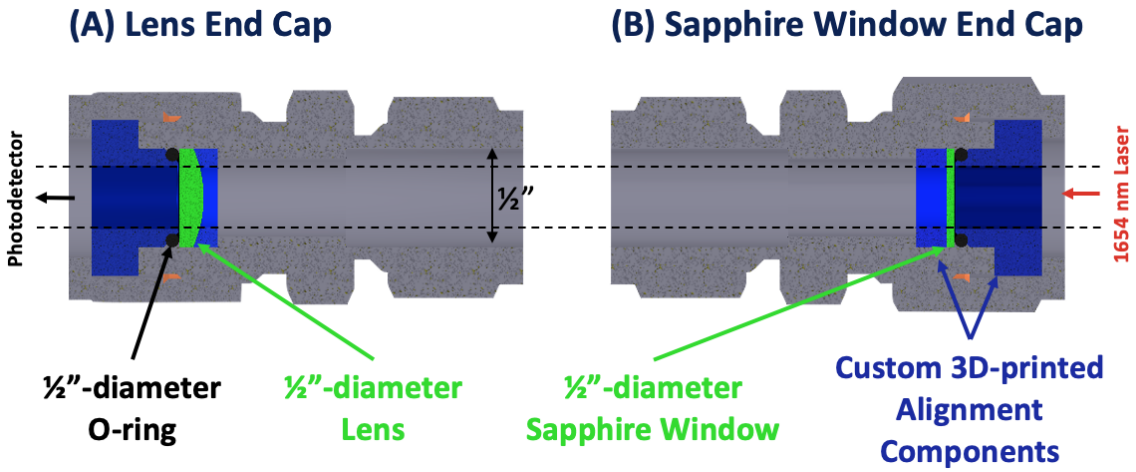

Figure 6.10: Cut-away views of the CAD models for the two gas cell end caps. (A) Houses a lens while (B) contains an optical sapphire window (both 1/2" in diameter). Custom 3-D printed PLA plastic parts plus 1/2" silicon o-rings are used to seal each end cap to prevent gas leaks. Dimensions of the 3-D printed spacers and plugs, plus custom-machined Swagelok components are provided in Appendix C. CAD model credit: Y. Ko.

End cap (A) houses a 1/2" diameter convex lens which is used to help focus laser light onto an external photodetector. End cap (B) contains an Edmund Optics 12.7 mm (∼1/2") diameter, 1 mm thick optical sapphire window for allowing the transmittance of IR laser light into the gas cell. To ensure that the end caps were leak-tight, the optical components were embedded into custom-modified 1/2"-Swagelok to 1/2"-VCR connectors with the VCR ends having a slightly greater than 1/2" diameter (∼0.504"), ∼0.403" deep counterbored hole. Inside the counterbore, four layers of components were inserted: a custom 3-D printed PLA plastic spacer; optical component; 1/2" diameter silicon o-ring; and lastly a custom 3-D printed PLA plastic plug. All components, apart from the optical pieces, have a central hole to allow for the passage of laser light. The specific dimensions of the custom-modified Swagelok-VCR connectors and 3-D printed parts are given in Appendix C. To compress the internal parts, primarily the o-rings to seal each end cap, a female 1/2" VCR nut was tightened to both ends; this cap also has a (pre-machined) central hole. Under vacuum, this design was able to sustain pressures as low as 8.7x10^{-5} Torr and successfully

passed leak checks using an Agilent HLD MD15 helium leak detector.

6.3.2 LAS Test Apparatus

With the gas cell in place, the remaining components required for the LAS apparatus were the IR laser, photodetector (PD), and a device for modulating the laser's wavelength and recording measurement signal on the PD. The overall look of the complete apparatus is presented in the diagram in Figure 6.11. A view of the physical apparatus as assembled onto an imperial (1" hole-spacing) optics bench in the Piro Lab is presented in Figure 6.12 with a top-down view of the gas cell (a) and an overview of the entire setup with electronics (b).

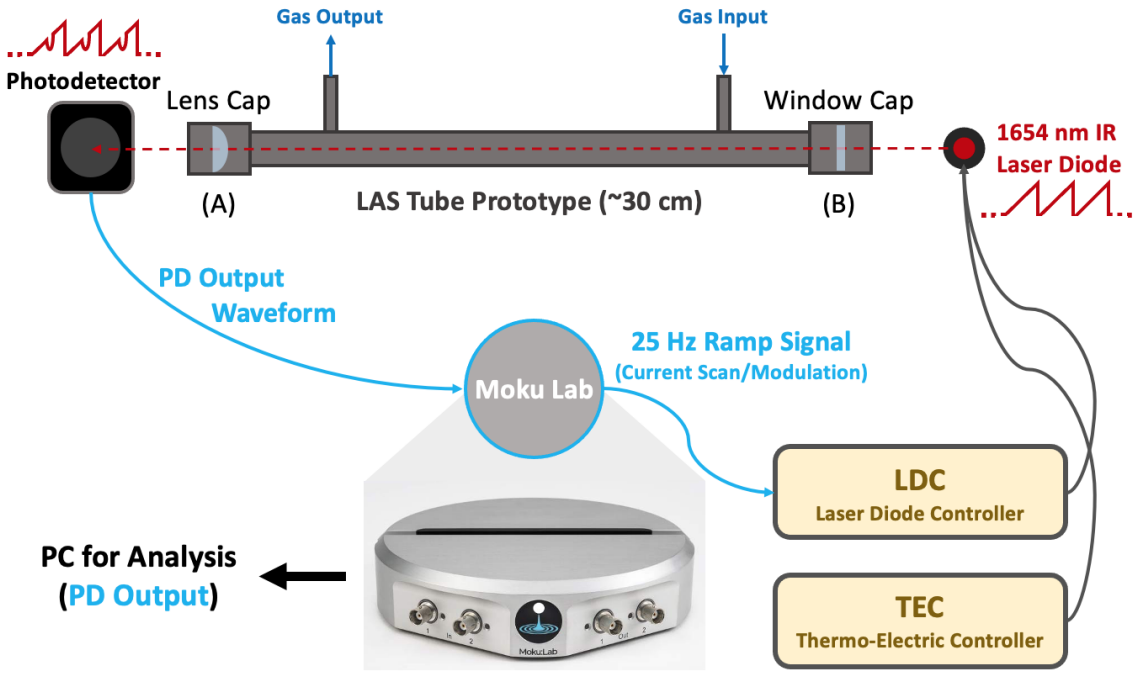

Figure 6.11: Simplified schematic of the prototype gas cell apparatus for performing test LAS measurements for concentrations of CH_4. This basic setup can be placed in circulation with additional hardware such as the radon trap (see Figure 6.17).

IR Laser Diode

The specific infrared absorption wavelengths for CH_4 that we decided to target were in the ~1650 nm range (see Figure 6.7). We acquired a nominally 1654 nm diode

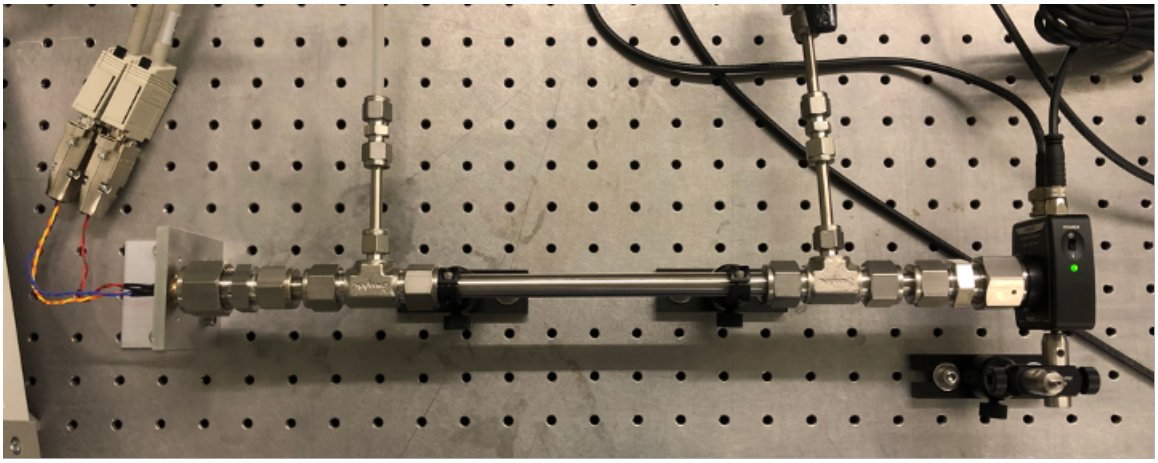

(a)

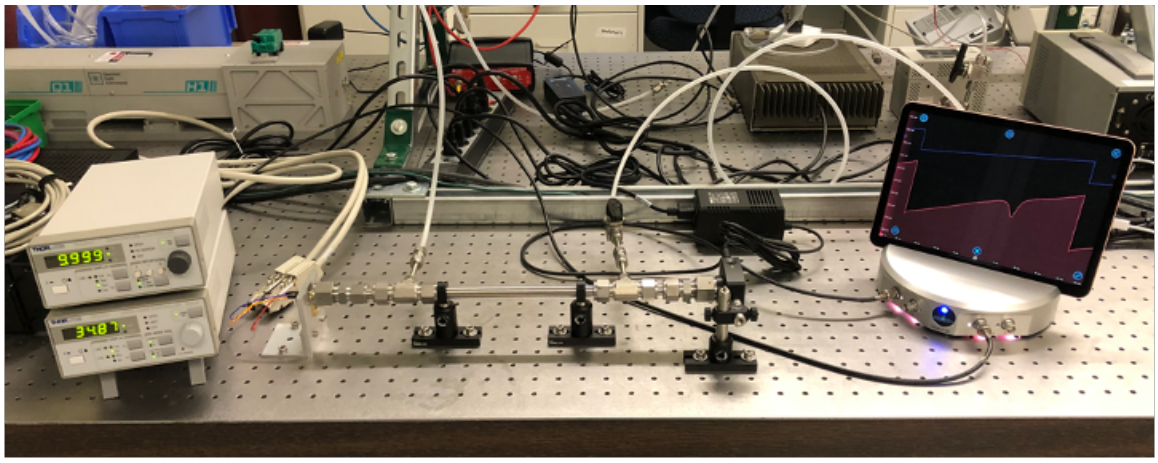

(b)

Figure 6.12: Laser absorption spectroscopy test setup with the prototype ∼42 cm gas cell at the Piro Lab at the University of Alberta. (a) Top-down view highlighting the gas cell, mounted Norcada 1654 nm laser, and PD. (b) Full view including TEC and LDC (left side) and Moku:Lab plus iPad app running the "Moku:" app (right).

laser produced by Norcada - specifically a model NL1654-T tunable IR distributed-feedback (DFB) laser. The purchased laser is assembled in Norcada's "T-type" TO-39 packaging which is an 8-pinned 9.09 mm diameter cylindrical model with a lasing cavity opening that is 6 mm in diameter. The one drawback with this laser model is that it is non-collimated, the consequences of which will be discussed later in Section 6.3.5. The laser is mounted to a Norcada TO-39 mounting plate - a 76 x 63 x 6 mm 6061 aluminum block acting as the laser's heat-sink. A custom L-bracket was

machined to bolt the mounting plate to the optics bench as seen on the left of Figure 6.12 (a).

A set of controllers were purchased to power and operate the diode laser: a Thorlabs 12 W TED200C thermo-electric cooler (TEC) and a Thorlabs ±500 mA LDC205C laser diode controller (LDC) (both pictured in Figure 6.12 (b) on the left). Both controllers were wired to the laser diode using provided cables and custom-wired 9-pin D-Sub crimp connectors according to the wiring diagram provided in Figure 6.13. Table 6.1 provides further detail on the pin labelling.

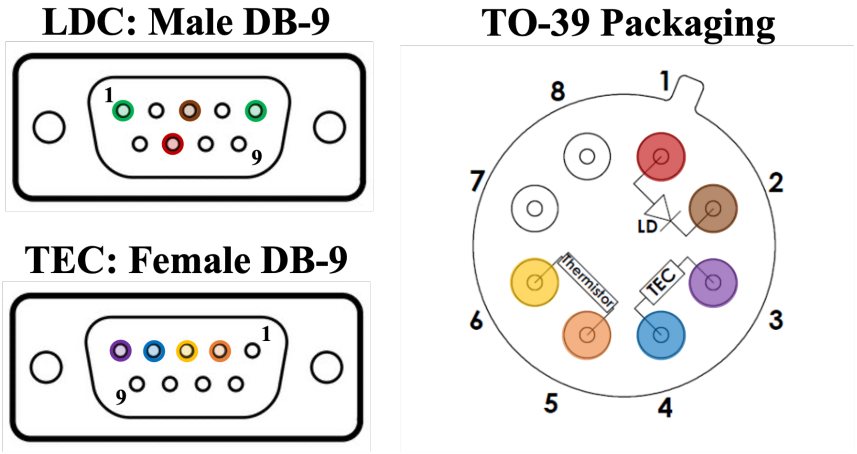

Figure 6.13: Pin diagram for wiring the Norcada TO-39 diode laser packaging to DB-9 connectors for the LDC and TEC controllers [105]. Note how LDC pin 1 (interlock control) and pin 5 (interlock ground) are shorted, bypassing the LDC's laser interlock controller. Pin diagram modified with permission from Norcada Inc.

The purpose of the TEC is to maintain the laser's internal temperature according to Norcada's operating specifications by maintaining the current of the diode laser's thermo-electric cooler. This unit will maintain a constant temperature according to a set thermistor resistance that measures the laser temperature. The Norcada specifications for the thermistor resistance are 10.0 ± 0.1 kΩ, corresponding to a 25°C laser temperature. The LDC unit provides the laser's drive current allowing it to lase and emit photons. The wavelength response versus drive current for the specific NL1654-T DFB laser model is provided in Figure 6.14.

Table 6.1: Further pin description for the pin and wiring diagram in Figure 6.13 [105].

TO-39 Pin #	TO-39 Label	LDC/TEC Pin #	LDC/TEC Label
1	LD Anode (+)	LDC 7	LD Cathode (-)
2	LD Cathode (-)	LDC 3	LD Ground
3	TEC (-)	TEC 5	TEC (-)
4	TEC (+)	TEC 4	TEC (+)
5	Thermistor (+)	TEC 2	Thermistor (+)
6	Thermistor (-)	TEC 3	Thermistor (-)
7	Not Used	N/A	N/A
8	Not Used	N/A	N/A

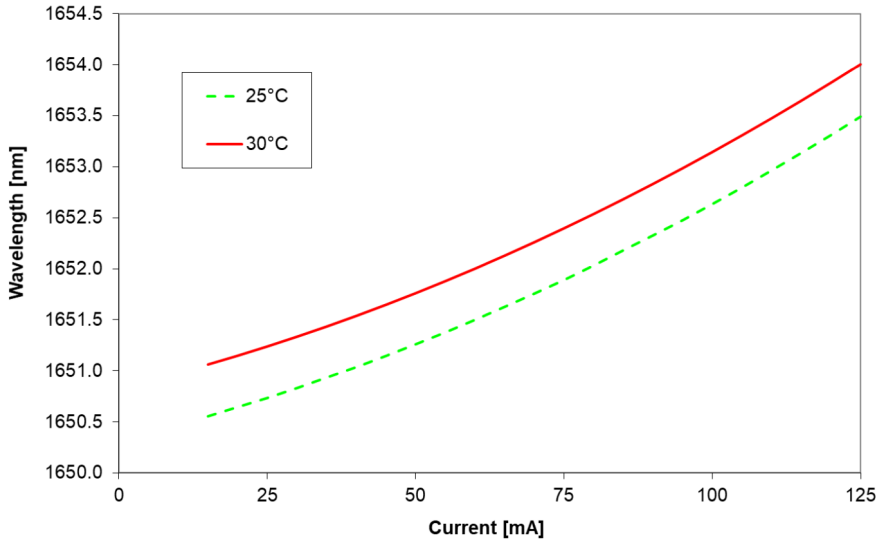

Figure 6.14: Norcada model NL1654-T DFB laser diode wavelength response as a function of LDC drive current for 25°C (red) and 30°C (green-dashed) [105]. For this thesis, the 25°C response curve will be referenced to since this is the laser's response for a thermistor resistance of 10.0 ± 0.1 kΩ. Reproduced with permission from Norcada Inc.

Photodetector and Moku:Lab

At the opposite end of the gas cell (located at end cap (A) in Figures 6.10 and 6.11) is where the PD is located. For our test apparatus, we made use of a Thorlabs

PDA10D2 InGaAs fixed gain amplified detector rated for 900 nm to 2600 nm wavelength detection (see right side of Figure 6.12 (a)). The one downside to this model is the large observable ∼230 mV baseline signal. It is unclear if this is an inherent property of the particular PD model ('dark current' rate), or if it could be another electronic issue. For the time being, as observed in this setup, so long as the target signal is at an amplitude well above this background PD response then the baseline signal can be ignored. Future iterations of this setup, however, will look to improve this baseline offset.

For recording data from the PD and additionally providing a modulating ramp signal to the LDC to perform wavelength scans, a device called a "Moku:Lab" (often shortened to "Moku") produced by Liquid Instruments was used (see right side of Figure 6.12 (b)). The Moku is an FPGA multi-purpose electronic device that serves the necessary functions for this setup as both a simultaneous function generator and oscilloscope. Using the 'Oscilloscope' instrument [106], BNC cables can be used to connect one of the Moku's input channels to monitor the PD response while one of the Moku outputs is connected to the modulation port on the LDC. The oscilloscope output can be accessed and recorded remotely via a PC using the python library 'pymoku' [107]. Alternatively, an iPad (see right side of Figure 6.12 (b)) can be used with the "Moku:" app to control and view the oscilloscope output.

6.3.3 Data Acquisition and Analysis

For performing test measurements, the 1654 nm diode laser was set to a nominal 25°C internal temperature by setting the TEC thermistor resistance to the specified 10.0 kΩ (±0.1 kΩ). After tuning the signal response to avoid the PD dark current and clearly display an isolated absorption feature corresponding to CH_4, as observed using the iPad's Moku app, a central LDC drive current ($I_{LD\,Set}$) of 34.00 mA (±0.05 mA) was selected. The LDC response was modulated via the Moku's output by a 25 Hz (arbitrary frequency, set to match modulating waveform settings used by W.

Morrish [98]) 200 mV peak-to-peak rising ramp signal. The LDC response, I_{LD}, to a modulating potential is given by:

$$I_{LD} = I_{LD\,Set} + K_{Mod}U_{Mod}, \text{ where } K_{Mod} = \frac{I_{LD\,Max}}{10\text{V}}\ (\pm 5\%). \tag{6.3}$$

K_{Mod} is the modulation voltage scaling where $I_{LD\,Max}$ is the maximum current output of the LDC. In the case of the LDC205C, $I_{LD\,Max}$ is 500 mA, making $K_{Mod} = 50.0 \pm 2.5$ mA/V. U_{Mod} is then the modulation potential that spans ±200 mV. Therefore, including the 5% uncertainty on K_{Mod}, the LDC current scan ranges from 24.0 ± 0.5 mA to 44.0 ± 0.5 mA. Using the 25°C wavelength response curve in Figure 6.14, we can estimate the wavelength scan to be from ∼1650.7 nm to ∼1651.2 nm - an approximate 0.5 nm scan. According to Figure 6.7, this aligns with the largest absorption peak at ∼1650.96 nm, but an IR spectrometry analysis of the observed laser light at the exit of the gas cell still needs to be performed to verify this.

Under these ramp modulation and LDC drive current conditions, example PD responses are presented in Figure 6.15. On the left we have an example non-absorbent spectrum where pure Ar gas at atmospheric pressure was inside of the gas cell. The right waveform illustrates the ∼1650.96 nm absorption peak resulting from an Ar + 3% (±10%) CH_4 fill gas mixture at atmospheric pressure. Both waveforms display slightly over one period ($T = 40$ ms) of data recorded at 246 kS/s (246x10^3 samples per second) with a 20 ms offset centred about the trigger point. Each waveform has undergone a 5x sample averaging, as set directly on the Moku, to reduce visible high-frequency fluctuations.

Absorption Peak Cuts

With the hypothesized ∼1651 nm peak identified and electronics settings in place, the next phase of data acquisition requires isolating the absorption peak from the background, non-absorbent, PD response waveform. In practice, this can be quite tricky with the current test apparatus, but the ideal steps will be presented here based

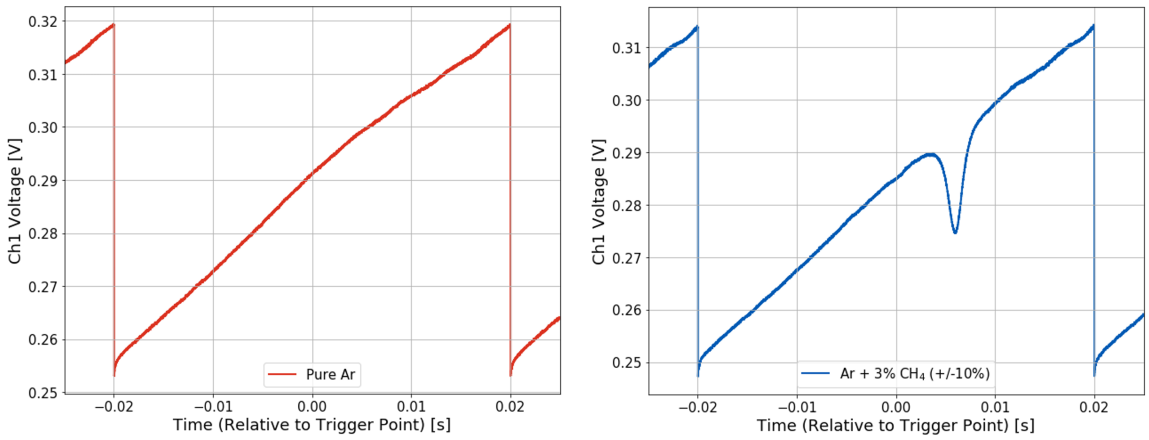

Figure 6.15: Sample waveforms of slightly over one period (40 ms) for an LDC drive current of 34.00 ± 0.05 mA and a ±200 mV 25 Hz ramp modulation signal. (Left) PD response for pure Ar gas at lab pressure. (Right) PD response for a nominal mixture of Ar + 3% (±10%) CH_4 at lab pressure, displaying a single absorption peak estimated to correspond to ∼1651 nm.

upon the method laid out by W. Morrish [98]. For a given measurement, ideally one is able to simultaneously measure both the absorbent and non-absorbent spectrum. This will yield two waveforms, akin to what we see in Figure 6.15, but ensuring that there is no global time separation between each measurement recording. In principle, the information contained in the background, non-absorbent waveform can allow for the full corrective removal of the PD's ramp-signal response and underlying non-CH_4-related absorption features.

Following Figure 6.16, we perform at least two corrections using a two-step regression-based process. Prior to these corrections, we also trim the data to a single period domain of 40 ms and use the voltage difference at the bottom of the discontinuity (located at the start of the window) to correct for any offset between background and absorption waveforms.

1. **Linear Ramp Correction:** First, we fit the background ramp-like PD response to a line. The exact domain may vary depending upon the PD response, but generally features towards the discontinuity at either end of the waveform are to be avoided. In this case, we perform a linear fit to the domain [-18 ms,

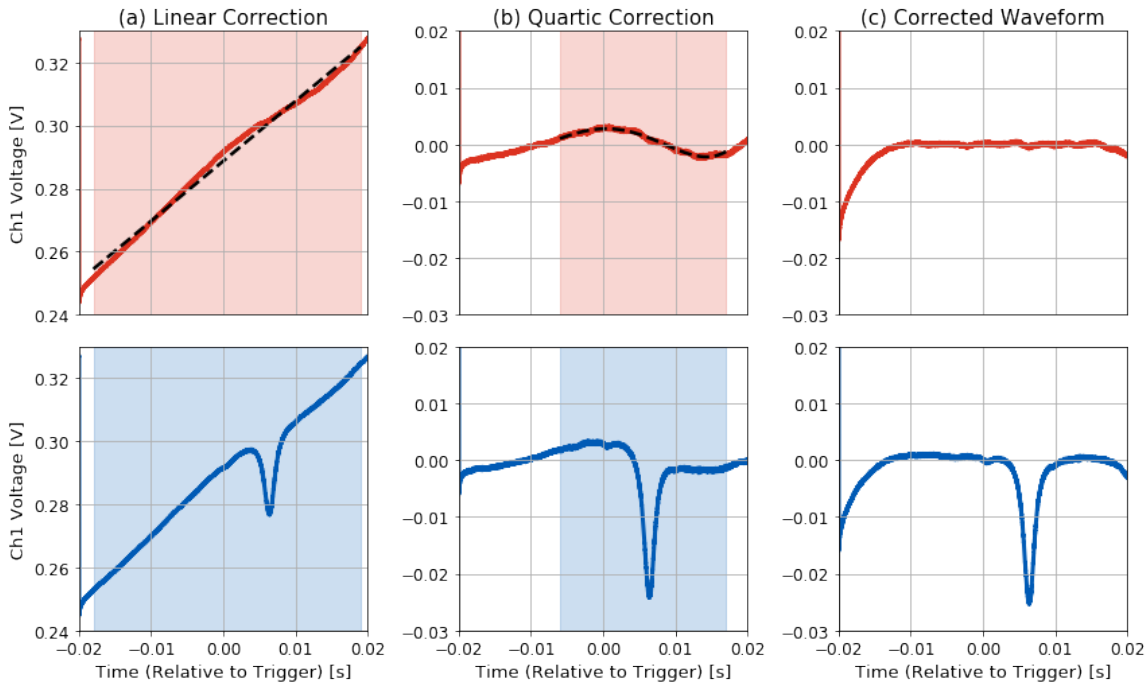

Figure 6.16: Base cleaning cut steps for removing the PD's background waveform response locally about the absorption peak. The upper row of plots (in red) were recorded using pure Ar at lab pressure, where as the lower row (in blue) were recorded using Ar + 3% CH_4 ($\pm$10%) at lab pressure. Steps include a linear ramp correction (left), polynomial (e.g., quartic in this case) correction (centre), and a presentation of the final waveform pre-sampling (right). The shaded regions highlight the domain that was used for fitting the background spectrum.

19 ms] relative to the trigger point centred about the window. A sample PD response waveform for pure Ar (top-left, in red) and Ar + 3% ($\pm$10%) CH_4 (bottom-left, in blue) at lab pressure are shown in Figure 6.16. In the top-left plot, the linear regression for the background waveform is highlighted. Once this cut is applied to both waveforms, the resulting linearly corrected waveforms are displayed in the centre column of Figure 6.16.

2. **Polynomial Correction(s):** Once the general ramp-like response is corrected for, the typical remaining background signal is polynomial in nature. Again, the exact response will vary, but in this case, a quartic (a 4^{th} order polynomial) was the lowest order of polynomial which matched the curvature of the background waveform within the vicinity of the absorption peak. This selected domain was

[-6 ms, 17 ms]. The overlaid quartic regression is displayed in the top-centre plot of Figure 6.16. Once this second correction is applied, the right column waveforms display the fully corrected background and absorption waveforms.

With these two corrections applied, within the domain directly about the absorption peak (the only feature of interest for analyses) we ideally observe a 0 V response save for where true absorption features exist. For the background spectrum, this would appear as the complete removal of any PD response with a flat 0 V signal. Additional smoothing may be performed after these steps, typically on the order of 10-30 points, averaging reduces significant high-frequency fluctuations beyond what the Moku was able to remove during the initial measurements.

Assuming that both waveforms were recorded simultaneously, these steps should cleanly isolate the absorption peak within the uncertainty of baseline fluctuations and the smoothing method. However, there are several observed factors that can limit the efficacy of this method, particularly for when measurements of the background PD response and absorption waveforms have to be recorded independently. These factors include:

- **Electronic EMFs**

  EMFs inducing changes in the current response of the LDC due to the movement of power cables for the PD, Moku:Lab, etc. can shift the value of $I_{LD\,Set}$. This changes the wavelength scan region of the diode laser, resulting in an approximate horizontal offset between the two measurement waveforms. The LDC's set current is controlled by an adjustable, but is highly sensitive dial. Re-correcting $I_{LD\,Set}$ between measurements in the event of external EMFs is consequently unreliable.

- **Time-dependent PD Response**

  As with most electronic equipment, there is normally a time-dependent "warm-up" period for equipment to reach a state of operational equilibrium. Before

this phase, there will be a time-dependent offset to the given piece of equipment's measurements. A good example of this is with the PDA10D2 InGaAs photodetector, which has a slowly-rising offset response for, observationally, on the order of ~ 1 hour after being powered on. In terms of LAS measurements, this manifests as a baseline offset between time-independent measurements.

- **Background Measurement Time-offset**

  The underpinning issue between time-independent background and absorbent waveform measurements is that the background PD response behaviour is time-dependent and can manifest in ways that simple linear corrections (e.g., a baseline offset correction) cannot address. For example, the slope of the ramp-like PD background response can change over time, ruining the effectiveness of correction steps as outlined in this section. For using the LAS system in live-monitoring applications, or even for measurements spanning hours, a single background waveform will not be apply to every waveform measured afterword during a continuous live measurement session.

Attempts have been made to try and perform the two regression corrections without the need for a simultaneous (or near-simultaneous) background waveform by performing the regressions on the absorption data directly. This essentially repeats the process outlined previously, but ignores the domain directly about the absorption peak (currently selected as [3 ms, 12 ms] relative to the trigger point) when performing each regression calculation. However, the loss of information near the absorption peak often leads to underestimated corrections resulting in oversized absorption peaks, particularly when the absorption peaks are large in terms of both width and amplitude. For the following section on LAS calibration, we made use of these corrections and did not record background waveforms solely for showcasing the methodology. However, for further tests leading into the next phase of the apparatus design, as discussed in Section 6.3.5, we will need to improve the reliability of these

corrections by enabling simultaneous background measurements or introduce new, alternative analysis techniques.

6.3.4 Gas Cell Calibration

For performing measurements of varying CH_4 concentrations, the gas cell apparatus must be calibrated to associate each absorption peak with a set of gas conditions. The specific metric that we use for calibrating is the absolute value of the integral of the absorption peak, recorded as a sum over all (smoothed) points in the domain [2.0 ms, 10.5 ms] (to be tuned as analysis methods advance). The principal concerns while calibrating are the concentration of CH_4, which must be non-zero to observe any absorption peak whatsoever and the pressure of the gas. Varying gas pressure has a known "pressure broadening" effect which can widen the resolution of the absorption peak notably at higher pressures and low temperatures [108]. Other factors can modify the absorption features of the gas, including the gas temperature and even its kinematics via "Doppler broadening" for sufficiently low-pressure gases, but such secondary effects were not observed during the pressure scales used during our test measurements. Even with the operation of a 6 V ALLDOO CMP25W micro pump, there were never any significant measurable changes in absorption peak characteristics whether the gas was in stasis or flowing in circulation.

Since there are limitations in the capacity to perform proper background-subtraction corrections, as described in the previous section, non-background cut methods were employed to perform test calibration measurements for pressure and CH_4 concentration. These calibration measurements were performed with available equipment at the Piro Lab and can be greatly improved upon, as discussed in the following section. However, for a suitable range of pressures and CH_4 concentrations (e.g., the regimes used for S140 at SNOLAB), calibration curves need to be measured for the practical use of the specific equipment. For our test measurements, the calibration setup is presented in Figure 6.17's P&ID diagram.

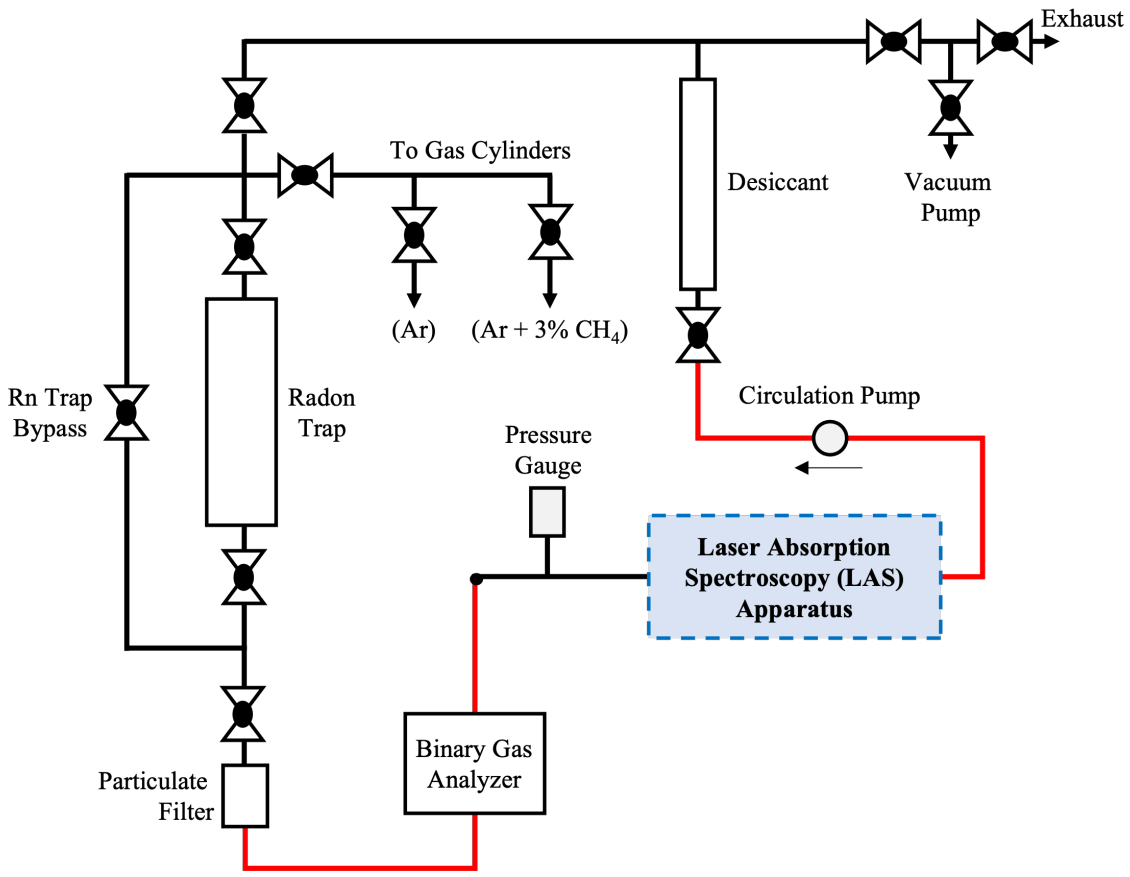

Figure 6.17: P&ID diagram of the first test LAS calibration setup in the Piro Lab (modified based upon Figure 6.3) for performing LAS measurements with either the prototype gas cell or test integrating sphere apparatuses (shown respectively in Figures 6.12 and 6.23).

For measuring pressures, we used a calibrated Swagelok S model NA25 piezoresistive absolute pressure transducer rated for up to 25 psi with a 0.01 psi precision ($\leq$0.5% accuracy). CH_4 concentrations were measured using an SRS BGA244 Binary Gas Analyzer (BGA) for relative concentration measurements when mixed with Ar. Ideally, pre-mixed gas bottles or the use of a gas-mixing board would be preferred to the BGA due to observed systematic errors in the respective equipment's concentration measurements, but arbitrary gas dilution of pure Ar and Ar + 3% CH_4 ($\pm$ 10%) had to be performed instead. For each calibration curve, data were recorded bidirectionally in the case of measurement hysteresis.

For pressure calibrating, 5 bidirectional waveforms were recorded using the nom-

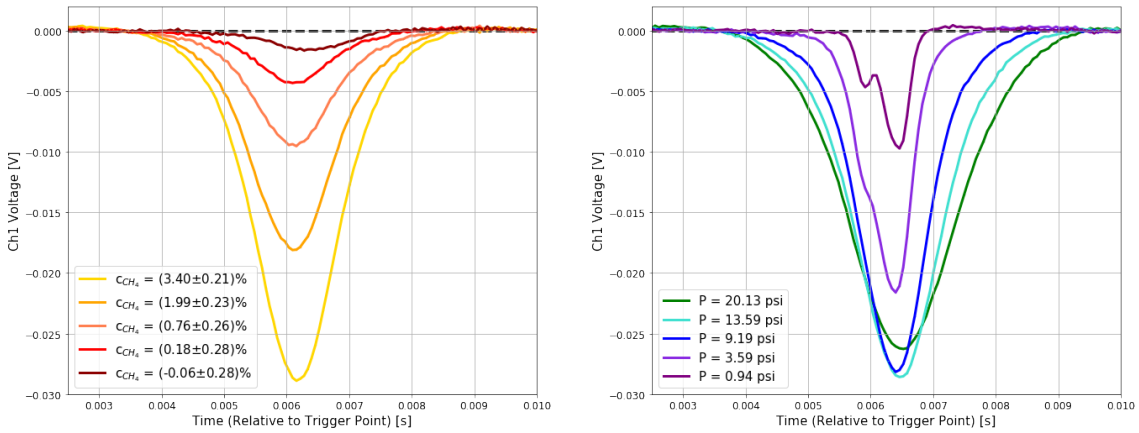

(a) (b)

Figure 6.18: Example LAS waveforms of varying CH_4 concentrations (a) and gas cell pressure (b).

inal Ar + 3% CH_4 (± 10%) pre-mixed gas. A selection of these pressure-varying background-subtracted waveforms, noting that corrections were performed without reference waveforms, is provided in Figure 6.18 (b). Note that the larger the absorption peak, the larger the systematic overestimation of the peak's size in this current cleaning cut regimen.

For each measurement, the pressure uncertainty was assumed to be ±0.01 psi (the largest observed fluctuations in pressure reading). The absolute integrated area of each background-corrected waveform versus pressure calibration curve is presented in Figure 6.19.

The grey vertical bar highlights the pressure ranges that the CH_4 calibration curve was recorded over: from 13.52 psi to 13.58 psi. The characteristic shape of the pressure calibration illustrates similar behaviour to a root or logarithmic function. Above a certain pressure, the shape of the absorption peak primarily grows in terms of its width, rather than height. Two independent square root regressions are overlaid on the calibration plot to guide the eye, but in reality, interpolation would be used between each point in the absence of a theoretically-motivated analytical function. This behaviour is also subject to change as improved calibration methods are explored.

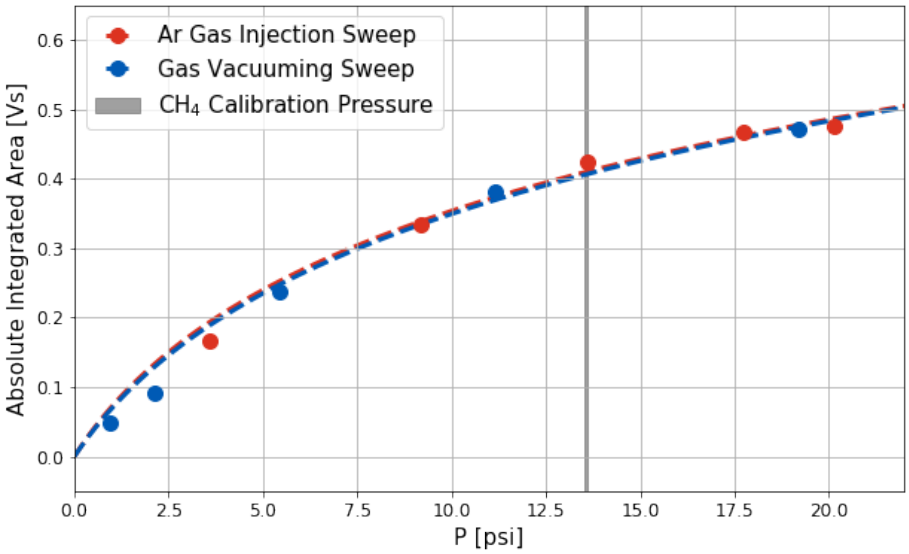

Figure 6.19: Pressure calibration curve for the gas cell within the regime 1e-2 psi to 25 psi. All points were recorded using Ar + 3% CH_4 ($\pm$ 10%) gas.

For CH_4 concentration calibration, points were recorded at lab pressure within the aforementioned range of 13.52 psi to 13.58 psi. Again, 5 bidirectional data points were recorded where for each sweep either pure Ar or the Ar + 3% CH_4 ($\pm$ 10%) mixture was started with, using the other to slowly increase/decrease the concentration of CH_4. To reduce hysteresis and other systematics imposed by the BGA, the circulation pump was ran for at least 20 minutes per measurement, with an additional wait period of 10 minutes once the pump was turned off. Sample waveforms are presented in Figure 6.18 (a).

The resulting calibration curve is presented in Figure 6.20. In this case, both bidirectional data sets display linear behaviours. The grey region highlights the (3.0 $\pm$ 0.3)% region where the pressure calibration curve was recorded.

In practice, the two bidirectional calibration curves for both calibration types would set the upper and lower uncertainty bound on the total calibration measurement. For a given absorption waveform recording, one will be required to know the gas pressure. Using the two interpolation curves of data points in Figure 6.19, one can determine $A_{P\,Cal} \pm \delta A_{P\,Cal}$, the integrated area associated with the known pressure. Likewise,

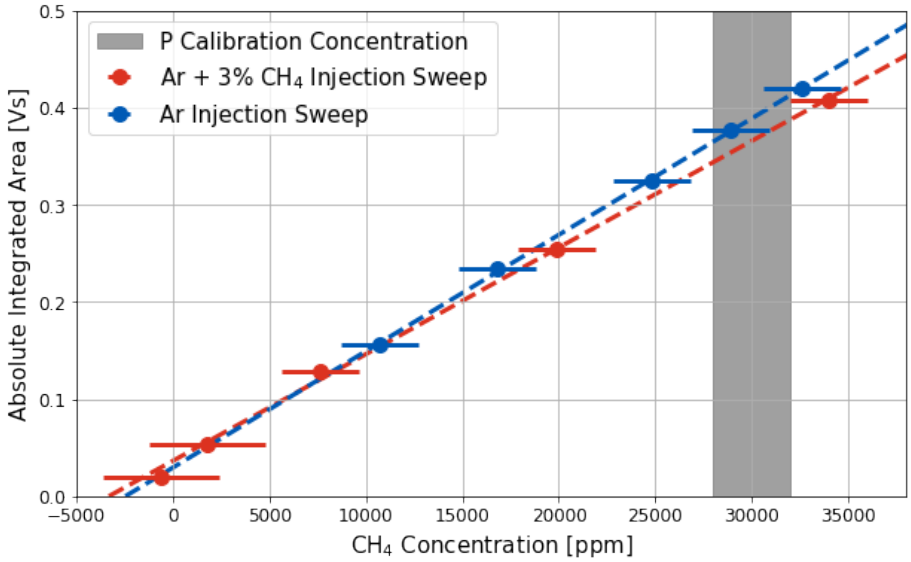

Figure 6.20: CH_4 calibration curve for the gas cell within the regime 0.0% to (3.0 ± 0.3)%. All points were recorded at the given lab pressure: (13.52 psi, 13.58 psi).

the reference integrated area, $A_{P\,Ref} \pm \delta A_{P\,Ref}$, is already known as defined by the intersection between the interpolations and the grey vertical bar. The ratio of $A_{P\,Ref}$ to $A_{P\,Cal}$ (plus uncertainty from error propagation) acts as a scaling factor for the CH_4 calibration curve. Moving on to Figure 6.20, one can use their true measured integrated area, $A_{Meas} \pm \delta A_{Meas}$, to map to the corresponding CH_4 concentration (and uncertainty) using the interpolation curves scaled by the aforementioned scaling factor.

The efficacy of this method is dependent upon the reliability of the background subtraction cuts and calibration apparatus, plus the minimization of systematics during calibration. Importantly, it is also the assumption that within the target pressure and CH_4 concentration regimes the behaviour of both calibration curves is identical. In practice, calibration curves should be performed for several fixed pressures and CH_4 concentrations to verify the use of the linear scaling factor discussed prior.

6.3.5 Planned Iterations and Remaining Work

For the gas cell system to be used for reliably measuring absolute CH_4 concentration measurements, let alone perform as a live-monitoring system, some improvements need to be put in place and will be the focus of the next phase of this project.

The two primary issues with the current gas cell apparatus include the inability to simultaneously measure background, non-absorbent waveforms alongside absorbent waveforms with CH_4 present, and the poor collimation of the 1654 nm laser light. Firstly, the beam angle of the laser diode was approximated with an IR viewing card to be on the order of 45°. This means, the majority of photons are not passing straight through the gas cell but are angled such that they will interact with the inner structure of the stainless steel tube and alignment components. This can lead to hypothesized non-physical reflection absorption peaks (Figure 6.21 (a)) and complex background absorbance and or reflectance features (Figure 6.21 (b)).

The solution to the poor beam collimation and improving the behaviour of the background waveforms is by making use of collimating lenses. This can be combined with a potential solution to the first raised issue of non-simultaneous background measurements: by fibre-coupling the laser to two independent, yet identically structured gas cells. By using a second gas cell filled with a non-absorbent gas (of arbitrary pressure), one can theoretically measure both the waveforms at the same time. The concept is presented schematically in Figure 6.22.

Both cells would require light from the same laser, so a split fibre would need to be used to feed the 1654 nm laser's output into both cells. With the current laser model, this would require a new collimating structure into the fibre input and output collimating lenses rated for 1654 nm. Alternatively, Norcada does provide "B-Type" laser packages which are pre-built with a laser fibre-port that could be used instead.

Alternatively, or in addition to apparatus improvements, there are possible signal analysis improvements that could be made to better and more consistently isolate

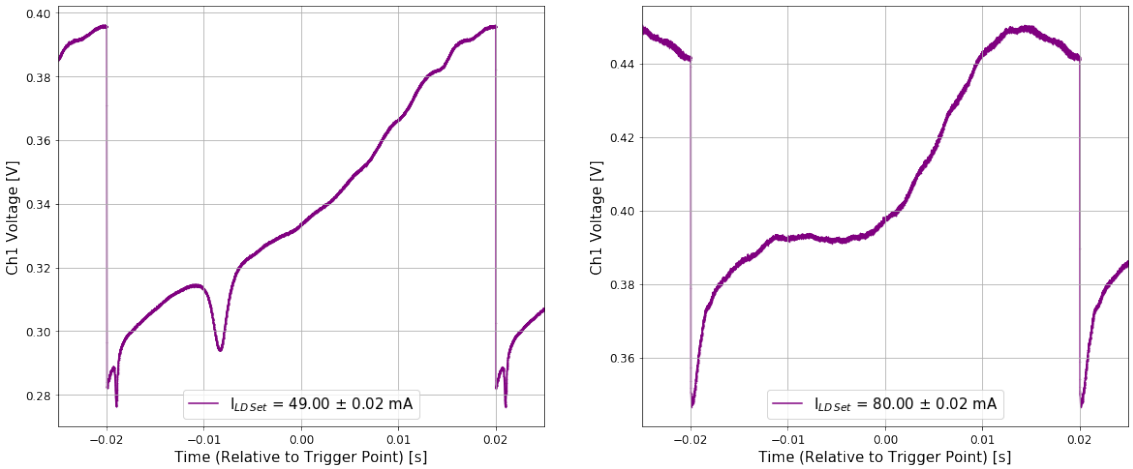

(a) (b)

Figure 6.21: Example PD response waveforms of extreme backgrounds of unknown origin. (a) Setting $I_{LD\,Set}$ to 49.00 ± 0.02 mA, the non-linearity of the PD ramp response becomes further exaggerated, but early in the scan window, a second, non-physical absorption peak appears. This peak shifts independently of the true absorption peak. It is hypothesized that this waveform may be due to internal reflections within the gas cell. (b) Setting $I_{LD\,Set}$ to 80.00 ± 0.02 mA, the PD's ramp response becomes extremely non-linear. It is unknown what causes this effect; possibly it is either due to absorptive or reflective properties of the gas cell materials.

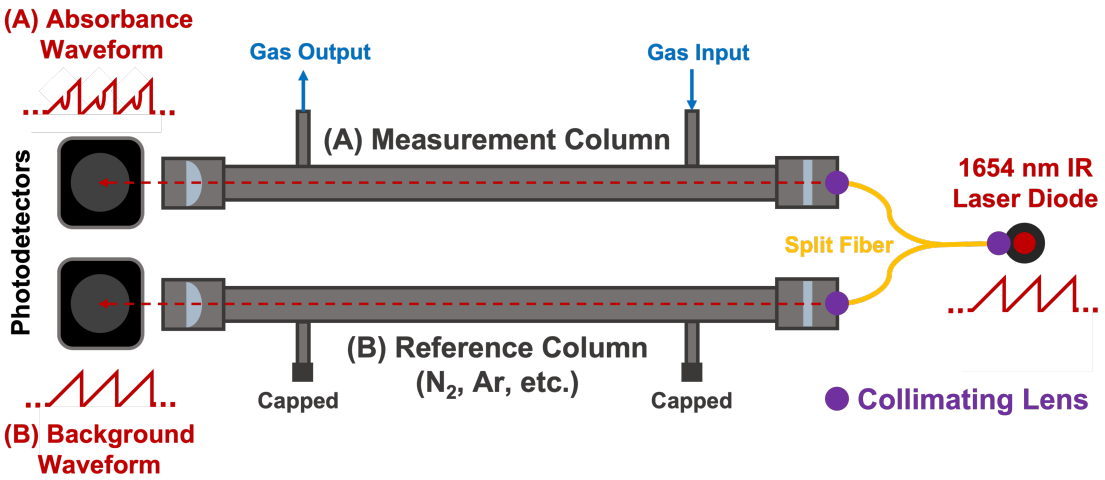

Figure 6.22: Concept extension of the test gas cell LAS apparatus in Figure 6.8 (electronics implied). Expanding to two gas cells, one with an isolated non-absorbent gas, would allow for the simultaneous measurement of the absorbance and background waveforms. The 1654 nm diode laser would need to be fibre-coupled to the gas cells, requiring further collimating lenses.

measured absorption peaks. One such option is to make use of improved fitting algorithms. A possible option that will be explored is known as Asymmetric Least Squares Smoothing (ALS) [109], or an alternative smoothing algorithm designed for background subtraction applications. Improvements to the data collection process, such as increased time-averaging, could also improve the overall data quality of measured waveforms. Such improvements could deem the need for an improved apparatus unnecessary and will be the first options tested during the next phase of this project prior to any major design overhauls.

Despite this next phase, the long-term goal of this project is to make use of this apparatus with S140 at SNOLAB. Before commissioning underground, the apparatus needs to be tested and undergo calibration for the relevant gas mixtures and pressures of Ne + CH_4. As a compliment to this prototype, we have also been exploring the possibility of an alternative apparatus: an integrating sphere, as discussed in the following section.

6.4 Prototype Integrating Sphere

At the Meldrum Lab at the University of Alberta, studies of LAS performed by W. Morrish made use of integrating sphere devices [98, 110]. An integrating sphere is a spherical gas cavity with a highly-reflective, often diffuse inner coating with small holes for a laser feed-through input and output port for a PD. The principle idea of an integrating sphere is that incident light will be reflected about the sphere a significant number of times before exiting via the PD port. Therefore, for even a small apparatus, high average path lengths may be achieved. For example, with simulations performed by W. Morrish, one of their integrating spheres, with an inner diameter of 38.1 mm and a pre-sandblasted, 99.5% reflective gold inner coating, was estimated to attain an average path length of 2.442 $\pm$ 0.006 m [98].

The advantage of an integrating sphere when compared to a typical gas cell is often this greater average path length, reducing the lower concentration measurement limit.

However, for concentrations on the order of 10% CH_4, smaller path lengths may still be favourable due to less overall absorption. Integrating spheres alternatively also remove the need to worry about laser beam collimation and, for appropriate inner surface coatings (e.g., elemental gold), can exhibit improved linearity in photodetector background response waveforms.

6.4.1 Integrating Sphere Test Apparatus

For testing purposes, we were allowed to borrow the most recent model integrating sphere from the Meldrum Lab for comparative performance tests using the same prototype gas cell calibration setup discussed previously. Photographed in Figure 6.23, is the 38.1 mm inner diameter integrating sphere set in place of the gas cell prototype.

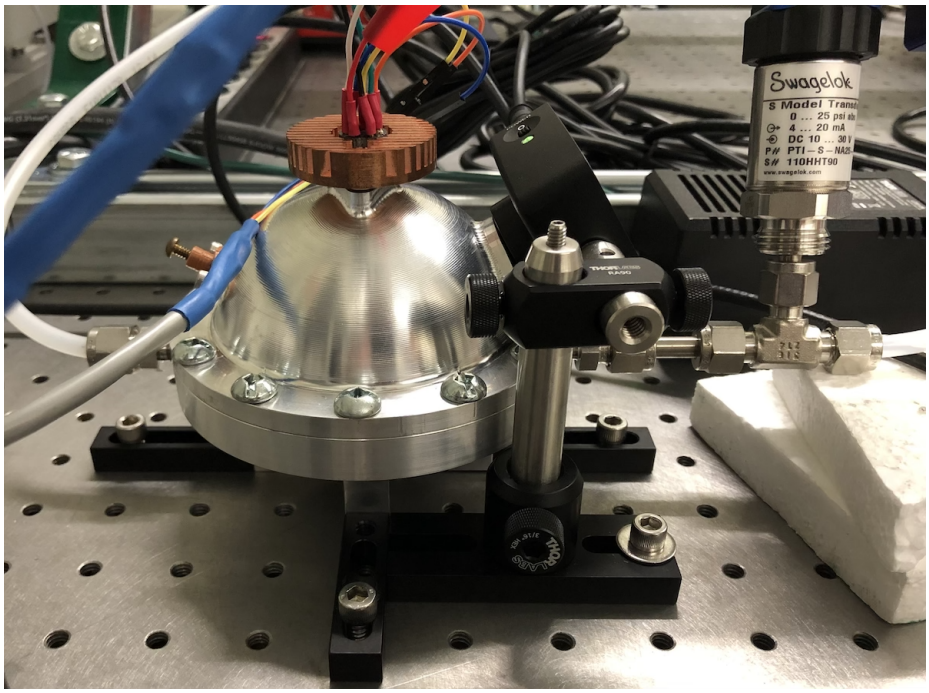

Figure 6.23: The aluminum 38.1 mm inner diameter gold-coated integrating sphere as set up in the Piro Lab mounted onto the imperial optics bench.

This integrating sphere is made from CNC-machined aluminum for an inner diameter of 38.1 mm. The inner surface was sandblasted followed by the deposition of

a ∼100 nm thick uniform layer of gold for maximizing reflectivity within the cavity. The device has two gas ports on the left and right side as oriented in the photograph, with the laser feed-through on-top alongside a custom copper heat sink and a sapphire window. Two other ports exist in the upper hemisphere: a small fibre port intended for spectrometer analyses and a larger PD window port.

One final difference with this apparatus when compared to the prototype gas cell is that this integrating sphere was designed to work with Norcada's TO-66 laser packaging (slightly larger in diameter at 11.55 mm and containing 9 pins). We were able to borrow one of these lasers from the Meldrum Lab, specifically one that was already in use with this integrating sphere model.

6.4.2 Data Acquisition and Analysis

Due to the difference in laser type, the LDC specifications were modified to observe a different absorption peak. The modulation ramp signal was kept the same as during tests with the prototype gas cell, but $I_{LD\,Set}$ was set to 56.00 ± 0.05 mA. This corresponds to a LDC current scan between 46.0 ± 0.5 mA and 66.0 ± 0.5 mA. According to the wavelength response of this laser model [111], the resulting wavelength scan is approximately between ∼1653.3 nm and ∼1653.8 nm, roughly a 5 nm scan. Looking at Figure 6.7, the matching absorption peak has a wavelength of ∼1653.73 nm. Sample waveforms recorded with the integrating sphere at lab pressure are provided in Figure 6.24 for pure Ar (left) and Ar + 3% CH_4 (±10%) (right). Of note, in comparison to the gas cell measurements under similar conditions, is that the ramp response of the PD is narrower in amplitude, worsening the signal-to-noise ratio of the PD response. However, the general shape of the background is evidently more linear in nature than with the gas cell's comparative PD response (see Figure 6.15).

Due to the poor leak tightness of this integrating sphere model, with a minimum vacuum of ∼1.9e-1 Torr and a clear leak check fail at primarily the laser port and

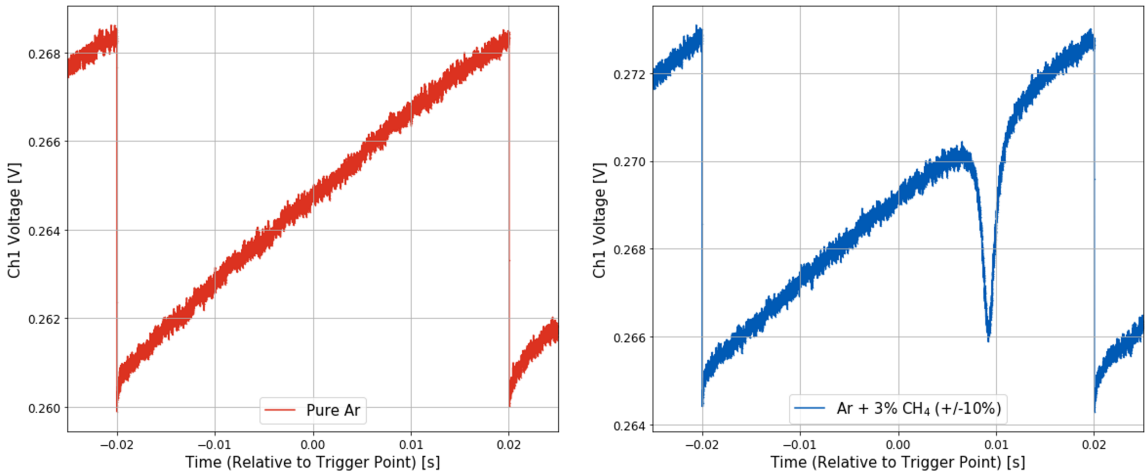

Figure 6.24: Sample waveforms as recorded with the test integrating sphere for $I_{LD\,Set} = 56.00 \pm 0.05$ mA. (Left) The background waveform recorded with pure Ar at lab pressure. (Right) The absorption waveform recorded with Ar + 3% CH_4 ($\pm$10%), highlighting the absorption peak associated with $\sim$1653.73 nm.

along the seal between both hemispheres of the sphere, a full test pressure calibration is not possible with the current apparatus. Neither would such an apparatus be safe for use with greater concentrations of CH_4 as planned for future characterization tests. Therefore, for further testing purposes and complete calibration with higher concentrations of CH_4, further leak sealing modifications will need to be made, if not the construction of an entirely new, more leak-tight integrating sphere.

As with the prototype gas cell, a more advanced apparatus, akin to what is shown in Figure 6.22, and or improved signal analysis methods would be required for proper live-monitoring of CH_4 measurements with this device. This would enable cleaner background subtraction cuts, allowing for a more reliable concentration calibration. As mentioned, further leak-tightening modifications of the device will allow for the measurement of pressure calibration data and safer measurement of greater CH_4 concentrations without needing to worry about leaks.

6.5 Future Development of LAS with SPCs

The LAS project for live CH_4 monitoring in S140 at SNOLAB is ongoing. As outlined in this chapter, we have performed test measurements with two different apparatuses - the prototype 42 cm gas cell and 244 cm effective path length integrating sphere. With the test apparatus set up in the Piro Lab at the University of Alberta, both apparatuses were capable of clear non-saturating absorption peak measurements with 3% ($\pm$10%) CH_4 level concentrations. The next step is to increase the concentration levels of CH_4 to the 6% to 10% range as will be used at SNOLAB.

Once a device is selected, the next phase of the apparatus design, including improved analysis and data collection techniques, along with apparatus advancements such as what was shown in Figure 6.22, will be explored. Either with simultaneous background and absorption waveform measurements or consistent background subtraction techniques, near-ideal background subtraction cuts should be achievable in the near future. This will remove the effects of interference from EMFs, time-dependent electronics performances, and short time-scaled modifications to the PD background response. Most importantly, it should enable the consistent measurement of absorption waveforms over longer data-taking periods where it's impractical, if not impossible to record background waveforms with just a single device. More precise test measurements will be performed alongside the Piro Lab radon trap, with current indications suggesting on the order of 10% of CH_4 being non-absorbed for an initial lab pressure of 3% ($\pm$10%) CH_4 concentration. This will validate the level of CH_4 absorption and its effect on the radon trap's radon absorption efficiency. These developments and measurement tests will be a part of an upcoming publication outlining the finalized design and test measurement results with the LAS setup. Plans are also in place to install and commission the completed apparatus underground at SNOLAB.

Chapter 7

Summary and Future Work

This thesis has presented two distinct avenues of study for the characterization and application of new instrumentation techniques for NEWS-G's latest and largest SPC detector: S140. In the NEWS-G collaboration's efforts to pursue evidence for some of the lightest of theorized WIMP masses, it is critically important to characterize and monitor the SPC's active volume and fill gas. Crucially, a careful understanding of these fundamental properties of detector behaviour serves as a significant piece to analyses in setting world-leading WIMP-nucleon cross section limits. While at first glance the studies presented in this thesis may be distinct, they are related in their goal of furthering our understanding of how the interactions between the gaseous volume and sensory equipment of an SPC impact NEWS-G's capacity to further push our WIMP sensitivity.

Through MC simulations of drifting electrons within S140's gas volume, the fiducialization of the entire detector can be studied to define the effective mass exposure of the sensory equipment to specific energy threshold-level events, as presented in Chapter 5. As seen here at LSM, the increasing reliance on methane as a means of lowering NEWS-G's WIMP-mass sensitivity, through an abundance of hydrogen target atoms, requires new methods for accurately measuring SPC gas contents. Laser absorption spectroscopy offers one possible solution, with Chapter 6 delving into possibilities for different apparatuses and a methodology for performing live measurements of this

ever-important gas. While these studies mostly have been looking in hindsight with the near-conclusion of the data analysis for the LSM campaign, there is a clear motivation for their use in the ongoing next phase of the S140 project at SNOLAB. It is additionally hoped that the groundwork laid out in this thesis results in further application beyond S140 and into the many planned future projects to be conducted by the NEWS-G experiment collaboration.

7.1 MC Electron Drift Simulations of S140

There have been many iterations of SPC simulation developed by the NEWS-G collaboration over the past decade. Alongside full detector simulations, like that used by the University of Birmingham's NEWS-G team, the University of Alberta team has been principally involved in advancing our first-principles detector simulation capabilities. This thesis outlined in Chapter 4 the current status of such simulation efforts, originally started upon by Y. Deng, and expanded upon to its current framework during this work.

Going forward, the study and iterative improvement of this simulation methodology will continue to be a subject of interest. Simulations prove a valuable tool as shown in Chapter 5. Of paramount interest is the study of space charge effects - the secondary Coulomb interactions between drifting electrons and other ions populating SPC detectors. These effects are hypothesized to account for discrepancies seen in other applications of this simulation work: drift and rise time studies of recorded LSM (and eventually SNOLAB) event data. Additionally, further, iterative optimization of detector electric field modelling and the electron drift methodology, including other, possibly unaddressed secondary effects is recommended to anyone continuing the pursuit of advancing our detector simulation efforts.

7.2 Fiducialization of S140 at LSM

In order to set constraints on the total mass exposure of the S140 detector during its CH_4 data collection run at LSM, a characterization of the detector's fiducial volume is paramount. Evermore so with the complex sensor geometry presented by the dually-channeled ACHINOS sensor in use during this measurement campaign. In Chapter 5, this thesis presented a direct application of using our MC electron drift simulation tool in studying the anode-wise distribution of different event species about an 11-anode ACHINOS sensor. This allowed for the characterization of S140's fiducial volume for respective events, specifically for the ACHINOS's south-channel in light of the LSM campaign's restriction to south-trigger data. With a successful calibration method, the result of this work was a set of volume efficiency cuts on near energy-threshold type events. These results will be used directly in the upcoming LSM data analysis paper in setting constraints on S140's effective mass exposure following final verification checks on potential systematic correlations in the simulation results.

This work lays the groundwork for more detailed studies of detector fiducialization with the SNOLAB campaign already underway. Of interest are improvements to the fiducialization calibration methodology. It is recommended that studies to fully characterize the effect of electron attachment within SPCs are undertaken to calibrate for contaminants such as O_2; necessary changes to the current simulation electron attachment method require such studies. Beyond this, it is also recommended that for more advanced calibration that improvements be made to the signal construction process, specifically in terms of defining anode gains. If this study is to be reproduced for S140 at SNOLAB, or any other future NEWS-G projects, that appropriate SPC and sensor geometry be implemented with the systematic study of the effect of uncertainties on HV conditions and dimensional variations taken into consideration beyond solely the detectors' gas conditions.

7.3 CH_4 Monitoring via LAS

With the continued reliance on CH_4 as a principle component to the fill gas of SPCs not only as a gas quencher but as a WIMP target, the precise measurement of said gas when used in a mixture is crucial for estimating a given detector's active mass. With advances in gas-related instrumentation being made at the University of Alberta in radon trapping, further reasons are presented for the need for such CH_4-monitoring capabilities with such instruments capable of removing CH_4 and lowering its concentration.

Chapter 6 of this thesis was dedicated to the testing of an early gas cell prototype and integrating sphere apparatus for performing a measurement technique new to the NEWS-G collaboration: laser absorption spectroscopy. This work presented early feasibility studies of implementing such a system for measuring the concentration of CH_4 within S140's fill gas, at SNOLAB, externally in circulation before filling the detector. Plans are currently set to advance characterization studies of both apparatuses to comparable CH_4 concentrations as to what will be used during the SNOLAB campaign ($\sim$6%-10%).

The principle challenges going forward for this project include exploring new analysis and data acquisition techniques for improved consistency in absorption peak measurements. Possible apparatus improvements such as the proper collimation of the 1654 nm IR laser diode and implementation of a dual-measurement apparatus for simultaneously recording background LAS waveforms were also presented in this work. Under these advances which will be explored in the near future, final characterization of both apparatus types may be made, leading to the finalization of the system to be implemented at SNOLAB. I will be continuing this project over the coming months, with a future publication in the works finalizing the details of the ultimate resolution to the outstanding challenges presented in this thesis.

Bibliography

[1] N. Aghanim *et al.*, "Planck 2018 results - vi. cosmological parameters," *A&A*, vol. 641, A6, 2020.

[2] M. W. Goodman and E. Witten, "Detectability of certain dark-matter candidates," *Phys. Rev. D*, vol. 31, pp. 3059–3063, 12 1985.

[3] M. Schumann, "Direct detection of wimp dark matter: Concepts and status," *J. Phys. G: Nucl. Part. Phys.*, vol. 46, p. 103 003, 2019.

[4] Q. Arnaud *et al.*, "First results from the news-g direct detection dark matter search experiment at the lsm," *Astroparticle Physics*, vol. 97, pp. 54–62, 2018, ISSN: 0927-6505.

[5] D. Durnford and M.-C. Piro, "The search for light dark matter with news-g," *Journal of Physics: Conference Series*, vol. 2156, p. 021 059, 2021, ISSN: 0927-6505.

[6] L. Balogh *et al.*, *The news-g detector at snolab*, 2022. [Online]. Available: https://arxiv.org/abs/2205.15433.

[7] V. Trimble, "Existence and nature of dark matter in the universe," *Annual Review of Astronomy and Astrophysics*, vol. 25, no. 1, pp. 425–472, 1987.

[8] W. Thomson, "Baltimore lectures on molecular dynamics and the wave theory of light," 2010.

[9] J. H. Oort, "The force exerted by the stellar system in the direction perpendicular to the galactic plane and some related problems," *Bull. Astron. Inst. Netherlands*, vol. 6, p. 249, 1932.

[10] H. Poincare, "The milky way and the theory of gases," *Popular Astronomy*, vol. 14, pp. 475–488, 1906.

[11] J. C. Kapteyn, "First attempt at a theory of the arrangement and motion of the sidereal system," *The Astrophysical Journal*, vol. 55, p. 302, 1922.

[12] F. Zwicky, "The redshift of extragalactic nebulae," *Helvetica Physica Acta*, vol. 6, pp. 110–127, 1933.

[13] F. Zwicky, "On the masses of nebulae and of clusters of nebulae," *The Astrophysical Journal*, vol. 86, p. 217, 1937.

[14] V. C. Rubin and W. K. Ford, "Rotation of the andromeda nebula from a spectroscopic survey of emission regions," *The Astrophysical Journal*, vol. 159, p. 379, 1970.

[15] K. C. Freeman, "On the disks of spiral and s0 galaxies," *The Astrophysical Journal*, vol. 160, p. 811, 1970.

[16] V. C. Rubin, W. K. Ford, and N. Thonnard, "Rotational properties of 21 sc galaxies with a large range of luminosities and radii, from ngc 4605 (r=4kpcs) to ugc 2885 (r=122kpc)," *The Astrophysical Journal*, vol. 238, pp. 471–487, 1980.

[17] K. G. Begeman, A. H. Broeils, and R. H. Sanders, "Extended rotation curves of spiral galaxies : Dark haloes and modified dynamics," *Monthly Notices of the Royal Astronomical Society*, vol. 249, p. 523, 1991.

[18] M. Milgrom, "A modification of the newtonian dynamics as a possible alternative to the hidden mass hypothesis," *The Astrophysical Journal*, vol. 270, pp. 365–370, 1983.

[19] D. I. Zabnina and A. V. Zasov, "Galaxies with declining rotation curves," *Astron. Rep.*, vol. 64, pp. 295–309, 2020.

[20] D. Clowe *et al.*, "A direct empirical proof of the existence of dark matter," *The Astrophysical Journal*, vol. 648, p. L109, 2006.

[21] X ray: NASA/CXC/Cfa/M.Markevitch et al, *1e 0657-57 with scale bar*, 2006. [Online]. Available: https://chandra.harvard.edu/photo/2006/1e0657/more.html#scale.

[22] Y. Akrami *et al.*, "Planck 2018 results - iv. diffuse component separation," *A&A*, vol. 641, A4, 2020.

[23] D. J. Fixsen, "The temperature of the cosmic microwave background," *The Astrophysical Journal*, vol. 707, no. 2, pp. 916–920, 2009.

[24] N. Aghanim *et al.*, "Planck 2018 results - v. cmb power spectra and likelihoods," *A&A*, vol. 641, A5, 2020.

[25] C. Alcock *et al.*, "The macho project: Microlensing results from 5.7 years of large magellanic cloud observations," *The Astrophysics Journal*, vol. 542, p. 281, 2000.

[26] M. Tanabashi *et al.*, *Phys. Rev. D*, vol. 98, p. 030 001, 2019, Particle Data Group.

[27] B. Audren *et al.*, "Strongest model-independent bound on the lifetime of dark matter," *Journal of Cosmology and Astroparticle Physics*, vol. 2014, p. 028, 2014.

[28] J. Billard *et al.*, "Direct detection of dark matter - appec committee report," *Report on Progress in Physics*, vol. 85, p. 056 201, 2021.

[29] G. Jungman, M. Kamionkowski, and K. Griest, "Supersymmetric dark matter," *Physics Reports*, vol. 267, no. 5, pp. 195–373, 1996, ISSN: 0370-1573.

[30] M. L. Graesser, I. M. Shoemaker, and L. Vecchi, "Asymmetric wimp dark matter," *Journal of High Energy Physics*, vol. 2011, no. 110, 2011.

[31] W. Hu, R. Barkana, and A. Gruzinov, "Fuzzy cold dark matter: The wave properties of ultralight particles," *Phys. Rev. Lett.*, vol. 85, pp. 1158–1161, 2000.

[32] A. Boyarsky *et al.*, "Sterile neutrino dark matter," *Progress in Particle and Nuclear Physics*, vol. 104, pp. 1–45, 2019.

[33] L. J. Hall *et al.*, "Freeze-in production of fimp dark matter," *Journal of High Energy Physics*, vol. 2010, no. 80, 2010.

[34] Y. Hochberg *et al.*, "Mechanism for thermal relic dark matter of strongly interacting massive particles," *Phys. Rev. Lett.*, vol. 113, p. 171 301, 2014.

[35] E. W. Kolb and A. J. Long, "Superheavy dark matter through higgs portal operators," *Phys. Rev. D*, vol. 96, p. 103 540, 2017.

[36] J. Ellis *et al.*, "Supersymmetric dark matter in light of wmap," *Physics Letters B*, vol. 565, pp. 176–182, 2003.

[37] R. W. Schnee, "Introduction to dark matter experiments," in *Physics of the Large and Small*. 2011, pp. 775–829.

[38] J. M. Gaskins, "A review of indirect searches for particle dark matter," *Contemporary Physics*, vol. 57, no. 4, pp. 496–525, 2016.

[39] A. Askew, S. Chauhan, B. Penning, W. Shepherd, and M. Tripathi, "Searching for dark matter at hadron colliders," *International Journal of Modern Physics A*, vol. 29, no. 23, p. 1 430 041, 2014.

[40] D. Baxter, I. M. Bloch, E. Bodnia, *et al.*, "Recommended conventions for reporting results from direct dark matter searches," *European Physical Journal C*, vol. 81, p. 907, 2021.

[41] A. M. Green, "Astrophysical uncertainties on the local dark matter distribution and direct detection experiments," *Journal of Physics G: Nuclear and Particle Physics*, vol. 44, p. 084 001, 2017.

[42] T. Piffl *et al.*, "The rave survey: The galactic escape speed and the mass of the milky way," *A&A*, vol. 562, A91, 2014.

[43] R. Bernabei, P. Belli, F. Cappella, *et al.*, "Final model independent results of dama/libra-phase 1," *The European Physical Journal C*, vol. 73, no. 2648, 2013.

[44] T. M. Undagoitia and L. Rauch, "Dark matter direct-detection experiments," *J. Phys. G: Nucl. Part. Phys.*, vol. 43, p. 013 001, 2016.

[45] Q. Arnaud *et al.*, "Precision laser-based measurements of the single electron response of spherical proportional counters for the news-g dark matter search experiment," *Phys. Rev. D*, vol. 99, p. 102 003, 2019.

[46] A. Aguilar-Arevalo *et al.*, "Results on low-mass weakly interacting massive particles from an 11 kg d target exposure of damic at snolab," *Phys. Rev. Lett.*, vol. 125, p. 241 803, 24 2020.

[47] O. Abramoff *et al.*, "Sensei: Direct-detection constraints on sub-gev dark matter from a shallow underground run using a prototype skipper ccd," *Phys. Rev. Lett.*, vol. 122, p. 161 801, 16 2019.

[48] P. Adhikari *et al.*, "First direct detection constraints on planck-scale mass dark matter with multiple-scatter signatures using the deap-3600 detector," *Phys. Rev. Lett.*, vol. 128, p. 011 801, 1 2022.

[49] P. Adhikari *et al.*, "Pulse-shape discrimination against low-energy ar-39 beta decays in liquid argon with 4.5 tonne-years of deap-3600 data," *The European Physical Journal C*, vol. 81, no. 823, 2021.

[50] R. Agnese *et al.*, "First dark matter constraints from a supercdms single-charge sensitive detector," *Phys. Rev. Lett.*, vol. 121, p. 051 301, 5 2018.

[51] E. Armengaud *et al.*, "Constraints on low-mass WIMPs from the EDELWEISS-III dark matter search," *Journal of Cosmology and Astroparticle Physics*, vol. 2016, no. 05, pp. 019–019, 2016.

[52] A. H. Abdelhameed *et al.*, "Probing spin-dependent dark matter interactions with ^{6}Li," *European Physical Journal C*, vol. 82, p. 207, 2022.

[53] C. Amole *et al.*, "Dark matter search results from the complete exposure of the PICO-60 C_3F_8 bubble chamber," *Phys. Rev. D*, vol. 100, p. 022 001, 2 2019.

[54] D. S. Akerib *et al.*, "Results of a search for sub-gev dark matter using 2013 LUX data," *Phys. Rev. Lett.*, vol. 122, p. 131 301, 13 2019.

[55] P. Agnes *et al.*, "Darkside-50 532-day dark matter search with low-radioactivity argon," *Phys. Rev. D*, vol. 98, p. 102 006, 10 2018.

[56] Y. Meng *et al.*, "Dark matter search results from the pandax-4t commissioning run," *Phys. Rev. Lett.*, vol. 127, p. 261 802, 26 2021.

[57] E. Aprile *et al.*, "Dark matter search results from a one ton-year exposure of XENON1T," *Phys. Rev. Lett.*, vol. 121, p. 111 302, 11 2018.

[58] E. Alfonso-Pita *et al.*, *Snowmass 2021 scintillating bubble chambers: Liquid-noble bubble chambers for dark matter and ceνns detection*, 2022. [Online]. Available: https://arxiv.org/abs/2207.12400.

[59] P. Grothaus, M. Fairbairn, and J. Monroe, "Directional dark matter detection beyond the neutrino bound," *Phys. Rev. D*, vol. 90, p. 055 018, 5 2014.

[60] F. Mayet *et al.*, "A review of the discovery reach of directional dark matter detection," *Physics Reports*, vol. 627, pp. 1–49, 2016, A review of the discovery reach of directional Dark Matter detection, ISSN: 0370-1573.

[61] F. Sauli, *Gaseous Radiation Detectors: Fundamentals and Applications*, ser. Cambridge Monographs on Particle Physics, Nuclear Physics and Cosmology. Cambridge University Press, 2014. DOI: 10.1017/CBO9781107337701.

[62] I. Giomataris *et al.*, "A novel large-volume spherical detector with proportional amplification read-out," *Journal of Instrumentation*, vol. 3, no. 09, P09007–P09007, 2008.

[63] J. Derre, *Pulse shape in the spc prototype*, Technical Report, 2007. [Online]. Available: https://newsgorg.files.wordpress.com/2018/07/pulse-shape-in-the-spc-prototype.pdf.

[64] COMSOL Multiphysics® v. 6.0. www.comsol.com COMSOL AB, Stockholm, Sweden.

[65] G. Giroux, P. Gros, and I. Katsioulas, "The search for light dark matter with the NEWS-g spherical proportional counter," *Journal of Physics: Conference Series*, vol. 1312, p. 012 008, 2019.

[66] P. B. O'Brien, "Optimization of processing parameters and development of a radon trapping system for the news-g dark matter detector," M.S. thesis, Edmonton, Alberta, Canada, 2021.

[67] L. Balogh *et al.*, "Copper electroplating for background suppression in the news-g experiment," *Nuclear Instruments and Methods in Physics Research Section A: Accelerators, Spectrometers, Detectors and Associated Equipment*, vol. 988, p. 164 844, 2021, ISSN: 0168-9002.

[68] L. Balogh *et al.*, "Quenching factor measurements of neon nuclei in neon gas," *Phys. Rev. D*, vol. 105, p. 052 004, 5 2022.

[69] M. Inokuti, "Ionization yields in gases under electron irradiation," *Radiation Research*, vol. 64, no. 1, pp. 6–22, 1975.

[70] U. Fano, "Ionization yield of radiations. ii. the fluctuations of the number of ions," *Phys. Rev.*, vol. 72, pp. 26–29, 1 1947.

[71] D. Durnford, Q. Arnaud, and G. Gerbier, "Novel approach to assess the impact of the fano factor on the sensitivity of low-mass dark matter experiments," *Phys. Rev. D*, vol. 98, p. 103 013, 10 2018.

[72] D. Durnford, "Phenomenological studies and analysis techniques to search for light dark matter with news-g," M.S. thesis, Kingston, Ontario, Canada, 2018.

[73] R. W. Conway and W. L. Maxwell, "A queuing model with state dependent service rates," *Journal of Industrial Engineering*, vol. 12, no. 2, pp. 132–136, 1962.

[74] *Tunable IR DFB lasers - 1654 nm specifications*, NL1654-T, SN20251, TO 39 Package Type, Norcada, 2021.

[75] R. W. Stoenner, O. A. Schaeffer, and S. Katcoff, "Half-lives of argon-37, argon-39, and argon-42," *Science*, vol. 148, no. 3675, pp. 1325–1328, 1965.

[76] F. V. de Sola Fernandez, "Solar kk axion search with news-g," Ph.D. dissertation, Kingston, Ontario, Canada, 2020.

[77] A. Giganon *et al.*, "A multiball read-out for the spherical proportional counter," *Journal of Instrumentation*, vol. 12, no. 12, P12031–P12031, 2017.

[78] I. Giomataris *et al.*, "A resistive ACHINOS multi-anode structure with DLC coating for spherical proportional counters," *Journal of Instrumentation*, vol. 15, no. 11, P11023–P11023, 2020.

[79] T. Neep, "Searching for light dark matter with NEWS-G," IoP - Joint APP/HEPP/NP Conference, 2021. [Online]. Available: https://indico.cern.ch/event/1013634/contributions/4313199/contribution.pdf.

[80] S. Agostinelli *et al.*, "Geant4—a simulation toolkit," *Nuclear Instruments and Methods in Physics Research Section A: Accelerators, Spectrometers, Detectors and Associated Equipment*, vol. 506, no. 3, pp. 250–303, 2003, ISSN: 0168-9002.

[81] J. Allison *et al.*, "Recent developments in geant4," *Nuclear Instruments and Methods in Physics Research Section A: Accelerators, Spectrometers, Detectors and Associated Equipment*, vol. 835, pp. 186–225, 2016, ISSN: 0168-9002.

[82] H. Shindler, Garfield ++. [Online]. Available: https://garfieldpp.web.cern.ch/garfieldpp/.

[83] Rene Brun and Fons Rademakers, *ROOT - An Object Oriented Data Analysis Framework*, Proceedings AIHENP'96 Workshop, Lausanne, Sep. 1996, Nucl. Inst. & Meth. in Phys. Res. A 389 (1997) 81-86. See also https://root.cern/.

[84] T. Neep, I. Katsioulas, P. Knights, J. Matthews, K. Nikolopoulos, and R. Ward, "A simulation framework for spherical proportional counters," 2021, p. 917. DOI: 10.22323/1.390.0917.

[85] S. Biagi, Magboltz. [Online]. Available: https://magboltz.web.cern.ch/magboltz/.

[86] S. Biagi, "Monte carlo simulation of electron drift and diffusion in counting gases under the influence of electric and magnetic fields," *Nuclear Instruments and Methods in Physics Research Section A: Accelerators, Spectrometers, Detectors and Associated Equipment*, vol. 421, no. 1, pp. 234–240, 1999, ISSN: 0168-9002.

[87] Y. Deng, "Detector response simulation for NEWS-G experiment," CAP Congress, 2022. [Online]. Available: https://indico.cern.ch/event/1072579/contributions/4788587/contribution.pdf.

[88] H. C. Berg, "Diffusion: Microscopic theory," in *Random Walks in Biology*. 1993, pp. 5–16.

[89] G. Savvidis, *LSM Data Analysis Update: North/South/Shared ratio of offtrigger events*, NEWS-G Collaboration internal report, October 2020.

[90] G. Savvidis, *Un-biased results for North/South/Shared events*, NEWS-G Collaboration internal report, June 2021.

[91] D. Durnford, *W-Value Measurements in Methane*, NEWS-G Collaboration internal report, December 2021.

[92] R. Barlow, *Asymmetric statistical errors*, 2004. [Online]. Available: https://arxiv.org/abs/physics/0406120.

[93] D. Durnford, "The NEWS-G light dark matter search experiment: Current status and preparation for experiment at SNOLAB," CAP Congress, 2022. [Online]. Available: https://indico.cern.ch/event/1072579/contributions/4788511/contribution.pdf.

[94] G. Savvidis, *XTalk study*, NEWS-G Collaboration internal report, November 2021.

[95] Brookhaven National Laboratory National Nuclear Data Center, *NuDat (Nuclear Structure and Decay Data)*. Mar. 2008.

[96] A. Brossard, "Optimization of spherical proportional counter backgrounds and response for low mass dark matter search," Ph.D. dissertation, Kingston, Ontario, Canada, 2020.

[97] S. M. Kuznicki *et al.*, "Xenon adsorption on modified ets-10," *The Journal of Physical Chemistry C*, vol. 111, no. 4, pp. 1560–1562, 2007.

[98] W. R. Morrish, "Sensing with optical microresonators and integrating cavities," Ph.D. dissertation, Edmonton, Alberta, Canada, 2021.

[99] C. N. Banwell and E. M. McCash, *Fundamentals of Molecular Spectroscopy*. McGraw-Hill, 1994.

[100] A. Fried and D. Richter, "Infrared absorption spectroscopy," in *Analytical Techniques for Atmospheric Measurement*. John Wiley & Sons, Ltd, 2006, ch. 2, pp. 72–146, ISBN: 9780470988510.

[101] I. Gordon *et al.*, "The hitran2020 molecular spectroscopic database," *Journal of Quantitative Spectroscopy and Radiative Transfer*, vol. 277, p. 107 949, 2022, ISSN: 0022-4073.

[102] P. Werle *et al.*, "Near- and mid-infrared laser-optical sensors for gas analysis," *Optics and Lasers in Engineering*, vol. 37, no. 2, pp. 101–114, 2002.

[103] H. He *et al.*, "In-situ testing of methane emissions from landfills using laser absorption spectroscopy," *Applied Sciences*, vol. 11, no. 5, 2021.

[104] T. A. Hu, E. L. Chappell, J. T. Munley, and S. W. Sharpe, "Improved multipass optics for diode laser spectroscopy," *Review of Scientific Instruments*, vol. 64, no. 12, pp. 3380–3383, 1993.

[105] *CR-110-R2.1 charge sensitive preamplifier: Application guide*, CR-110-R2.1, Cremat Inc, 2020.

[106] *Moku:lab's oscilloscope user manual*, 2011. [Online]. Available: https://www.liquidinstruments.com/resources/supporting-material/product-documentation/.

[107] Liquid Instruments Pty. Ltd.. Moku:Lab Python Interface. [Online]. Available: https://pymoku.readthedocs.io/en/2.8.3/.

[108] D. Rehle, D. Leleux, M. Erdelyi, *et al.*, "Ambient formaldehyde detection with a laser spectrometer based on difference-frequency generation in ppln," *Appl Phys B*, vol. 72, pp. 947–952, 2001.

[109] J. Peng *et al.*, "Asymmetric least squares for multiple spectra baseline correction," *Analytica Chimica Acta*, vol. 683, no. 1, pp. 63–68, 2010.

[110] E. Hawe *et al.*, "Hazardous gas detection using an integrating sphere as a multipass gas absorption cell," *Sensors and Actuators A: Physical*, vol. 141, no. 2, pp. 414–421, 2008.

[111] *Tunable IR DFB lasers - 1654 nm specifications*, NL1654-T, SN19013, TO 66 Package Type, Norcada, 2021.

Appendix A: COMSOL Model Dimensions

As a part of the development of a COMSOL Multiphysics® finite element method software modelling of S140's electric field, a fully dimensioned 3-D CAD model was required (see Figure 4.1 (a)). This CAD model was developed in COMSOL directly using physical measurements of S140's sensory equipment, including ACHINOS and rod structures. For the dimensioning purpose, Figure A.1 provides a labelling diagram for different measurables used in defining the CAD model geometry.

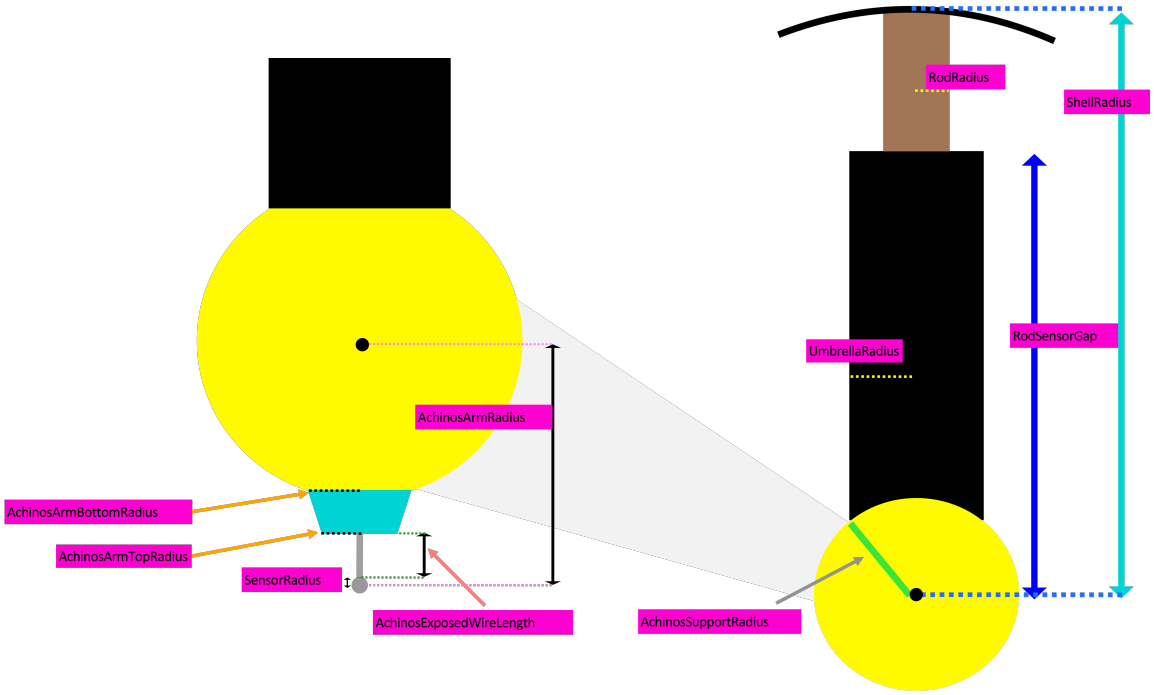

Figure A.1: Labelling diagram of sensory components in S140 used for COMSOL model dimensions as laid out in Table A.1. (Left) Close-up view of the central ACHINOS structure and dimensions. (Right) Large-scale view of the labelling of the sensory equipment in S140. Credit: F. Vazquez de Sola.

Table A.1: COMSOL dimensions for the 3-D CAD model presented in Figure 4.1 (a). The COMSOL model values were recorded by physical measurements of the sensory equipment used with S140 by G. Savvidis. For reference, Figure A.1 serves as a labelling diagram for the majority of dimensions listed.

Dimension Label	**COMSOL Value [mm]**	**Description**
ShellRadius	675	S140 inner shell radius
SensorRadius	0.85	Individual sensor anode radius
UmbrellaRadius	3.75	Radius of "umbrella" part of the rod/sensor
RodRadius	3	Radius of the rod
RodSensorGap	∼28.495	Distance between the centre of the sensor (model origin) & opposite end of the umbrella
AchinosSupportRadius	7.5	Radius of the inner ball support of the ACHINOS
AchinosArmRadius	∼14.85	Distance between centre of ACHINOS (origin) and centre of the anodes
AchinosArmBottomRadius	2.1	Radius of the innermost portion of the "arms" supporting each anode wire
AchinosArmTopRadius	∼1.6	Radius of the outermost portion of the "arms" supporting each anode wire
AchinosExposedWireRadius	0.25	Anode wire radius
AchinosExposedWireLength	3.8	Length of the exposed anode wire segment

For each of these dimensions, amongst others, Table A.1 provides the respective values used in defining the COMSOL CAD model used for this thesis as recorded by G. Savvidis. Some other geometrical notes of importance include that the centre of the ACHINOS - in the middle of the central support structure for the anodes - is defined as the origin of the overall CAD model (normally defined in spherical polar

coordinates). Each of the eleven anodes displays approximately icosahedral symmetry about the central support structure. The angle between the bottom ("southernmost") anode and the nearest anode latitude is denoted exactly as $\pi/2 - \tan^{-1}(1/2)$ radians and to the further anode latitude is $\pi/2 + \tan^{-1}(1/2)$ radians. For each latitude with five anodes present, there is $2\pi/5$ radians spacing between each adjacent anode.

Appendix B: Rise Time Simulation Methodology

The rise time of a signal pulse is defined for treated (integrated doubly-deconvolved) pulses as the time interval between the points where the pulse reaches 10% and either 75% ($t_{(10\%-75\%)\,rise\,time}$) or 90% ($t_{(10\%-90\%)\,rise\,time}$) of its maximum amplitude. The rise time of a signal pulse is correlated to the radial origin of the corresponding event as rise times correspond to longer drift times and consequently greater levels of diffusion. The specific choice of using either 75% or 90% to define rise time depends upon the application. In general, when the level of diffusion in the given SPC measurement is high, a 10%-90% rise time calculation has a less likely chance of missing any rises in amplitude due to straggling, late arrival time electrons. A 10%-75% rise time definition works better for low diffusion times, incorporating less noise into its computation.

To simulate signal rise times, as performed in Chapter 5 with the electron attachment calibration of MAGBOLTZ O_2 concentrations, we make use of code originally written by Q. Arnaud in ROOT and later adapted for 3-D simulations by Y. Deng. The working principle of the method is that we want to avoid a complete signal simulation, but solely focus on extracting the specific rise time of interest using structural inferences about the shape of the treated pulse. To start, for each simulated event with $N > 0$ primary electrons reaching the sensor (in this case we will assume an ACHINOS anode) we will have a set of individual drift times that are simply the sum

of each primary electrons time steps:

$$t_d = \sum_{k=1}^{N_{steps}} \Delta t_k = \sum_{k=1}^{N_{steps}} \left(\frac{\Delta s_0}{v_d} \right)_k , \tag{B.1}$$

where t_d is an individual primary electron's drift time and the remaining variables correspond to Equation 4.3. This set of drift times is sorted in ascending order and represents the relative arrival times for each primary electron.

To define treated pulses, we assume that they are ideal and follow a Gaussian cumulative density function where each pre-integrated pulse has a defined Gaussian resolution (σ_{PE}) and amplitude (A_{PE}). The pulse widths can be arbitrary so long as they are small relative to the window of arrival times of the primary electrons: $\sigma_{PE} << (t_{d_{max}} - t_{d_{min}})$. For the purposes of this thesis we set $\sigma_{PE} = 0.001$ μs. The signal amplitudes are drawn from Polya distributions (Equation 3.5) where their gain ($\langle G \rangle = n/\langle n \rangle$) corresponds to the gain of the detector. For the ACHINOS, we use the same gain definitions as in Section 5.1.2. With these two parameters, the total signal amplitude of the treated pulse is the following sum:

$$A_{max} = \sum_{k=1}^{N_{PE}} \frac{A_{PE_k}}{2} \left(1 + \text{erf} \left(\frac{(L - t_{d_k})}{\sqrt{2}\sigma_{PE_k}} \right) \right) . \tag{B.2}$$

where L is sufficiently larger than the mean of the pulse (i.e. the drift time) such that the pulse "tail" is within the error function's argument domain. For this thesis, we set $L = t_{d_{max}} + 8\sigma_{PE_k}$.The corresponding rise time for this signal then occurs within the time interval where the pulse reaches between $0.10A_{max}$ and $0.75A_{max}$ or $0.90A_{max}$.

To estimate the times corresponding to each amplitude value, we perform a search algorithm for $t_{10\%-rise}$ and $t_{75\%-rise}$ (or $t_{90\%-rise}$). For this search we first pre-define a large array of time steps where each step is defined as:

$$t_{step} = \frac{1}{20}(t_{d_{max}} - t_{d_{min}} + 0.1) \left(\frac{1}{2} \right)^j , \tag{B.3}$$

where j ranges from 0 to 99,999, yielding 100,000 unique step values. For each rise time value we set an initial guess as the drift time value corresponding to the 10^{th},

75^{th}, or 90^{th} percentile electron in terms of arrival times (drift times). With this initial guess, we perform a calculation akin to the sum in Equation B.2, but we replace $(L - t_{d_k})$ with the corresponding percentile arrival time to truncate the CDM calculation up to the guessed 10% rise location:

$$A_{10\%-guess} = \sum_{k=1}^{N_{PE}} \frac{A_{PE_k}}{2} \left(1 + \text{erf}\left(\frac{(t_{10\%-guess} - t_{d_k})}{\sqrt{2}\sigma_{PE_k}}\right)\right). \tag{B.4}$$

Depending upon whether the resulting amplitude is greater than or less than the expected percent amplitude, we either increase or decrease the initial guess time by the next available time step. This process is repeated until the guessed pulse amplitude is equal to, within a selected relative error of 0.0001%, the true pulse amplitude corresponding to the 10%, 75%, or 90% rise time location. Once this search algorithm is performed for $t_{10\%-rise}$ and the preferred upper rise time value, the final rise time is recorded as either $t_{(10\%-75\%)\,rise\,time} = t_{75\%-rise} - t_{10\%-rise}$ or $t_{(10\%-90\%)\,rise\,time} = t_{90\%-rise} - t_{10\%-rise}$.

Appendix C: LAS Gas Cell Custom Component Dimensions

The following CAD drawings illustrate the dimensions for the custom 3-D printed parts (using PLA plastic) used in the vacuum sealing and optical alignment of the 1/2" diameter sapphire window and lens inside their respective end cap of the prototype LAS gas cell. Each custom part, optical component, and silicon o-ring are placed inside the ∼0.504" diameter (hole only needs a 0.5" allowance, can be tighter than 0.504"), ∼0.403" deep counterbored hole cut-out on the VCR end of each of the 1/2"-Swagelok to 1/2"-VCR connectors. Figure 6.10 will be used for reference to illustrate where inside the gas cell end caps that each component exists.

The first two components are the first to be placed inside their respective end cap (inside the ∼0.403" deep counterbored holes) as spacers such that the face of each optical component isn't directly in contact with stainless steel. For the lens end cap (labelled (A) in Figure 6.10), we use the spacer design in Figure C.1 which features a sloped inner lip on one side to accommodate the curvature of the convex lens.

The other spacer, meant for the sapphire window end cap (labelled (B) in Figure 6.10), features a flat face on either side as depicted in Figure C.2. Since the sapphire window is shaped like a flat disk, the curvature of the lens spacer is unnecessary.

With each spacer placed inside their respective end cap, the corresponding optical component, followed by a silicon o-ring is placed inside over top.

The final custom 3-D printed part is identical for each end cap. As depicted in Figure C.3, this custom part acts a "plug" that compresses the three aforementioned

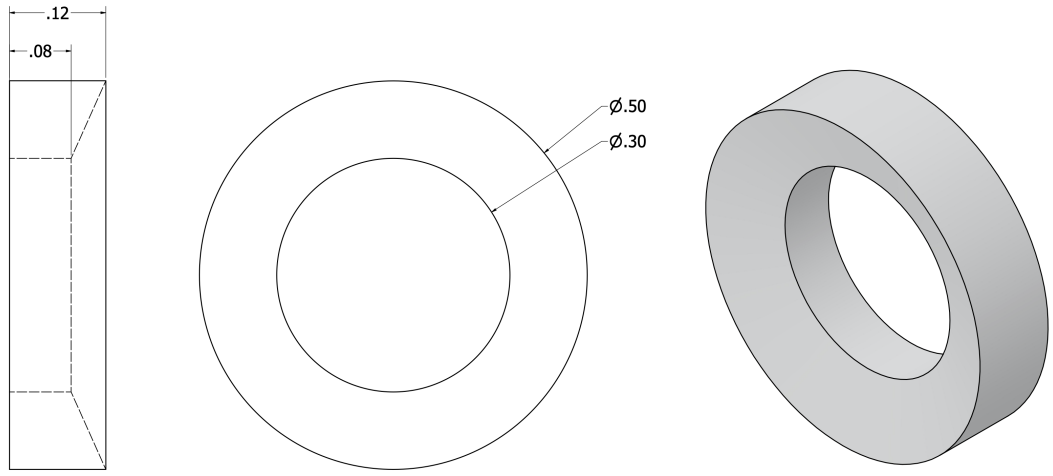

Figure C.1: Imperial dimensions (in inches) for the custom 3-D printed spacer component used in the lens end cap ((A) in Figure 6.10). One side features a sloped inner lip to accommodate the shape of the 1/2" lens. CAD model credit: Y. Ko.

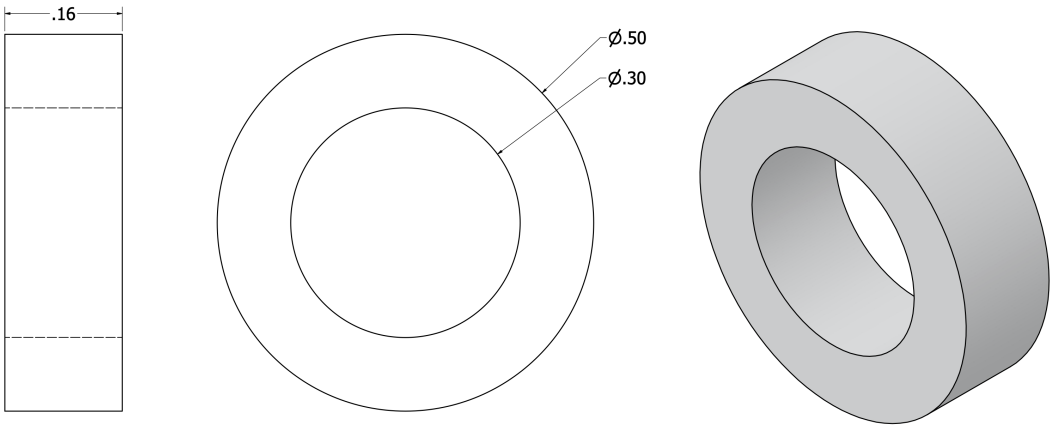

Figure C.2: Imperial dimensions (in inches) for the custom 3-D printed spacer component used in the sapphire window end cap ((B) in Figure 6.10). CAD model credit: Y. Ko.

parts already inside of each end cap. This forms the vacuum seal by squeezing silicon o-rings. The smaller diameter end of each of these components is chamfered such that the respective o-ring will be compressed against the inner stainless steel surface of the end cap. The female 1/2" VCR nuts are tightened as much as possible onto

the VCR threads over the top of these plugs to form the compressing seal.

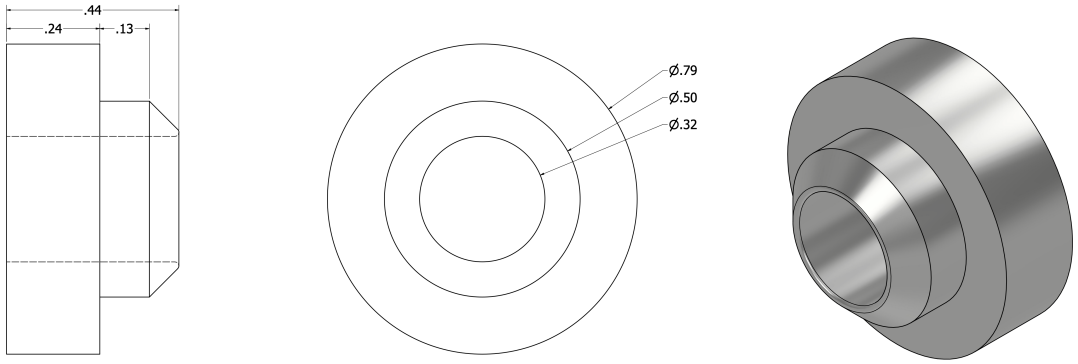

Figure C.3: Imperial dimensions (in inches) for the custom 3-D printed "plug" component used in both end caps to compress the spacers, optical components, and most importantly, the silicon o-rings to form a vacuum seal. CAD model credit: Y. Ko.